Effets des inhomogénéités nanométriques sur les propriétés magnétiques de systèmes magnétiques dilués

Akash Chakraborty

HAL Id: tel-00947328

https://theses.hal.science/tel-00947328

Submitted on 15 Feb 2014

UNIVERSITÉ DE GRENOBLE

THÈSE

Pour obtenir le grade de

DOCTEUR DE L'UNIVERSITÉ DE GRENOBLE

Spécialité : **PHYSIQUE/PHYSIQUE DE MATIERE CONDENSEE & RAYONNEMENT**

Arrêté ministériel : 7 août 2006

Présentée par

Akash Chakraborty

Thèse dirigée par **Georges BOUZERAR**

préparée au sein de l'**Institut Neel, CNRS-UJF**
dans **l'École Doctorale de Physique de Grenoble**

Effets des inhomogénéités nanométriques sur les propriétés magnétiques de systèmes magnétiques dilués

Thèse soutenue publiquement le **26 Juin 2012** ,
devant le jury composé de :

M. Roland HAYN
Professeur, Aix-Marseille University, Marseille   (Rapporteur)
M. Stefan KETTEMANN
Professeur, Jacobs University Bremen, Bremen   (Rapporteur)
Mme. Lucia REINING
Directeur de Recherche, Ecole Polytechnique Palaiseau   (Membre)
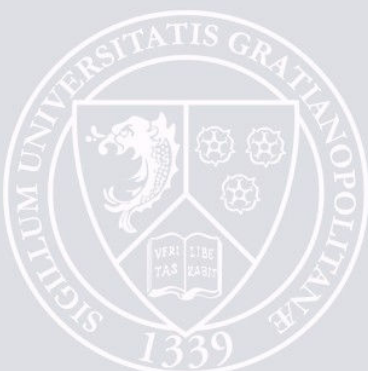**M. Georges BOUZERAR**
Directeur de Recherche, Institut Néel, Grenoble   (Directeur de thèse)
M. Denis FEINBERG
Directeur de Recherche, Institut Néel, Grenoble   (Membre)
M. Didier MAYOU
Directeur de Recherche, Institut Néel, Grenoble   (Membre)

To the people of my motherland ...

Acknowledgments

This thesis is perhaps the most important as well as significant achievement of my life till now, and the person without whom it would not have been possible is my supervisor Prof. Georges Bouzerar. I do not have enough words to thank him for the constant help and support he has provided throughout all these years of my PhD. Despite innumerable problems and hardships in his personal life he was always there for me. I have learned so many important things from him that it is difficult to recount everything here. Apart from the various concepts of physics and the necessary computational skills, the other important thing he has taught me is to maintain one's honesty and integrity, which is sometimes unfortunately lacking in this profession. His immense patience even when I committed serious blunders was a constant source of motivation for me. He was more than a supervisor to me as he not only helped me with science, but he was also there for all kinds of daily life hassles like finding an apartment, opening a bank account, and so many other things. It was also because of him that I got a post-doc position even before finishing my PhD thesis. Thank you so much for introducing me to this rich and interesting field of research. It was a real pleasure knowing and working with you. I would remain ever so grateful to you for all you have done for me.

Another person who was of immense help during these last years is Dr. Richard Bouzerar. I would like to sincerely thank him from the deepest core of my heart for all the time he has spent with me, collaborating on several projects. The numerous discussions with him was of great help in my work and I have learned so much, particularly about computational techniques, from him. His insightful comments and timely suggestions helped make this work relatively easy. Thanks a lot for everything.

I would take this opportunity to express my deep gratitude to all members of my PhD jury: Prof. Denis Feinberg, Prof. Didier Mayou, and Prof. Lucia Reining for agreeing to be the examiners of my PhD defense, and especially Prof. Stefan Kettemann and Prof. Roland Hayn for kindly accepting to be the referees of this manuscript.

In all these years that I have spent at the Institut Néel, I met so many people with whom I had valuable discussions on science or anything else. Among them one person I would like to sincerely thank is Dr. Arnaud Ralko. He has helped me a lot, especially during the initial stages of my PhD. He had always been patient and understanding irrespective of how trivial my questions or queries were.

I would also like to thank all the administrative staff of the MCBT Department of Institut Néel for being so helpful and cooperating. Not to forget, at the same time, all the people from the computer center who were equally helpful and were always there in times of need. It was nice knowing you all and many thanks for your cooperation.

The last few months of my PhD I spent at the Jacobs University in Bremen, and I must say that I am very lucky to have a bunch of wonderful friends there. I would particularly like to thank Dr. Paul Wenk for the numerous useful scientific discussions as well as helping me with other things when I first moved to Bremen. I would also like to thank Daniel Jung, Aleksander Hinz, and Llea Samuel for creating an amicable atmosphere in our group there.

In the three years that I have spent in Grenoble, the best thing that has happened to me and which will remain with me forever is the delightful and great group of friends that I have made here. I really do not know what I would have done without them. Their presence has always made my stay here enjoyable and I never really felt that I was so far away from my home. Among them one whom I can never thank enough is Arpan Krishna Deb. He has always been with me through thick and thin, and was a constant source of motivation and inspiration. We had innumerable discussions on various things from science to movies, sports to food, and anything and everything that came to our mind. I have spent some of the best time of my life with him, and among them the most cherished ones are the long walks we took along the river in the late evenings. He has been more than a brother to me and I am really fortunate to have met a wonderful and humble person like him. Another person very close to me is Maitreyee Mookherjee, whose constant love and affection gave me the warm feeling of my family. I have learned from her the true meaning of sacrifice that one can make for the person one loves. I will never forget the sumptuous dinners, and especially the delicious Indian desserts that she used to make for us. I am equally thankful to Anita Sarkar,

who has been a wonderful friend and is one of the nicest persons I have ever met. Her jovial nature and utmost caring attitude was a source of relief in times of distress and anxiety. Also her kindness and hospitality is something exemplary. The person who deserves special mention here is Soumen Mandal, who has helped me in more ways than I can remember. His ideas and opinions about research as well as his views on the scientific community in general served as a guideline in the early days of my work. I also express my deepest gratitude to friends like Ananda Shankar Basu, Priyadarshini Chatterjee, Ayan Kumar Bandyopadhyay and Kuheli Bandyopadhyay, Subhadeep Datta, Dibyendu Hazra, Chandan Bera, Kalpana Mandal, Anupam Kundu, Biplab Biswas, Sutirtha and Dipanwita Mukhopadhyay, Arijit and Satarupa Roy, Abhijit Ghosh, Roopak Sinha, Arpita Chanda, and Sandeep Kumar Srivastava, for making my sojourn in Grenoble memorable. I would particularly like to thank Priyadarshini Chatterjee for helping me out with several things when I first came to Grenoble, and it was through her that I was introduced to this big and extended family of ours. It has been a great pleasure to know you all and I wish you the very best for all your future endeavors.

Talking about friends, I am sincerely grateful to my childhood friends from school Ranadip Banerjee, Anirban Pal, Subhabrata Banerjee, and Awadul Haque. Their love and friendship is something that I will always treasure. Among the friends that I had made during my years at the university, the one who will always remain very special to me is Sourav Mitra. He has taught me the real value of friendship and camaraderie. His relentless support and encouragement, during all these years, is one of the reasons that I have come this far. His modesty and humbleness is something worth emulating. I would also like to thank Sanjukta Chatterjee, Arindam Datta, Arghya Choudhury, Pratyay Banerjee, Arindam Chakraborty, Jyoti Prasad Saha, Sourish Mitra, and Sourav Guha for their affection and adulation.

The stepping stone in this long journey thus far was my school, St. Patrick's H.S. School Asansol. I will always remain indebted to this lovely institution and the great teachers that I have had the opportunity to learn from. I express my sincerest gratitude to Late Mrs. B. Berger whose uncompromising dedication to teaching has always been a source of inspiration for me. It is most unfortunate that she is no more with us today. I am also very thankful to Mr. Ravi Victor from whom I actually started learning the basics of physics. His lucid teaching and constant encouragement strongly influenced me to take up this subject. I am equally grateful to my teachers at the Physics Department of Jadavpur University, Prof. Ranjan Bhattacharya, Prof. Dhiranjan Roy, Prof. Kushal Goswami, and Prof. Amitava Datta. I would especially like to thank Prof. Narayan Banerjee and Prof. Soumen

Kumar Roy, without whose help and support I would not have been able to come to France. I would also like to take this opportunity to thank my painting teacher, Mr. Madhu Biswas, who taught me the value of devotion towards one's work, ever since my childhood days.

Now the people who matter the most to me and without whom I would not have been here, are my parents Mrs. Jharna Chakraborty and Mr. Tapas Chakraborty. I do not want to thank them because I know that I can never thank them enough for what they have done for me. Despite the severe adversities they had to face all along, I never had to feel the brunt of anything. They have provided me with the best possible education and it is due to their unconditional love and immense moral support that I have made it this far today. They have been my biggest source of inspiration and motivation. I have always considered myself fortunate to have been blessed with such wonderful parents and I just hope that I have been able to fulfill their dreams, at least to a certain extent.

Finally, the person who has had the single biggest influence on my life is my uncle, Mr. Abhijit Sengupta, whom I fondly call *Kaku*. Many people, including my friends and family, have always loved me but he is the only person who has taught me to love others. Ever since I can remember I have learned so much from him about different aspects of life, that it helped change my entire conception of the world we live in. His utmost honesty and integrity is something which I have always aspired to achieve. Despite the geographical distance between us, I have always felt that he is here with me acting as my conscience. I have never seen God but if I've ever seen someone close to Him, he is my *Kaku*.

Contents

Chapter 1

Introduction

1.1 Nanostructured Materials for Spintronics

Spintronics, a neologism for *spin electronics*, is a relatively new and rapidly growing branch of study in condensed matter physics. Until now, conventional solid-state devices, based on Si and GaAs, made use of only the fundamental charge of the electron. The whole idea behind spintronics is to incorporate the spin degree of freedom and its associated magnetic moment, and this is believed to lead to a significant advancement over existing semiconductor technology. This may offer several benefits such as nonvolatile memories, increased data processing speed and decreased power consumption, among others. The spin field-effect-transistor (SPINFET), proposed by Datta and Das in 1990 [1], can be considered as one of the earliest suggestions for the use of semiconductors for spintronics. A sketch of the device is shown in Figure 1.1. The most important advantage of the SPINFET is the efficient spin injection from the ferromagnetic source into the channel (a 2 dimensional electron gas). One of the major breakthroughs in the field of spintronics came with the discovery of the Giant Magneto Resistance (GMR) effect in 1988 by A. Fert and P. Grünberg, which earned them the 2007 Nobel Prize in Physics. The GMR effect is observed in alternating stacks of magnetic and non-magnetic metallic multilayers. The conductance of a GMR device depends strongly on an applied magnetic field, which can
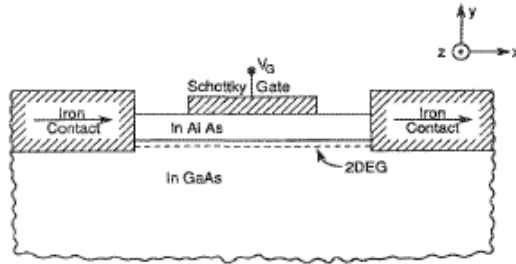
Figure 1.1: Original design of the SPINFET, as proposed by Datta and Das, from Ref. [1].

switch the interlayer exchange coupling. This phenomenon is applied in the spin-valve device used in the red heads of a hard disk drive. This has led to a considerable increase in the memory density of hard disk drives. Figure 1.2 shows an illustration of this new memory technology known as magnetoresistive random-access memory (MRAM). Now when the non-magnetic layer is insulating instead of metallic, it leads to another effect known as the Tunnel Magneto Resistance (TMR), which can result in a more enhanced magnetoresistance. More detailed reviews on spintronics and its applications can be found in Ref. [2, 3, 4].
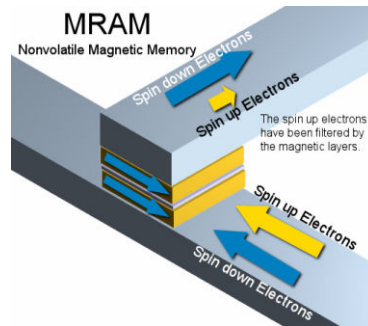
Figure 1.2: A schematic representation of magnetoresistive random-access memory (MRAM), which is based on the principle of GMR.

One of the major challenges in the field of spintronics was the search for materials which could combine semiconducting properties (for information processing) with robust magnetism (for information storage and retrieval).

It is now a well known fact that in order to make realistic applications feasible, spintronics require robust materials that show magnetic ordering at and above room temperature. One of the 125 critical unanswered scientific questions posed in Science[5] a few years back was, "Is it possible to create magnetic semiconductors that work at room temperature?" The hope for high T_C values, predicted by Dietl *et al.*[6], in some materials such as (Ga,Mn)N and (Zn,Mn)O could not be further substantiated by either experimental or theoretical studies. For a long time the major focus of spintronics research was on homogeneously diluted magnetic systems (magnetic atoms randomly distributed on the host lattice), without taking into consideration other possibilities such as metallic inclusions or simple concentration modulation. It was firmly believed that materials devoid of any kind of defects or inhomogeneities would ideally lead to room-temperature ferromagnetism. Unfortunately this proposition could not be realized in practice.

This led to more intensive research in other possible directions in the ultimate quest for room-temperature ferromagnetism. Experimental studies using transmission electron microscopy revealed the presence of coherent Mn-rich spherical nanocrystals in (Ga,Mn)As[7, 8], which exhibited a Curie temperature of 360 K. Similar Mn-rich clusters were also reported in (Ga,Mn)N by applying synchrotron radiation microprobe analysis[9]. In this case, the hexagonal symmetry of the host lattice was found to be preserved in both cluster-free and Mn rich regions. This kind of nanoscale spinodal decomposition into regions with high and low concentration of magnetic ions was speculated to be the possible reason for the apparently high Curie temperatures. Hence this led to the idea that nanoclusters formation could lead to promising materials for next generation spintronics. Nevertheless, the fabrication of such structures, typically of the order of a few nanometers, was not so simple a task. Self-assembled growth of nanoclusters on a periodic surface was shown to be a reliable approach[10]. However, the growth of ordered nanocluster arrays with identical size and adjustable composition was even more challenging.

In a very interesting study, Long Li and co-workers[11] showed that it was possible to obtain periodically ordered nanocluster arrays on a Si(111) sub-
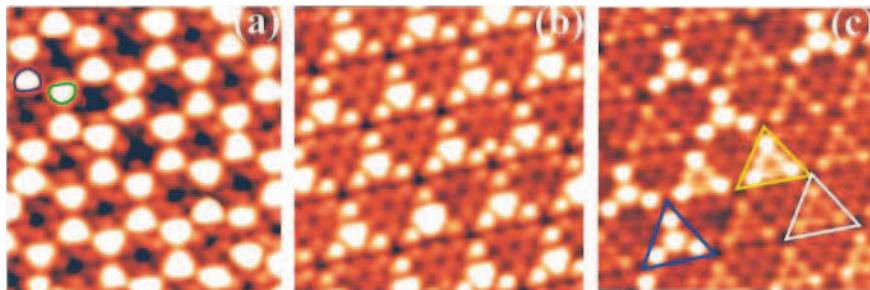
Figure 1.3: (a) Mixed array of equal-size In and Mn clusters, (b) Identical In/Ag alloy cluster array, and (c) STM image for the surface with low In/Ag coverage, demonstrating that the nanoclusters in (b) are In/Ag alloy. (From Ref.[11]).

strate by delicate control of the growth parameters. The substrate-induced spontaneous clustering was believed to be responsible for this. Figure 1.3(a) shows a complex array of two equivalent In and Mn cluster triangular lattices formed by depositing Mn on a pre-existing array of In clusters. The blue semi circle highlights the In cluster, and the green semi circle highlights the Mn cluster. Instead of Mn if Ag is deposited an array of identical sized In/Ag alloy clusters were formed, as shown in Figure 1.3(b). The In cluster array were found to dictate the growth of the Ag cluster array. This feature was illustrated at lower In/Ag coverage where the In clusters appear as a three-spot triangle indicated by the yellow triangle in Figure 1.3(c), while the In/Ag alloy clusters show four-spot triangles (indicated by the blue triangle). A high thermal stability of the ordered nanocluster arrays was also observed. Hence this method was shown to be very efficient for fabricating uniform nanocluster arrays with atomic precision.

In another recent study, based on scanning tunneling microscopy (STM), the structural transformation of heavily boron-doped diamond[12] was observed. On the surface of diamond films, grown by chemical vapor deposition (CVD), boron induced insulator-to-metal transition was found to facilitate the self-assembly of spatially ordered uniform-sized nanocrystals. Fig-
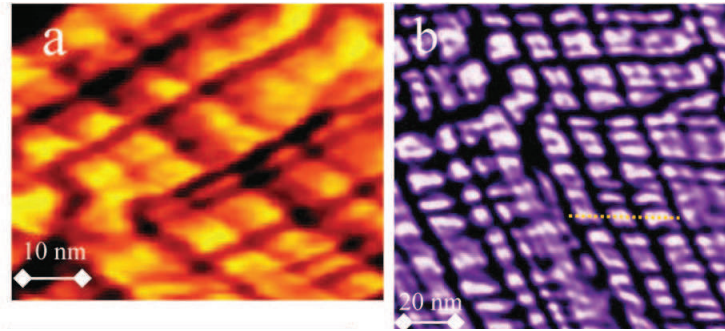
Figure 1.4: STM images on the surface of boron-doped diamond microcrystals. The image sizes are (a)620×500 Å^2, and (b)1300×1300 Å^2. (From Ref.[12]).

ure 1.4 show the STM images obtained on the top surface of such diamond microcrystals. In the figure we can see periodically ordered parallelogram-shaped nanoscale diamond grains. The formation of these periodic super structures was believed to be caused by the Fermi-sea-induced quantum electronic growth mechanism. This study of uniform-sized nanocrystals on the surface of boron-doped metallic diamond, demonstrated that the interplay of structural and electronic properties of materials is greatly enhanced at the nanometer scale.

Hence we see that the formation of inhomogeneous structures, at the nanoscale, is indeed possible. With the advent of efficient growth techniques the manipulation of the structure and composition of these nano-arrays can also be controlled. Now, from the fundamental point of view, it would be very interesting to observe the correlations of these inhomogeneous structures with different physical properties in disordered systems.

1.2 Signature of inhomogeneities in a wide variety of materials

The presence of inhomogeneities has been often detected in several disordered materials, such as manganites, diluted magnetic semiconductors (DMSs), superconductors, and many more. The formation of these inhomogeneous structures in these materials can be due to several reasons. For example, in the case of DMSs the out-of-equilibrium growth techniques, such as molecular beam epitaxy (MBE), required to grow the samples can lead to the formation of metastable phases. These phases can show high concentrations of magnetic atoms locally, and at the same time be coherent with the surrounding matrix. In manganites, they can arise due to the interplay between the charge, spin, orbital, and lattice degrees of freedom. This can lead to the coexistence of metallic and insulating phases in the system. It can also lead to the formation of Griffiths phases, which in turn can cause anomalous behavior of the magnetic susceptibility above the critical temperature. Hence the presence of such inhomogeneities, of the nanoscale order, cannot be completely ignored in these disordered magnetic systems. These heterogeneous structures can give rise to rich and interesting properties in these materials. The physics of these inhomogeneous materials is complex and interesting at the same time, from a fundamental point of view. It is due to this reason that these inhomogeneous disordered systems have started to attract considerable interest recently. In the following we give a brief overview of the effects of inhomogeneities observed in a wide variety of disordered magnetic systems.

1.2.1 High T_C Superconductors

Superconductors are one of the most widely studied materials in condensed matter physics. These materials can conduct electricity with almost no resistance, but only at sufficiently low temperatures. The discovery of high temperature superconductivity in copper oxides (better known as cuprates) led to extensive research in these materials, both from the theoretical as well as experimental point of view. The applications are widespread, for example

superconducting wires can be used for lossless power transmission. They can also be used to built very powerful electromagnets, which are used in MRI scanners. However, the origin of high-temperature superconductivity still remains unclear as several mechanisms have been proposed, as well as the search for room-temperature superconductivity remains one of the primary goals in this field.
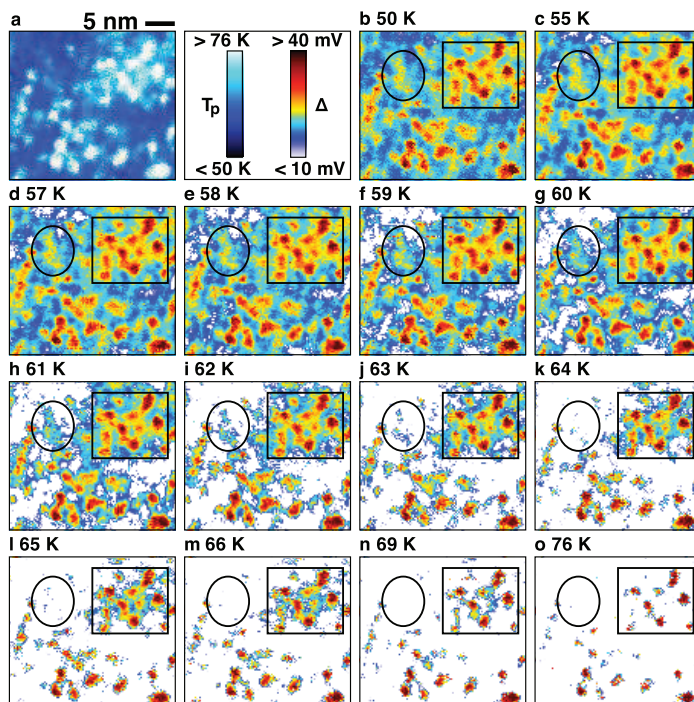
Figure 1.5: Evolution of the superconducting gap distribution with temperature in $Bi_2Sr_2CaCu_2O_{8+\delta}$. (a) Map of the local pairing temperature (T_p). (b)–(o) A 25×28 nm "gap-map" taken at different temperatures showing the distribution of gaps in real space. (From Ref.[13]).

In a recent study[13] Parker et $al.$ used scanning tunneling microscopy (STM), to focus on the interplay between naturally inhomogeneous nanoscale regions in the high-temperature superconductor $Bi_2Sr_2CaCu_2O_{8+\delta}$. Figure 1.5(a) shows the spatial distribution of the local pairing temperature T_p for this material. T_p is determined from the sequence of images in Figure 1.5(b)–(o) by finding the temperature above which there is no maximum in

the conductance on the positive bias side. Figures 1.5(b)–(o) show the spatial distribution of the gaps in a 25×28 nm grid at fourteen different temperatures from 50 to 76 K. It is found that regions of the sample with a small gap magnitude surrounded by larger gapped regions (the box in the upper right side of the panels) survive to higher temperatures compared to regions with similar gap sizes bordered by smaller gapped regions (the oval shaped region in the upper left of the panels). In other words, regions with weak superconductivity can persist to higher temperatures if bordered by regions of strong superconductivity. These measurements show that nanoscale inhomogeneous regions can affect each other via the proximity effect. The authors speculate that the collapse of superconductivity is caused not just by local thermal pair breaking, but also with phase fluctuations. The possibility of increasing the maximum transition temperature by the controlled distribution of dopants is also suggested.

1.2.2   CMR compounds: The manganites

Another class of materials which have been extensively studied over the last few decades is manganites of the type $R_{1-x}A_xMnO_3$, where R is a trivalent rare-earth ion and A is a divalent alkaline-earth ion such as Ca^{2+}, Sr^{2+}, Ba^{2+}. As a result of the substitution of R^{3+} by A^{2+} disorder as well as local distortions are induced. A metal-insulator transition (MIT) is found to occur for intermediate doping ranges in these rare-earth manganites. The phenomenon of colossal magneto-resistance (CMR), observed in these materials, helped to draw even more attention.

In Ref.[14], the authors have used scanning tunneling spectroscopy (STS) to study single crystals and thin films of $La_{1-x}Ca_xMnO_3$ (LCMO), which is is known to exhibit CMR behavior. Figure 1.6 shows the STS images of a thin film of $La_{0.7}Ca_{0.3}MnO_3$ taken just below the critical temperature, for different magnetic fields between 0 and 9 T. We can see the inhomogeneous nature of the local electronic structure, showing the coexistence of metallic (ferromagnetic) and insulating (paramagnetic) regions, with intermediate regions as well. The typical size of these intermediate regions were found to
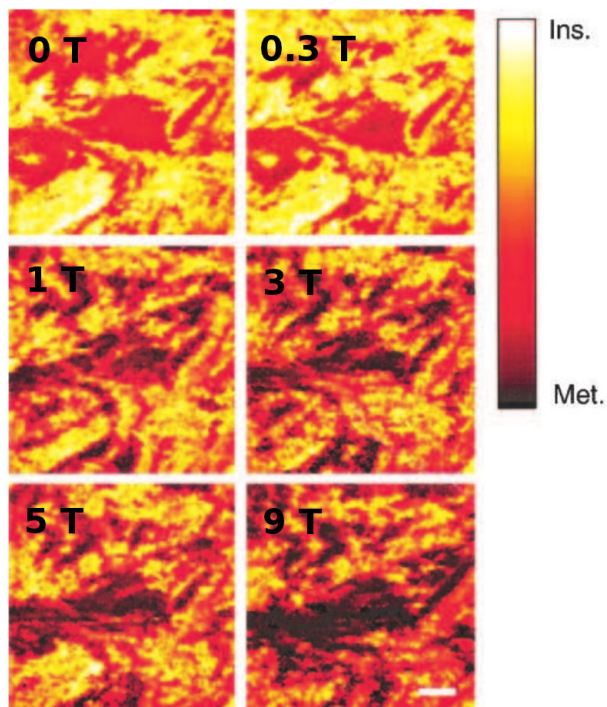
Figure 1.6: STS images of the local electronic structure of $La_{0.7}Ca_{0.3}MnO_3$ taken just below T_C in magnetic fields from 0 to 9 T. Light (dark) colors correspond to the insulating (metallic) parts of the surface. (From Ref.[14]).

be few tens of nanometers. Thus, below T_C a phase separation is clearly observed. In addition a strong field dependence was also found, when on increasing the magnetic field a significant proportion of the insulating regions (light color) could be converted into metallic regions (dark color). These results suggested that the MIT and the associated CMR behavior should be interpreted in terms of a percolation of metallic ferromagnetic domains.

In a more recent study[15], Tao et $al.$ studied the mixed-phase regions in the phase diagram of LCMO (at x=0.45), using scanning electron nanodiffraction techniques. At x=0.45, LCMO exhibits a CMR effect around the transition temperature from the ferromagnetic(FM) ground state to the paramagnetic(PM) state. A third mixed-phase is also found to coexist here, which

19
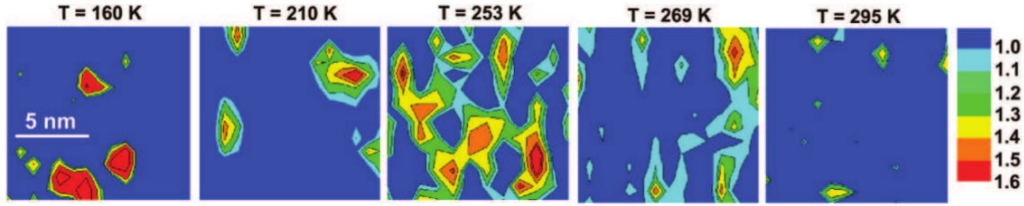
Figure 1.7: Intensity maps of the superlattice reflections in $La_{0.55}Ca_{0.45}MnO_3$ at different temperatures moving across FM-PM phase transition. Each map is from an area of 12×12 nm^2. (From Ref.[15]).

is characterized by unique superlattice reflections having a correlation length of a few nanometers. Figure 1.7 shows the intensity images of these super-lattice reflections in $La_{0.55}Ca_{0.45}MnO_3$, as the temperature is raised through the FM-PM transition. The mixed-phase clusters were found to be $\sim 3-4$ nm in diameter from the images. In the figure we observe that the density of these clusters is maximum at T=253 K. This was found to coincide exactly with the maximum in the CMR effect. The volume fraction of this nanoscale mixed-phase was found to peak at the CMR critical temperature and was sufficiently large to make a significant contribution to the CMR peak. The authors also argued that this nanoscale mixed-phase did not originate from chemical inhomogeneities.

1.2.3 A novel class of materials: The Topological Insulators

A fairly new class of electronic materials which has generated tremendous interest recently is the topological insulators[16]. These materials resemble ordinary insulators with a similar bulk band gap but surprisingly allows metallic conduction on their surface or edges due to the presence of topologically protected conducting states. These novel states arise due to the combination of spin-orbit interactions and time-reversal symmetry. Topological surface states were detected in several compounds such as $Bi_{1-x}Sb_x$, Bi_2Se_3, Bi_2Te_3, and Sb_2Te_3 by angle-resolved photoemission spectroscopy

(ARPES). This new class of states were found to be helical Dirac fermions, which are massless relativistic particles with their intrinsic spin locked to the linear momentum. These materials can have huge potential for applications in spintronics and quantum computation if superconductivity or magnetism is induced on the surface sates via proximity effect and doping. However, this requires a better understanding of the local electronic properties of these sates at the Dirac energy of their band structure.
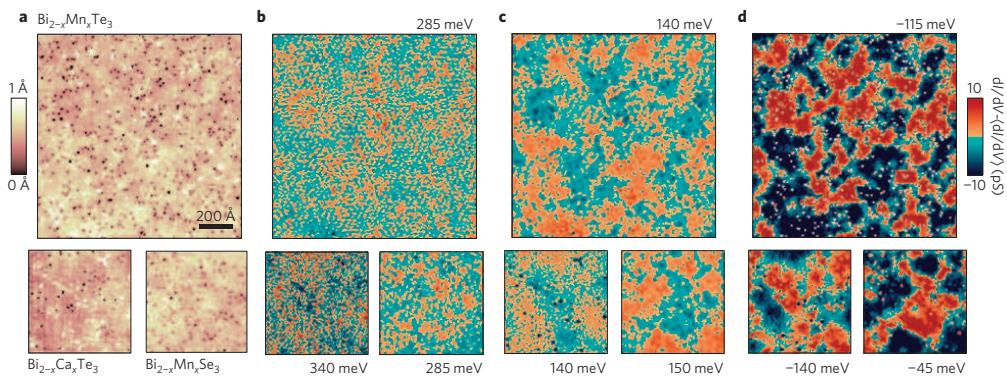
Figure 1.8: (a) STM images on the surface of Mn and Ca doped Bi_2Te_3 and Mn doped Bi_2Se_3. (b)-(d) Conductance maps taken at high, intermediate and low sample biases. (From Ref.[17]).

In a very recent study[17] by Beidenkopf *et al.*, spectroscopic mapping with STM was used to study the response of these surface states to magnetic and non-magnetic bulk doping in Bi_2Te_3 and Bi_2Se_3. Distinct nanoscale spatial fluctuations of energy, momentum and helicity were observed close to the Dirac energy. Figure 1.8(a) shows the STM topography for $Bi_{2-x}Mn_xTe_3$, $Bi_{2-x}Ca_xTe_3$, and $Bi_{2-x}Mn_xSe_3$. Figures 1.8(b)-(d) show energy resolved conductance (dI/dV) maps for the corresponding samples at different energies. The bulk doping leads to spatial interference patterns which can be seen in the conductance maps in Figure 1.8(b) and (c). In Figure 1.8(d) we observe that the conductance maps, at low energies, are rather controlled by an inhomogeneous nature of the local density of states, which vary on a typical length scale of a few tens of nanometers. These features were found to

21

be present irrespective of the fact whether the dopants were magnetic or not. The authors also found that on tuning the chemical potential to the Dirac energy the surface states electronic structure oscillates between electron-like and hole-like doped regions which have opposite helicity. It was concluded that the topological surface states are sensitive to charge inhomogeneities induced due to the bulk doping, and a reduction of this bulk charge defects is required in order to tune the chemical potential to the Dirac energy and to achieve high carrier mobility of these surface states, for making potential applications feasible.

1.2.4 Diluted magnetic semiconductors

It can be safely said that the field of DMSs has continued to attract considerable interest ever since the first report of ferromagnetism in (In,Mn)As in 1992[18]. This is true even today despite the discovery of several novel materials in the past few years. However, the ultimate goal to achieve room-temperature ferromagnetism in these materials has continued to elude researchers for a very long time. Room-temperature would hugely enhance their potential application in the field of spintronics.

Only recently, Jamet and co-workers[19] reported a high T_C ferromagnetic phase in the Group IV semiconductor (Ge,Mn) for a Mn content of 6%. The Curie temperatures were found to be higher than 400 K. A careful structural analyses, in this case, revealed the Mn distribution to be strongly inhomogeneous, with the formation of self assembled Mn rich nanocolumns. Figure 1.9 shows the transmission electron microscopy (TEM) images of the (Ge,Mn) thin film, where we can clearly see these nanocolumns extending throughout the whole sample. The average diameter of the nanocolumns were reported to be 3 nm and their spacing 10 nm. Magnetotransport transport measurements showed a large anomalous Hall effect up to room temperature, and a giant positive magnetoresistance was also found. The high Curie temperature was attributed to the formation of these nanocolumns, however the exact origin of ferromagnetism inside the columns was not clearly understood. Similar kind of inhomogeneous structures have also been detected
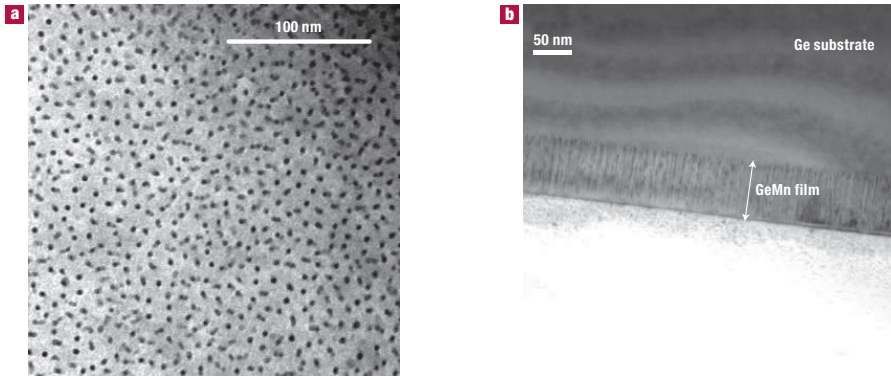
Figure 1.9: TEM images of a $Ge_{0.94}Mn_{0.06}$ film. (a) Plane view where the dark spots are nanocolumns. (b) Cross-sectional view, where the nanocolumns are the dark lines which appear perpendicular to the film plane. (From Ref.[19]).

in other diluted systems such as (Ga,Mn)N, Zn(Cr,Te), and (Zn,Co)O. The effects of these will be discussed later in the manuscript.

Hence we see that the existence of inhomogeneities can indeed give rise to a myriad of interesting properties in a wide variety of materials. With the latest advancements in growth techniques, the formation of these inhomogeneities can be controlled to a fairly good extent. However, a proper understanding of the origin of these effects still remains an open issue on the theoretical front. This serves as the primary motivation behind the research work we are going to present in a major part of this thesis.

1.3 An Overview of the Present Work

This work is mainly devoted to the study of nanoscale inhomogeneities in diluted magnetic systems. But first and foremost, one has to take into account the disorder effects in these diluted systems properly. The failure of this might lead to an incorrect estimation of the physical properties. The importance of disorder and percolation, and the need for a reliable tool for a proper treatment of these effects will be discussed in Chapter 2. The self-consistent local random phase approximation (SC-LRPA) is shown to be the best available method in this context. We will provide a detailed account of the spin excitation spectrum in the diluted nearest-neighbor Heisenberg model, within the SC-LRPA. It will be seen that the percolation threshold can be reproduced accurately within this approach. Chapter 3 would deal with a minimal model study of diluted magnetic semiconductors in general. We lay special emphasis on the particular case of (Ga,Mn)As. The Curie temperatures and the magnetic excitations of optimally annealed (Ga,Mn)As is calculated within this simple model. The results obtained are in excellent conformity with first-principles based calculations as well as experimental data. The model is shown to bridge the gap between first-principles based studies and minimal model approaches. Following this we come to the more important and exciting part of this work, which deals with nanoscale inhomogeneities. In Chapter 4 we present an elaborate and comprehensive study on the effects of inhomogeneities on the magnetic properties of diluted systems from a generalized perspective. The possibility of room-temperature ferromagnetism in these materials is put forward. Some discrepancies between theoretical predictions and experimental data are clarified as well. In addition, we will try to provide a plausible explanation of the various interesting effects observed on the temperature dependent magnetization, magnon excitation spectrum, and the spin-stiffness. The essential role of the relevant physical parameters are discussed. We finally conclude with the important findings of this research summarized in Chapter 5 and discuss the possible future directions that this work presents.

Chapter 2

Disorder effects and percolation in diluted magnetic systems

2.1 Introduction

Disorder in magnetic systems has been one of the prime areas of interest in condensed matter research over the last few decades. A significant amount of work was previously done to study the disorder effects in metals and nonmagnetic semiconductors[20, 21]. However, the effects of disorder and the role it plays in the transport and magnetism in diluted magnetic systems has attracted considerable interest from both the fundamental point of view as well as the exciting prospect of technological applications, in recent times. Disorder effects can arise due to several reasons in a wide class of materials. As for example in transition metal alloys like Fe_xNi_{1-x}, Fe_xCo_{1-x}, Ni_xCu_{1-x}, two types of atoms randomly occupy the lattice sites[22, 23, 24, 25] giving rise to disorder. The substitution of a non-magnetic atom by another one with a different size and/or valency induces disorder in manganites $R_{1-x}A_xMnO_3$ (where R is a rare earth element and A is a divalent alkaline earth metal)[26, 27, 28, 29, 30]. This leads to a metal-insulator phase transition, unusual behavior of the magnetic excitation spectrum, or even formation of inhomogeneities in these materials. A relatively new class of materials known as d^0 compounds (HfO_2, ZrO_2,

TiO$_2$), are reported to exhibit high Curie temperatures even in the absence of any magnetic impurities[31, 32, 33, 34, 35, 36]. This is attributed to the formation of intrinsic defects, such as vacancies, during the growth process of these materials. The random spatial distribution of magnetic impurities in a non-magnetic matrix gives rise to disorder effects in the widely studied diluted magnetic semiconductors, such as In$_{1-x}$Mn$_x$As, Ga$_{1-x}$Mn$_x$As, Zn$_{1-x}$Cr$_x$Te, Ge$_{1-x}$Mn$_x$. Also relevant in these materials is the formation of intrinsic defects, like Mn interstitials and As antisites in Ga$_{1-x}$Mn$_x$As, due to the non-equilibrium growth conditions. The Curie temperatures as well as other magnetic and transport properties are found to be very sensitive to the presence of disorder[37].

Another very important aspect of diluted magnetic systems which needs particular attention is the percolation phenomenon. A formal study of percolation thresholds can be traced back to 1957 when Broadbent and Hammersley[38] introduced a simple "lattice percolation" model for the flow of fluid through a static random medium. They showed that no fluid will flow if the concentration of active medium is smaller than some non-zero threshold value. The most common statistical assumptions considered were the *bond percolation* model and the *site percolation* model. In the former, when a fraction of the bonds, randomly distributed, are absent in the lattice no fluid can flow through them. While in the latter, if a fraction of the sites are missing, no current can flow through any of the bonds which join these sites to their respective neighbors. In order to describe this picture, the authors consider a lattice containing N sites, where N is a large number. The concentration of 'allowed' sites is given by x, and the quantities relevant to percolation depend upon this concentration and the geometry of the lattice. For a low concentration, $x \ll x_c$, the allowed sites appear in small isolated clusters. On increasing x, larger clusters occur and the mean size of a cluster increases monotonically. In the limit $N \to \infty$, as x approaches x_c, the bigger clusters begin to merge and the mean cluster size diverges at x_c. This leads to the fact that for any finite N, there is a fully connected path of allows sites extended over the system which makes the flow through the system possible. For $x \gg x_c$ and for a sufficiently large N, it is believed that only one large

26

cluster exists with other small ones. The ratio of the number of sites in this single large cluster to the number of sites in the lattice is defined as the site percolation probability $P^{(s)}(x)$. This represents the fraction of the volume of the system in which conduction is allowed. $P^{(s)}(x)$ was found to follow a simple power law, near the threshold, given by

$$P^{(s)}(x) \propto (x - x_c)^s \tag{2.1}$$

where s was found to be approximately the same for all three lattices (simple cubic (sc), body-centered cubic (bcc) and face-centered cubic(fcc)), $0.3 \leq s \leq 0.4$. The threshold concentrations, x_c, satisfying the above power law form were found to be 0.312 ± 0.002, 0.248 ± 0.003, and 0.2 ± 0.002 for sc, bcc, and fcc lattices respectively[39, 40].
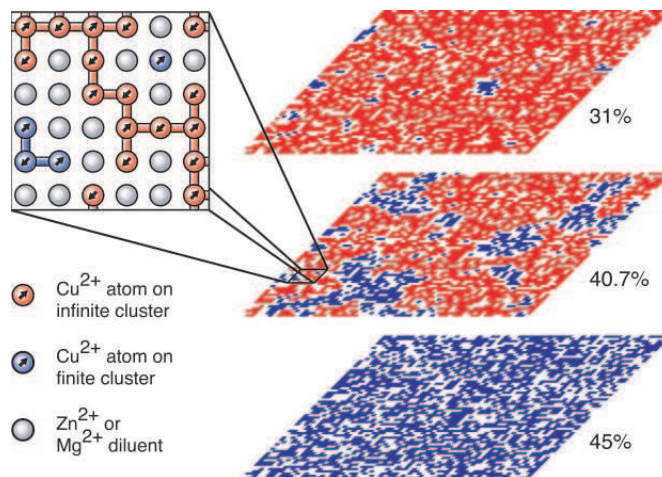
Figure 2.1: Schematic representation of finite-sized sections of an infinite square lattice for $La_2Cu_{1-x}(Zn,Mg)_xO_4$, for different site dilution levels. Inset: Close-up view for $x=40.7\%$, showing the role of magnetic Cu ions and non-magnetic Zn/Mg ions. (From Ref.[41]).

The problem of magnetic percolation appears to be of significant importance in disordered and diluted systems. For example in a clean system, when the concentration of impurities is 100%, there is a perfect ferromagnetic network. However, on dilution this network is weakened and for concentrations

below a certain percolation threshold the ferromagnetic ordering ceases to exist in the system, since due to missing longer ranged interactions the moments cannot align anymore. For example in the nearest neighbor Heisenberg model the percolation threshold, x_c, is known to be 20% for the fcc lattice. But in realistic diluted systems, such as DMSs, the relevant concentration range is much lower than 20%, and it is the weaker and more long ranged interactions that dominate the ferromagnetism instead of the strong nearest-neighbor couplings. This implies that the real percolation threshold should also be lower in this case. As we shall see later, the improper treatment of the percolation effects can lead to strong overestimations of the Curie temperatures and other magnetic properties of these systems. In this context it is also interesting to note the case of the spin-1/2 two-dimensional Heisenberg anti-ferromagnet $La_2Cu_{1-x}(Zn,Mg)_xO_4$. It was shown to be a model example of a 2D quantum antiferromagnet, for square-lattice site percolation[41]. Here both Zn^{2+} and Mg^{2+} are nonmagnetic, and they do not introduce any charge carriers on substitution. It was found that this nearest-neighbor square lattice undergoes a structural transition with dilution x, in the absence of quantum fluctuations, at the percolation threshold $x_p \approx 40.725\%$. As can be seen in Figure 2.1, below x_p there is an infinite cluster of connected sites. On approaching the percolation, more disconnected clusters are found to appear and above x_p the lattice is fully spanned by finite-sized disconnected clusters. The possibility of a quantum critical point below the percolation threshold was ruled out in the extreme quantum limit of $S=1/2$.

Hence we see that disorder effects and percolation appear to be very important in these systems. A proper treatment of these effects calls for a reliable and accurate tool. Among the available theoretical approaches, the Monte Carlo (MC) calculations are widely considered as exact. The disorder effects are treated exactly as well as the spin fluctuations are properly accounted for, within the MC studies. Although powerful, this approach has some deficiencies when it comes to the study of diluted systems. For example it is restricted to relatively small system sizes and the calculations are expensive in terms of computational resources. We shall discuss this in more detail a little later.

28

2.2 Which Theoretical Approaches to handle large scale systems

Now we discuss some of the theoretical methods that have been applied to study the role of disorder and to calculate the magnetic properties of diluted magnetic systems in general. These approaches are an alternative to the *in principle* exact MC studies. We discuss the pros and cons of these methods with respect to the treatment of disorder and spin fluctuations, and the reliability of their predicted results.

2.2.1 The basic Mean Field Approximation

The mean-field theory was originally proposed by Weiss[42] for the case of ferromagnetic systems without disorder. The main idea is to describe the interactions between the magnetic atoms in terms of an average or effective interaction, known as a *molecular field*. Thus the effective field acting on all the particles of the system is identical. This oversimplification has some advantages in the sense that it can provide a basic understanding of the magnetism at a fairly low cost. However, this approach has several shortcomings, like the spin fluctuations (thermal and transverse) are underestimated and the Mermin-Wagner theorem[43] and the Goldstone theorem[44] are not fulfilled. Moreover the Curie temperatures calculated within the mean-field theory often results in strong overestimations in most cases.

One of the most frequently used and often cited studies in DMSs is based on the mean-field treatment of the Zener model[6]. The thermal as well as transverse fluctuations of the impurity spins and the charge carriers are treated within the mean-field theory. The disorder in this case is handled within the Virtual Crystal Approximation (VCA). This is also sometimes referred as the 'average lattice model' or 'continuous media approximation'. The VCA treats the potential experienced by an electron as the average of the two extreme elements where the concentration of impurities is given by $x=0$ and $x=1$ respectively. The multiple scattering effects on the impurities are not considered and the percolation effects are not taken into account. Also

the couplings between the localized impurity spins and the charge carriers are treated in a perturbative manner. These approximations led to the prediction of above room temperature ferromagnetism in (Ga,Mn)N and (Zn,Mn)O for 5% Mn content[6]. Unfortunately, this could not be realized till date. The Curie temperature within the mean-field(MF) VCA is given by the following expression

$$T_C^{MF-VCA} = \frac{2}{3}S(S+1)x\sum_i J_{0i} \tag{2.2}$$

where x is the concentration of magnetic impurities and J_{0i} is the effective exchange interactions (see Appendix A). As one can clearly see, the expression does not take into account the nature or the range of the exchange interactions. This is of particular importance in diluted systems where the T_C's and other magnetic properties are mainly determined by the exchange interactions close to the average separation between the magnetic impurities and the nearest-neighbor interactions are not so important. The MF-VCA, on the other hand, treats all interactions on an equal footing, thus giving an undue importance to the nearest-neighbor interactions in the dilute limit. This leads to the strong overestimations in the Curie temperatures and other relevant properties.

2.2.2 The effective medium approach: Coherent Potential Approximation

The Coherent Potential Approximation (CPA) is a single-site effective medium theory[45, 46, 47]. In the CPA, this effective medium is given by a spin-dependent local self-energy $\sum_\sigma(\omega)$, which is determined from the condition that the averaged t matrix of a single impurity immersed in this medium is zero. This describes the configuration average properties of disordered systems. The average includes the spatial average over all sites of the system, including the random impurity positions, as well as the thermal average over the relative spin orientations. The method is built within the framework of multiple-scattering theory, and the electronic structure of the system is

described by the atomic t matrices, which include the multiple scattering effects off a single impurity. In the case of an alloy, for example $A_{1-x}B_x$, the scattering path operator τ is calculated from the atomic t matrix (t_{CPA}) corresponding to a hypothetical atom in the CPA medium. This is given by the weighted average of the single-site scattering path operators (τ_A and τ_B) in the effective CPA medium, which implies $\tau = (1-x)\tau_A + x\tau_B$. Now this is evaluated iteratively for a self-consistent t_{CPA}.
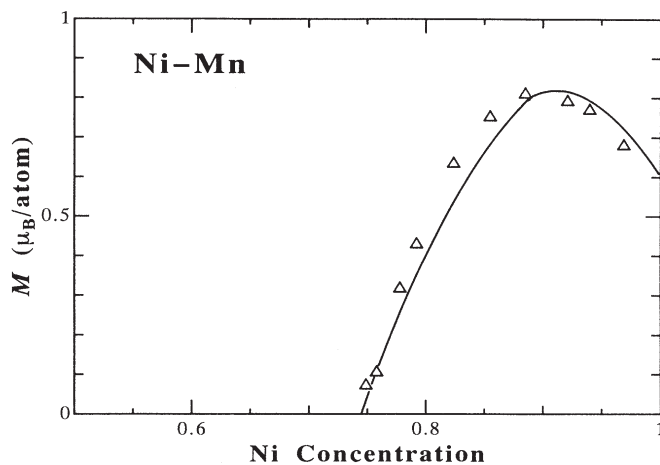
Figure 2.2: Magnetization of a Ni-Mn system, calculated within the KKR-CPA method, as a function of the Ni concentration. The triangles represent experimental data from Ref.[49]. (From Ref.[48]).

The CPA method has been used extensively in *ab initio* calculations, in combination with the Korringa-Kohn-Rostoker (KKR) method[51] and the linear muffin-tin orbital (LMTO) method[52], to successfully calculate the properties of disordered magnetic systems like ferromagnetic alloys[48] as well as DMSs. Figure 2.2 shows the average magnetization of a Ni-Mn alloy[48] calculated from the KKR-CPA method in combination with the local spin density formalism. This shows that the CPA can reproduce the observed magnetization quite well and can describe the average quantities with good accuracy. A detailed review of the first principle calculations of DMS properties based on the KKR-CPA and LMTO-CPA can be found
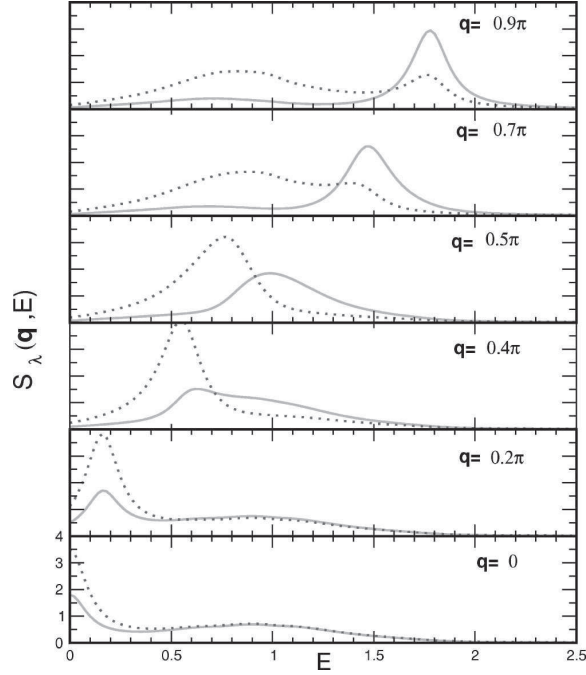
Figure 2.3: Spectral function $S_\lambda(\mathbf{q}, E)$ of a binary alloy $A_{1-c}B_c$ as a function of energy for different momenta $\mathbf{q}$, where $\mathbf{q}=(1,1,1)$, calculated within the RPA-CPA method. The solid (dashed) lines correspond to λ=A (λ=B). (From Ref.[50]).

in Ref.[53]. The advantages of the method are that it is relatively fast, and is able to handle arbitrary concentration levels. However, due to the single-site approximation in the CPA it is not able to account for the short range order and the localization effects are neglected. This could prove to be a severe limitation especially in the case of diluted systems. Also the spatial distribution of defects cannot be described due to the effective medium approach.

The CPA was combined in a self-consistent manner with the random phase approximation (RPA) to study the magnetic properties in disordered

Heisenberg systems with long-range exchange integrals[50]. The RPA is based on the Green's function formalism using the Tyablicov decoupling procedure[54] and is already known to be reliable for evaluating the magnetic properties of clean ferromagnetic systems. The advantage of this approach is its ability to treat quantum fluctuations, as well as the fact that it satisfies both the Mermin-Wagner and the Goldstone theorems, which is not possible within the mean-field approach. In Ref.[50], the authors generalize the RPA to the case of disordered binary systems and the disorder effects are treated within a modified cumulant CPA approach. The advantage of the cumulant expansion method[55, 56] is its ability to tackle "environmental" disorder effects, which is a characteristic of Goldstone systems like phonons and magnons. By the simultaneous and self-consistent treatment of the RPA and CPA, the authors were able to calculate the Curie temperatures, spectral functions and the temperature dependent magnetization as a function of the impurity concentrations. Figure 2.3 shows the spectral function $S_\lambda(\mathbf{q}, E)$ of the disordered binary alloy $A_{1-c}B_c$ on a simple cubic lattice, as a function of the energy for different values of the momentum $\mathbf{q}$, calculated within the RPA-CPA theory[50]. The exchange integrals are restricted to nearest neighbor only. As can be clearly seen from the figure, at $\mathbf{q}=0$ there is well defined peak at $E=0$ in both the spectral functions corresponding to the atoms A and B. This is consistent with the fact that the theory satisfies the Goldstone theorem. For intermediate values of the momentum we see a single broad peak. We also note that the dispersion of the second peak is almost flat, whereas the Goldstone mode $E_1(\mathbf{q})$ shifts from $E=0$ to $E\approx 2$, when moving in the (111) direction. This spectral function can provide relevant information about the elementary spin excitations in the system and can be directly accessible by inelastic neutron scattering experiments. Although this approach proved to be promising for the study of disordered magnetic systems, it does not allow to include the effects of correlated disorder or the presence of inhomogeneities in the system.

2.2.3 The Self-Consistent Local Random Phase Approximation

From the previous approaches what we clearly understand is that the disorder effects have to be treated carefully and reliably in these systems. Thus it becomes imperative to go beyond a simplified approach, which can treat the disorder accurately as well as account for the thermal or transverse fluctuations, and the phenomena of localization and percolation in these diluted systems. In 2005, Bouzerar *et al.*[57] proposed a new method to calculate the Curie temperatures in III-V diluted magnetic semiconductors. Within this method, known as the self-consistent local random phase approximation (SC-LRPA), the spin fluctuations (thermal/transverse) are treated in the framework of the RPA, and the effects of disorder or dilution are treated exactly in real space. This method is essentially an extension of the standard RPA to the case of disordered systems. As we shall see throughout this manuscript, the SC-LRPA is a very efficient and powerful tool at the same time. This approach has several advantages like it is semi-analytical, fast and allows to reach large system sizes. Also the computational requirements are much less in comparison to the standard Monte Carlo methods. This method has been successfully implemented to calculate the magnetic properties of a wide class of magnetic systems from DMSs[57, 58, 59] to manganites[60] as well as the novel d^0 materials like HfO_2 and ZrO_2[35]. In the following we briefly discuss a few cases which demonstrate the accuracy of the method, when compared to the essentially exact Monte Carlo studies as well as experiments.

Comparison between SC-LRPA and Monte Carlo studies

In Figure 2.4 the Curie temperatures of (Zn,Cr)Te are shown as a function of the Cr concentration[58]. We notice that the T_C obtained within the mean field VCA (MFA-VCA) is almost always above the room temperature. On the other hand, the SC-LRPA and the Monte Carlo (MC) results yield much lower values of the Curie temperatures. The T_C's are strongly reduced due to the approach of the percolation regime. Moreover the calculated Curie
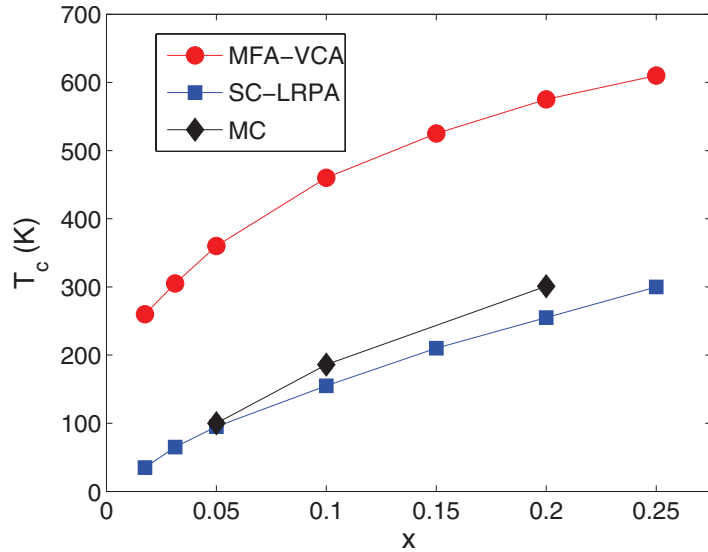
Figure 2.4: Curie temperatures of $Zn_{1-x}Cr_xTe$ as a function of x, within the MFA-VCA, SC-LRPA, and MC simulations. (From Ref.[58]).

temperatures are also in very good agreement with those obtained experimentally, for about 20% Cr content it was found that $T_C \approx 300$ K[61]. The MF-VCA strongly overestimates the T_C's as it does not take the disorder effects (percolation, localization) and the thermal fluctuations into account and hence is not a reliable tool to calculate the properties of these diluted systems. This again demonstrates the importance of disorder and the necessity to treat them reliably and accurately. The important thing to observe here is the excellent agreement between the exact MC results and the SC-LRPA values.

Comparison between *ab initio* based approach and experimental studies

Figure 2.5 shows the Curie temperatures for different samples of (Ga,Mn)As as a function of the Mn concentration (from Ref.[57]). The theoretical results are obtained using the SC-LRPA treatment of the disordered Heisenberg Hamiltonian, where the exchange couplings were calculated in the framework
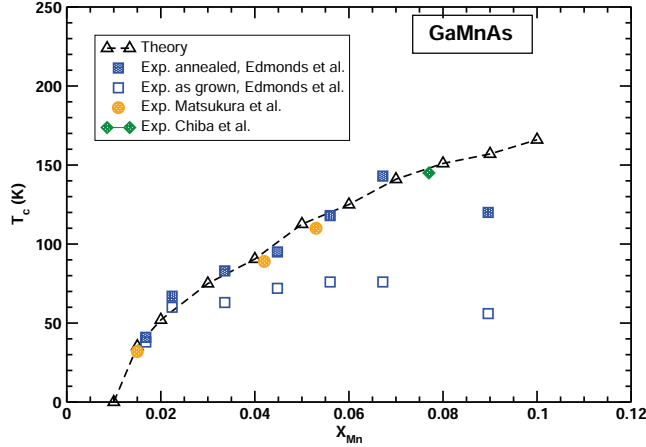
Figure 2.5: Curie temperature of $Ga_{1-x}Mn_xAs$ as a function of x. The triangles denote the calculated values within the SC-LRPA. The other symbols correspond to the experimental values. (From Ref.[57]).

of the tight binding linear muffin tin orbital (TB-LMTO) method of *ab initio* based studies assuming no compensating defects, such as Mn interstitials or As antisites. This corresponds to the case of *fully* or *optimally* annealed samples. As can be seen, an excellent agreement between the calculated Curie temperatures and those measured for optimally annealed samples is obtained for a wide range of Mn concentration. The exception being the case of 9%, for which the authors suggest that at this concentration the annealing is not complete. The theory also correctly predicts a percolation threshold, of about 1%, below which there is no ferromagnetism. Hence we see that this two-step approach, couplings obtained from *ab initio* studies combined with the SC-LRPA treatment of the effective Heisenberg Hamiltonian, could very well reproduce the experimentally measured Curie temperatures. Within this approach, disorder is treated in a reliable manner as is evident from the fact that the percolation threshold could also be reproduced.

2.3 Benchmarking an efficient self-consistent method

In this section we will see a few cases which further establish the accuracy and the reliability of the SC-LRPA in treating the disorder effects. The advantages of this method over the Monte Carlo calculations for diluted systems will also be demonstrated.

2.3.1 The one-band disordered Double Exchange model

We consider the simple case of a system of classical spins interacting with itinerant carriers, in the absence of any disorder[60]. The Hamiltonian which describes this is a one-band model on a simple cubic lattice given by

$$\mathcal{H} = -\sum_{ij\sigma}(t_{ij}c_{i\sigma}^{\dagger}c_{j\sigma} + hc) - J_H \sum_i \mathbf{S}_i \cdot \mathbf{s}_i \qquad (2.3)$$

where $t_{ij}=t$ for i and j nearest neighbors only, $\mathbf{S}_i$ is a classical spin localized at site i ($|\mathbf{S}_i|=1$), and $\mathbf{s}_i=c_{i\alpha}^{\dagger}(\boldsymbol{\sigma})_{\alpha\beta}c_{i\beta}$, ($\boldsymbol{\sigma}=(\sigma_x,\sigma_y,\sigma_z)$ are the Pauli matrices). This can be used to study systems like manganites ($R_{1-x}A_xMnO_3$, where R is a rare-earth element and A an alkaline element), where the dominant exchange mechanism is the double exchange. In the case of manganites, J_H represents the Hund coupling between the localized spins associated with the t_{2g} orbitals ($S=3/2$) and the itinerant carriers associated with the e_g orbitals. In the double exchange limit, $J_H S \gg W$ (W is the bandwidth) and J_H is set to infinity in the calculations.

Now a two-step approach (TSA) was adopted to study this model. In the first step the Hamiltonian given by Equation 2.3 is diagonalized in real space for a given configuration of disorder, assuming a fully polarized ground state at $T=0$ K. This leads to an effective Heisenberg Hamiltonian for classical
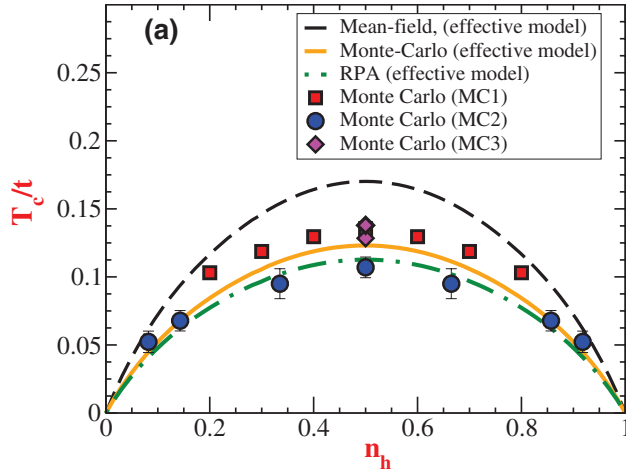
Figure 2.6: T_C for the double exchange model as a function of n_h corresponding to the clean case. The dashed, solid, and dot-dashed lines are obtained with the MF, MC, and RPA treatments, respectively. The symbols indicate the MC treatment of the full double exchange model. (From Ref.[60]).

spins

$$\mathcal{H}_{eff} = \sum_{\langle ij \rangle} J_{ij} \mathbf{S}_i \cdot \mathbf{S}_j \tag{2.4}$$

where the exchange couplings J_{ij} are calculated in the limit $J_H \to \infty$. In the double exchange limit, the couplings between the nearest neighbors, for a given hole density n_h, is given by

$$J(n_h) = \frac{1}{4} t \langle c_{i\uparrow}^\dagger c_{j\uparrow} \rangle \tag{2.5}$$

which can also be expressed as

$$J(n_h) = -\frac{1}{4z} \frac{\langle K \rangle}{N} \tag{2.6}$$

where the kinetic energy $\langle K \rangle$ depends on n_h and z is the lattice coordination number. The second step consists of treating the effective Heisenberg model

38

within the SC-LRPA scheme or by Monte Carlo simulations. Now the Curie temperature within the SC-LRPA is given by the following expression

$$T_C^{SC-LRPA} = \frac{1}{3}S(S+1)\frac{1}{N}\sum_i \frac{1}{F_i} \tag{2.7}$$

where the sum over i is for all sites (non-dilute regime), and

$$F_i = \int_{-\infty}^{\infty} \frac{A_{ii}(E)}{E} dE \tag{2.8}$$

The local quantity F_i have to be determined self-consistently at each temperature (more details can be found in Appendix B).

Figure 2.6 shows the Curie temperatures, corresponding to the clean case, as a function of the hole density in the double exchange model. The different lines represent the values obtained by treating $\mathcal{H}_{eff}$ within the mean-field theory ($T_C^{MF}(n_h)$=4$J(n_h)$), Monte Carlo simulations ($T_C^{MC}(n_h)$=2.88$J(n_h)$[62]), and the local RPA ($T_C^{RPA}(n_h)$=2.66$J(n_h)$[63]). We note that the SC-LRPA reduces to the standard RPA value (2.66$J(n_h)$) for the case of clean systems, where the T_C can be obtained analytically by the following formula

$$T_C^{RPA} = \frac{2}{3}S(S+1)\frac{1}{N}\left(\sum_{\mathbf{q}}\frac{1}{E(\mathbf{q})}\right)^{-1} \tag{2.9}$$

where $E(\mathbf{q})$=$zJ[1-\gamma(\mathbf{q})]$, and $\gamma(\mathbf{q})$=$\frac{1}{z}\sum_{\mathbf{r_i}}e^{i\mathbf{q}\cdot\mathbf{r_i}}$ (z is the coordination number). We observe that the RPA values are in fairly good agreement with those obtained from the Monte Carlo treatment of the effective Heisenberg model, while the mean-field approximation overestimates the Curie temperatures. Now this two-step approach is compared to the Monte Carlo treatment of the full double exchange model. This involves diagonalizing the Hamiltonian given by Equation 2.3, completely within Monte Carlo simulations without mapping to any effective Hamiltonian. This is denoted as FMC or the "Full Monte Carlo", to avoid confusing it with the Monte Carlo treatment of the effective Heisenberg Hamiltonian. The FMC method is expensive both in terms of memory as well as CPU time, but nevertheless it is considered in

principle exact. The symbols in Figure 2.6 denote the values obtained from FMC treatment of the double exchange model. We immediately observe an excellent agreement between the FMC treatment and the TSA adopted in this case. The difference between the results was found to be within 10%. This indicates the reliability of this approach in the case of ordered systems.
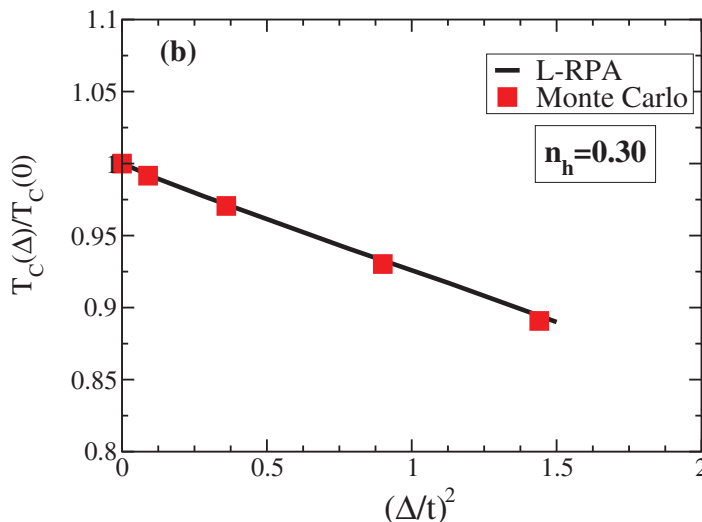
Figure 2.7: T_C for the double exchange model as a function of $(\Delta/t)^2$ (Δ is the on-site potential) for uncorrelated Anderson disorder. The solid line corresponds to the SC-LRPA and the squares represent values from MC simulations[64]. (From Ref.[60]).

Now in order to extend this study to the case of disordered systems, the following term is added to the Hamiltonian in Equation 2.3,

$$\mathcal{H}_{\mathcal{D}} = \sum_{i\sigma} \epsilon_i c_{i\sigma}^{\dagger} c_{i\sigma} \tag{2.10}$$

where ϵ_i are the random on-site potentials which may correspond to the chemical substitution of R^{3+} by A^{2+} in the case of manganites. The ϵ_i are uncorrelated variables and uniformly distributed within the interval $\left[-\frac{\Delta}{2}, \frac{\Delta}{2}\right]$. Now this is treated within the TSA where the effective Hamiltonian is diagonalized within the SC-LRPA. The results are compared with the FMC

simulations of the double exchange model in presence of disorder. Figure 2.7 shows the Curie temperature (scaled by $T_C(\Delta = 0)$) as a function of the square of the on-site potential width Δ, at a fixed hole density of n_h=0.3[60]. The calculations were performed on relatively large systems and a systematic average over a few hundred configurations of disorder were done for each value of Δ. As can be clearly seen from the figure, that the values obtained within the SC-LRPA treatment is found to be in excellent agreement with those obtained from the FMC treatment of the disordered double exchange Hamiltonian[64]. This shows that not only the thermal fluctuations but also the spatial fluctuations due to disorder are treated properly within this approach. At the same time this establishes the accuracy and the reliability of the SC-LRPA in the case of disordered systems as well.

2.3.2 Crucial role of Disorder and Thermal/Transverse Fluctuations

We now try to analyze the importance of disorder and thermal/transverse spin fluctuations and the role they play in determining the magnetism in disordered and diluted materials. For this we take the case of the Curie temperatures of the diluted magnetic semiconductor (Ga,Mn)As calculated within three different treatments of the disorder[57] as shown in Figure 2.8. The exchange couplings were obtained from the TB-LMTO approach, where the multiple scattering effects are treated within the CPA.

Now consider the equation of motion within the SC-LRPA (see Appendix B for details), which is given by

$$(\omega - h_i^{eff})G_{ij}(\omega) = 2\langle S_i^z \rangle \delta_{ij} - \langle S_i^z \rangle \sum_l J_{il} G_{lj}(\omega) \qquad (2.11)$$

where $G_{ij}(\omega)$ represents the Fourier transform of the retarded Green's function,

$$G_{ij}(t) = -i\theta(t)\langle [S_i^+(t), S_j^-(0)] \rangle \qquad (2.12)$$

and $\langle S_i^z \rangle$ and h_i^{eff} denote the local magnetization and the local effective field at each site, respectively. The second term on the right side of Equation 2.11 describes the transverse fluctuations. Ignoring this leads to what is denoted as "Ising-disorder" in Figure 2.8. This Ising-like mean-field theory
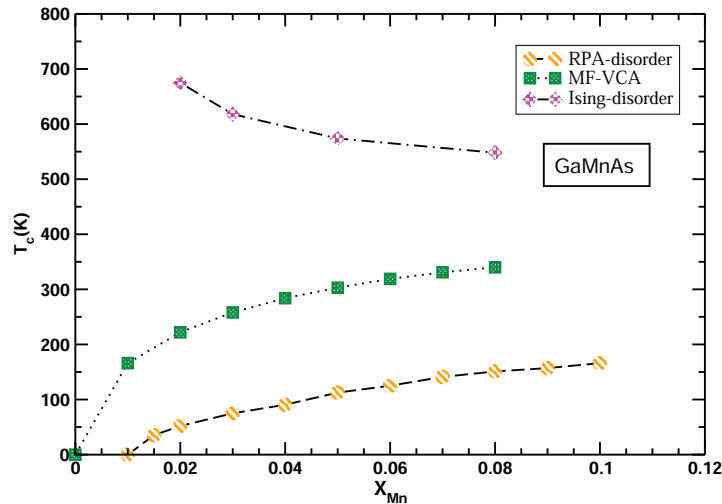
Figure 2.8: Curie temperature of (Ga,Mn)As as a function of x, for three different approximations , "Ising-disorder", MF-VCA, and the SC-LRPA. (From Ref.[57]).

includes the disorder effects correctly but does not take into account the transverse spin fluctuations. As we can clearly see from the above figure, this approximation leads to extremely high and unreliable Curie temperatures. This is due to the influence of the sites in large local effective fields due to the strong short-range ferromagnetic interactions. The second approximation is the MF-VCA, which also neglects the transverse fluctuations but the disorder is now treated as a simple effective medium. As discussed before, within the VCA all sites of the system are considered as equivalent. The MF-VCA largely overestimates the critical temperatures. For only about 5% of Mn, the Curie temperature is already found to exceed the room-temperature value. On the other hand, the SC-LRPA takes the transverse fluctuations into account and the disorder is treated exactly. The T_C's obtained within this approach are found to be strongly reduced in comparison to the other

approximations (almost three times less than the MF-VCA values). It should be noted that these values were found to be in good agreement with those obtained from Monte Carlo studies. We also observe that the self-consistent approach is able to predict a percolation threshold, of about 1%, below which the Curie temperature vanishes and there is no ferromagnetic order. This is beyond the scope of the mean-field like approximations.

Thus the relevance of disorder and thermal/transverse fluctuations are established and the need to treat them reliably and accurately is essential to give a correct account of the relevant properties of these systems. The SC-LRPA clearly has an upper hand over the other approaches. Within this approach the transverse fluctuations are treated within the RPA and the effects of disorder (percolation, localization) are properly taken into account.

2.3.3 Dramatic finite size effects and importance of proper statistical sampling

The Monte Carlo (MC) simulations are considered as a powerful and reliable tool to calculate the different properties of the diluted spin systems and the method is widely regarded as *in principle exact*. The spin fluctuations are taken into account and the disorder effects are treated exactly by means of configurational averaging over many disorder configurations. However, in the MC simulations a finite-size scaling of the data obtained is essential due to the limited size of supercells used in the calculations. Here we focus on the Curie temperature obtained within the MC methods in comparison with the SC-LRPA values in some realistic cases, and discuss the possible drawbacks of this method. Unlike the self-consistent approach, where the critical temperature is given by a semi-analytical formula, in the case of MC studies the Curie temperature needs to be extracted. In most of the cases this is done by using the cumulant crossing method, proposed by Binder[65]. In this method, the fourth-order cumulant U_4 of the order parameter, in this case the magnetization, is given by

$$U_4(T) = 1 - \frac{\langle M(T)^4 \rangle}{3\langle M(T)^2 \rangle^2} \qquad (2.13)$$

The thermal average of the magnetization and its associated powers are calculated within the Metropolis algorithm. Now U_4 is calculated for different lattice sizes and plotted as a function of the temperature. All the U_4 curves, corresponding to different sizes, cross each other at the temperature $T=T_C$. Thus the Curie temperature is extracted from this unique intersection point of the U_4 curves from different lattice sizes (usually three). Although accurate this method is costly in terms of computational time due to the need for finite size effect analysis. In some cases, it is also possible to extract the Curie temperature from the peak of average thermodynamic quantities like the specific heat or the susceptibility. However, this may not be reliable due to the change in the peak positions with the size of the system, and this calls for additional calculations with high statistical accuracy. This proves to be quite heavy in terms of both memory and CPU time. As we shall see in the following, in the case of dilute magnetic systems the finite size effects and proper statistical sampling appears to be of crucial importance.

In a recent study, Bouzerar and Bouzerar[66] adopted a two-step approach (TSA) to calculate the magnetic properties of dilute systems of localized spins interacting with itinerant carriers (holes/electrons), and the results were compared to those obtained from Monte Carlo (MC) studies. The minimal one-band model considered for this case is given by

$$H = -\sum_{ij\sigma} t_{ij} c_{i\sigma}^{\dagger} c_{j\sigma} + \sum_{i} p_i J_i \mathbf{S}_i \cdot \mathbf{s}_i + \sum_{i\sigma} \epsilon_i c_{i\sigma}^{\dagger} c_{i\sigma} \qquad (2.14)$$

The last term in the above equation is the on-site potential, which describes the disorder effects due to the substitution of a cation by another one. In this study, the last term is neglected. Now in the TSA, first the Hamiltonian (Equation 2.14) was diagonalized for a given configuration of disorder, at $T=0$ K assuming a fully polarized ground state. Following this the magnetic couplings between the localized spins is calculated from the spin resolved one-particle Green's functions of the itinerant carriers, and finally one ends up with the effective disordered Heisenberg Hamiltonian, same as the one discussed in Section 2.3.1. In this study, the magnetic couplings were provided by *ab initio* based calculations. In the second step, the effective

Heisenberg Hamiltonian is treated within the SC-LRPA. The authors found that in the case of clean systems (non-dilute) and in the double exchange regime, the finite size effects are completely negligible. This could explain the good agreement found between the TSA performed on relatively large systems ($N \approx 20^3$ sites) and the full MC calculations done for much smaller sizes ($N \approx 5^3$ sites) in clean cases. However, for diluted systems the finite size effects were found to be rather large. Hence using too small system sizes and an insufficient statistical sampling could affect the results in a drastic way.
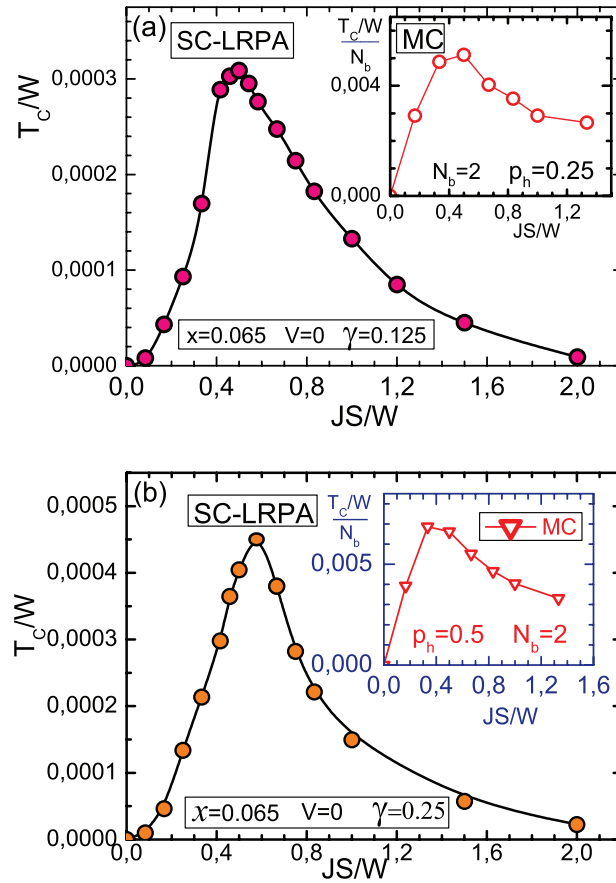
Figure 2.9: Curie temperature (in units of the bandwidth W) within SC-LRPA as a function of JS/W for a fixed $x=6.5\%$. The hole concentration per impurity is (a)$\gamma= 0.125$, and (b)$\gamma= 0.25$. The insets show the MC results for a two-band model ($N_b=2$) where the density of holes $p_h=2\gamma$. (From Ref.[66]).

45
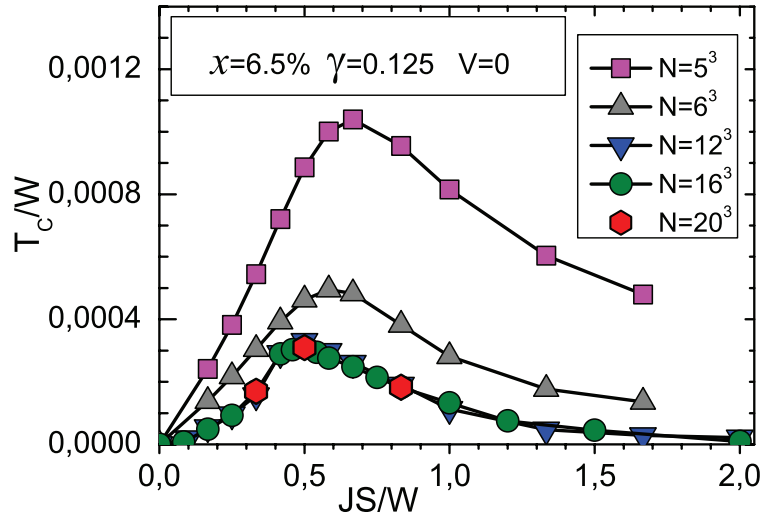
Figure 2.10: Curie temperature (in units of the bandwidth W) as a function of JS/W for different system sizes $N=L^3$, (L=5 to 20). (From Ref.[66]).

Figure 2.9 shows the Curie temperatures as a function of the local coupling JS, at a fixed concentration of magnetic impurities x=0.065, for two different hole concentrations per impurity, (a)γ= 0.125, and (b)γ= 0.25[66]. For both γ values, the T_C is found to increase with an increase in JS until it reaches a maximum, and then it gradually decreases again. The highest T_C values, as can be seen from the figure, are 3×10^{-4} and 5×10^{-4} for γ=0.125 and 0.25 respectively. The insets in the figure correspond to the full MC simulations of the diluted Hamiltonian (Equation 2.14) performed by Popescu et $al.$[67]. In this MC study, the authors considered a two-band model where each independent band is filled with a density of holes p. Hence in order to make a direct comparison with the TSA in the one-band model, the Curie temperature and the hole density from the MC calculations is simply divided by two. We immediately notice that for both carrier densities, the MC calculations yield much higher critical temperatures in comparison to the SC-LRPA values. The highest T_C values are almost 20 times larger than those predicted by the self-consistent scheme. We also observe a strong sup-

pression in these T_C values for large JS and it almost vanishes for $JS \approx 2W$, but the MC values decrease more slowly and kind of saturate at large JS values. It is to be noted that the MC calculations were performed on system sizes with $N=5^3$ and $N=6^3$ sites, and the average over disorder was done over seven configurations only. For $x=0.065$, the systems with $N=5^3$ and 6^3 sites contain only 8 and 14 magnetic impurities respectively. On the other hand, the self-consistent calculations were performed on a system size $N=16^3$ and the disorder average was done over few hundred configurations of disorder.

Now the huge difference observed between the SC-LRPA and the full MC results was attributed to mainly two reasons : (i) strong finite size effects, and (ii) an insufficient averaging over too few disorder configurations. Figure 2.10 shows the average Curie temperatures for various system sizes calculated within the SC-LRPA. A systematic average was done over a few thousand disorder configurations for the smallest systems and a few hundred for the largest systems. We immediately observe that the Curie temperatures are strongly size dependent. For $JS=0.7\ W$, the T_C for $L=5$ is more than five times larger than the one for $L=20$. This shows the large impact of the finite size effects in the case of diluted systems. Now to stress the importance of sampling over disorder, Figure 2.11 shows the distribution of the Curie temperatures obtained from different system sizes. As can be seen from the figure, for the smallest system size ($L=4$) a wide distribution of the critical temperatures is obtained, which can vary by at least one order of magnitude. Thus it is easy to realize that averaging over a small number of configurations (about 10) would lead to an overestimation of the critical temperature by a factor of about 10-20 compared to that obtained by averaging over a few thousand configurations. We also observe that with the increase in the system size the width of the T_C distributions decreases sharply, and almost tends to zero in the thermodynamic limit, which is the case for $L \geq 16$. It was concluded that in order to obtain reliable estimates the size of the systems considered, L, should be at least five to six times larger than the typical distance between the impurities. This also showed that averaging over only a few configurations of disorder for small systems is definitely insufficient to provide a reliable value of the Curie temperatures. The other essential aspect

of the MC calculations[67] is the determination of the Curie temperatures. In Ref.[67] T_C was extracted from an inaccurate approximative criteria on the magnetization curves, which is apparently not very accurate. As discussed previously, extraction of the critical temperature is such an approximate manner could incur serious errors due to the finite size effects as well as insufficient statistical sampling. On the other hand, within the self-consistent theory the critical temperature is directly obtained by using a semi-analytical formula and hence the possible errors due to any kind of extraction do not arise.
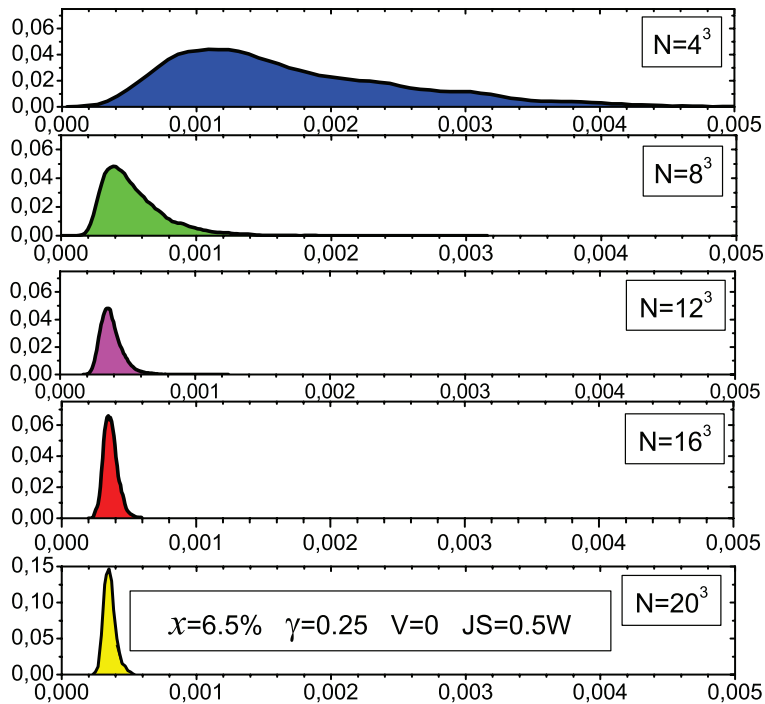
Figure 2.11: Distribution of the Curie temperatures (the x-axis is T_C in units of W) for different system sizes $N=L^3$, where L varies from 4 to 20. The parameters are given in the figure. (From Ref.[66]).

In another study based on MC calculations[68], the authors applied the dilute Kondo model to the case of Mn doped GaAs on a fcc lattice, including a realistic band structure and spin-orbit coupling. The Curie temperatures were calculated as a function of the local coupling J, for a fixed concentra-

tion of magnetic impurities x=0.085 and a hole density p_h≈0.75. However, the calculations were performed assuming for the local couplings JS=1.2 eV, which is about three times smaller compared to the realistic value of 3 eV. (Since the widely accepted value for the local p-d coupling is J≈1.2 eV, and the spin of Mn^{2+} is S=5/2). Assuming this correct value for the coupling the calculations would lead to $T_C \approx 700$ K, which is about five times larger than those experimentally observed. Thus this model was considered as inappropriate for $Ga_{1-x}Mn_xAs$. (For more details one can refer to the comment[69]). Also the value of J considered in Ref.[68] corresponds to the weak coupling regime (perturbative limit), where the Mn-Mn couplings may develop an RKKY-like tail. This leads to a strong suppression of T_C or finally to no ferromagnetic phase in the thermodynamic limit. These MC calculations were also found to have similar drawbacks as those discussed previously. The systems considered contained typically 20 localized spins and the average was done over five configurations of disorder only. Due to the small size of the systems considered in the MC simulations, the effects of the RKKY tail are suppressed which leads to finite and large values of the Curie temperatures.

Thus we see that the in principle exact MC simulations suffer from serious numerical shortcomings when it comes to the study of diluted magnetic systems. Unlike the case of non-dilute systems, the finite size effects and proper statistical sampling play a crucial role in diluted systems. Within the MC calculations, the system sizes considered are often relatively small due to the requirement for considerable computational resources, averaging over only a few disorder configurations leads to an insufficient sampling and the Curie temperatures are determined from approximative procedures. The combined effect of these may lead to strong overestimations of the critical temperatures. Moreover the MC simulations are not able to reproduce properly the limiting regimes of strong and weak couplings. However, within some large-scale MC simulations it is possible to study relatively large systems. These include the hybrid Monte Carlo (HMC) method[70], the polynomial expansion Monte Carlo (PEMC) method[71], and the truncated polynomial expansion Monte Carlo (TPEMC) method[64]. The self-consistent treatment, on the other hand, allows the study of much larger system sizes and is relatively

fast. The computational requirements are much less in comparison to the MC calculations. The Curie temperature is provided by a semi-analytical formula, which is also found to be in good agreement with the experimentally measured values. Hence to conclude we have demonstrated here the reliability and the accuracy of the SC-LRPA method by direct comparison with the MC simulations in the case of diluted magnetic systems.

2.4 Magnetic excitation spectrum of the nearest-neighbor diluted Heisenberg model

The SC-LRPA is already known to be efficient to determine the critical temperatures in disordered and diluted systems. Here we show the efficiency and the accuracy of this approach to determine the magnetic excitation spectrum. To demonstrate this we have studied the spin excitations in the three-dimensional (3D) diluted Heisenberg model with nearest-neighbor ferromagnetic interactions[72]. Until now most of the theoretical studies within the classical MC methods focus on the equilibrium properties of the Ising model[73, 74], and there are very few dealing with the 3D site diluted Heisenberg model[75]. However, probably due to the heavy requirements of both memory as well as CPU time, the spin excitation spectrum of the 3D diluted Heisenberg model has so far not been studied. In this section we are going to present a detailed study of the magnetic excitation spectrum in this model, where the disorder effects arising from dilution are treated accurately within the SC-LRPA approach. We are going to provide a detailed analysis of the magnon density of states and the magnon spectrum as a function of the dilution. In addition, we also estimate the spin-stiffness which is found to vanish at the percolation threshold exactly.

To start with we introduce the diluted Heisenberg Hamiltonian which describes N_{imp} interacting quantum/classical spins randomly distributed on

a lattice of N sites, given by

$$H_{Heis} = -\sum_{i,j} J_{ij} p_i p_j \mathbf{S}_i \cdot \mathbf{S}_j \qquad (2.15)$$

The sum ij runs over all sites and the random variable p_i is 1 if the site is occupied by a spin otherwise it is 0. Here all the calculations are performed at T=0 K, the quantum/classical nature of the spins is irrelevant. Hence we have assumed classical spins with $|\mathbf{S}_i|$=1. Here the couplings J_{ij} are are restricted to nearest neighbor only (J). Note that the exchange couplings can be very general in nature (short or long ranged) in realistic systems and can be provided by first-principle based calculations or model studies, as we shall discuss later. Now within the SC-LRPA, the retarded Green's functions are introduced to describe the transverse spin fluctuations (Equation 2.12). The higher order Green's functions in the equation of motion are decoupled using the Tyablicov decoupling scheme[54] (random phase approximation). The effective Hamiltonian matrix elements are now given by $(\mathbf{H}^c_{eff})_{ij} = -\langle S^z_i \rangle J_{ij} + \delta_{ij} \sum_l \langle S^z_l \rangle J_{lj}$ and $(\mathbf{D})_{ij}=2\langle S^z_i \rangle \delta_{ij}$, where "$c$" denotes the configuration of disorder (for details see Appendix B). $\langle S^z_i \rangle$ is the local magnetization which has to be calculated self-consistently at each temperature and for a given configuration of disorder. This is evaluated from a Callen-like expression[63]

$$\langle S^z_i \rangle = \frac{(S - \Phi_i)(1 + \Phi_i)^{2S+1} + (1 + S + \Phi_i)\Phi_i^{2S+1}}{(1 + \Phi_i)^{2S+1} - \Phi_i^{2S+1}} \qquad (2.16)$$

where Φ_i is the local effective magnon occupation number given by

$$\Phi_i = -\frac{1}{2\pi \langle S^z_i \rangle} \int_{-\infty}^{+\infty} \frac{\Im G_{ii}(\omega)}{exp(\beta \omega) - 1} d\omega \qquad (2.17)$$

Now the matrix $\mathbf{H}^c_{eff}$ is non-Hermitian (real and non-symmetric) but it has the property of bi-orthogonality[76]. Hence we have to define the the right and left eigenvectors of $\mathbf{H}^c_{eff}$ denoted by $|\Psi^{R,c}_\alpha\rangle$ and $|\Psi^{L,c}_\alpha\rangle$ respectively, both associated with the same eigenvalue ω^c_α. The retarded Green's functions can

now be expressed in terms of the right and left eigenvectors as

$$G_{ij}^c(\omega) = \sum_\alpha \frac{2\langle S_j^z \rangle}{\omega - \omega_\alpha^c + i\epsilon} \langle i|\Psi_\alpha^{R,c}\rangle\langle\Psi_\alpha^{L,c}|j\rangle \quad (2.18)$$

Despite the matrix being non-Hermitian, the spectrum is real and positive at each temperature in the ferromagnetic phase. A negative eigenvalue would indicate an instability of the ferromagnetic phase, as would be the case in the presence of frustration. However, since the exchange couplings we use here are all ferromagnetic, there is no possible frustration and the system exhibits long-range ferromagnetic order beyond the percolation threshold. Now since we are interested in the excitation spectrum at $T{=}0$ K, the matrix $\mathbf{H}_{eff}^c$ is real symmetric and hence the right and left eigenvectors are identical. Thus Equation 2.18 becomes

$$G_{ij}^c(\omega) = \sum_\alpha \frac{2\langle S_j^z \rangle}{\omega - \omega_\alpha^c + i\epsilon} \langle i|\Psi_\alpha^c\rangle\langle\Psi_\alpha^c|j\rangle \quad (2.19)$$

However, it is important to note that within the SC-LRPA one can also calculate the spin excitation spectrum as a function of the temperature, and analyze the evolution of the spin dynamics with increase in temperature.

In the following we calculate the magnon density of states, the dynamical spectral function, the spin-stiffness as well as the Curie temperature as a function of the concentration of localized spins $x{=}\frac{N_{imp}}{N}$. The localized spins are randomly distributed over a simple cubic lattice and periodic boundary conditions have been implemented.

2.4.1 Dilution effects on the average magnon density of states

Magnons are associated with the elementary excitations of a spin system which have a wave-like form. These spin waves are low lying oscillations in the relative orientations of the spins on a lattice. Magnons are essentially quantized spin waves. Here we are interested in the magnon density of sates

(DOS) which is given by

$$\rho(\omega) = \frac{1}{N_{imp}} \sum_i \rho_i(\omega) \qquad (2.20)$$

where $\rho_i(\omega)$ is the local magnon DOS given by

$$\rho_i(\omega) = -\frac{1}{2\pi \langle S_i^z \rangle} \Im G_{ii}(\omega) \qquad (2.21)$$
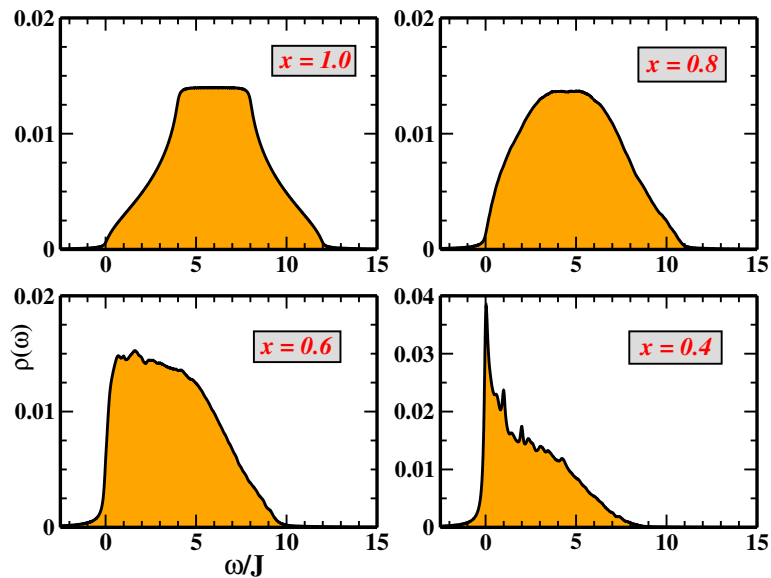
Figure 2.12: Magnon density of states $\rho(\omega)$ as a function of the energy ω for four different x. The energy axis (x-axis) is in units of ω/J. (From Ref.[72]).

Figure 2.12 shows the magnon (DOS) as a function of the energy, for four different concentrations of localized spins. Here $x=1.0$ corresponds to the clean case (no dilution). With increasing dilution we observe a significant change in the shape of the magnon DOS as well as a reduction of the bandwidth. We also notice an increase in the weight of the low-energy DOS for higher dilutions. As we approach the percolation threshold which is located at $x_c=0.31$[40], we observe that for the lowest concentration, $x=0.4$, a sharp

peak develops at $\omega=0$. This feature is attributed to the formation of several isolated clusters which have their own zero energy modes. Additional peak structures are found to be located at $\omega=J$ and $2J$ respectively for higher energies. These peaks are due to the non-zero eigenmodes of these isolated clusters. However, this average DOS does not provide any information on the nature (extended/localized) of the magnon modes. This would require a more careful analysis and study. One could determine this either by the calculation of the inverse participation ratio (IPR) or evaluation of the typical magnon DOS[77] which provide a direct access to the "mobility edge" separating the localized magnon modes from the extended ones. The IPR is defined as

$$\mathbf{IPR}(n) = \left(\sum_{\mathbf{r}} \mid \psi_n(\mathbf{r}) \mid^4 \right)^{-1} \tag{2.22}$$

where $\psi_n(\mathbf{r})$ are the normalized eigenfunctions. The IPR is directly proportional to the volume of the system for extended states but is independent of the system size for localized states. The typical magnon DOS is given by

$$\rho_{typ}(\omega) = exp(\langle ln\rho_i(\omega)\rangle_c) \tag{2.23}$$

where the notation $\langle ... \rangle_c$ represents the average over disorder configurations and $\rho_i(\omega)$ is the local magnon DOS. The mobility edge is expected to vanish at the percolation threshold exactly.

2.4.2   Dynamical Spectral Function

The dynamical spectral function, also known as the dynamical structure factor, provides direct insight into magnetic excitation spectrum of the system. This can be accessed most directly by inelastic neutron scattering experiments. The averaged spectral function is given by

$$\bar{A}(\mathbf{q},\omega) = -\frac{1}{\pi\langle\langle S^z\rangle\rangle}\Im\bar{G}(\mathbf{q},\omega) \tag{2.24}$$

where $\bar{G}(\mathbf{q}, \omega)$ is the averaged Fourier transform of the retarded Green's functions

$$\bar{G}(\mathbf{q}, \omega) = \left\langle \frac{1}{N_{imp}} \sum_{ij} e^{i\mathbf{q}(r_i - r_j)} G_{ij}^c(\omega) \right\rangle_c \qquad (2.25)$$

and

$$\langle\langle S^z \rangle\rangle = \frac{1}{N_{imp}} \sum_i \langle S_i^z \rangle \qquad (2.26)$$

is the total magnetization averaged over all spin sites.
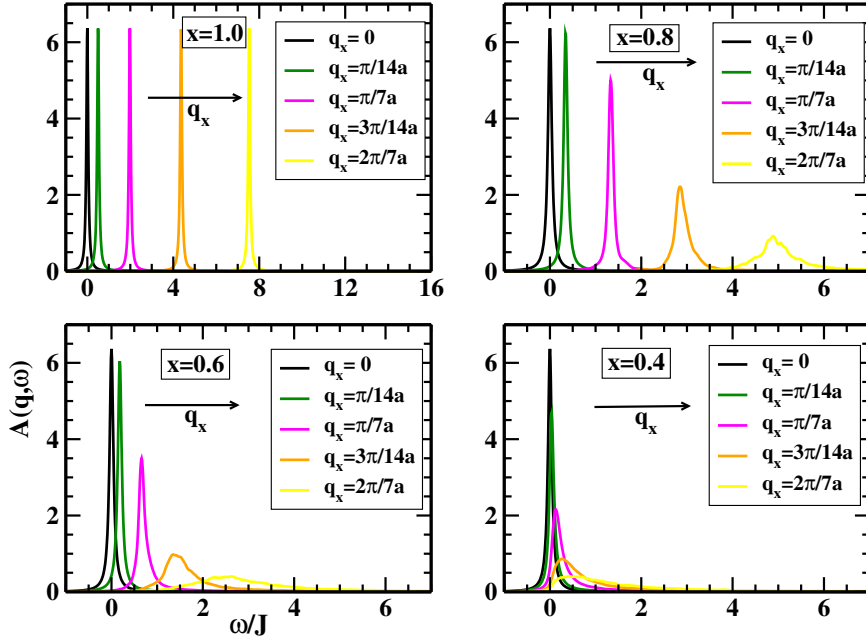
Figure 2.13: Spectral function $A(\mathbf{q}, \omega)$ as a function of the energy ω in the (1 0 0) direction for different values of q_x, and for four different x. (Here L=28). (From Ref.[72]).

In Figure 2.13 we have plotted the spectral function $\bar{A}(\mathbf{q}, \omega)$ as a function of energy for different values of the momentum $\mathbf{q}$ in the (1 0 0) direction. The
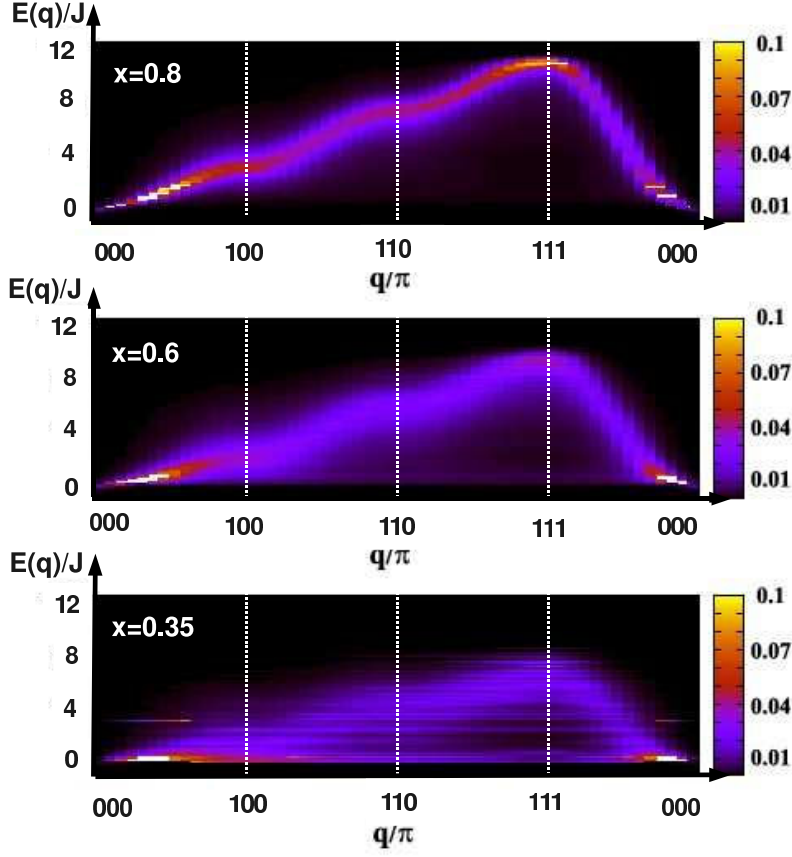
Figure 2.14: Spectral function $\bar{A}(\mathbf{q}, \omega)$ in the $(\mathbf{q}, \omega)$ plane for three different values of x. (Here $L=32$). (From Ref.[72]).

spectral functions shown here correspond to four different concentrations of localized spins x, where $x=1.0$ denotes the clean case. The size of the simple cubic lattice considered here is $L=28$ and periodic boundary conditions have been implemented. Note that for $x=0.8$, the system contains approximately 18000 spins, which can be considered as quite large. We have performed similar calculations for system sizes $L=20$ and $L=24$ to analyze the finite-size effects. It was concluded that $L=28$ is sufficiently large for the following discussions. A systematic average was done over 50 configurations of disorder. However, on checking for the necessary number of random configurations it

was found that 20 configurations are sufficient for the L=28 system. An insufficient sampling over disorder can lead to an error in the estimation of the spin-stiffness, which we shall see later. Now as we can clearly see from the figure that well defined excitations exist only for small values of the momentum **q**, except for the clean case where we observe sharp peaks for all values of the momentum. As the momentum increases the peak becomes broader and develops a tail extending towards higher energies, with increase in dilution. On approaching the percolation threshold, for sufficiently low concentration of spins, the magnetic excitation peaks become strongly asymmetric. Similar asymmetric peaks were also observed in the magnetic excitation spectrum for the diluted antiferromagnet $Mn_xZn_{1-x}F_2$ [78]. This increase in asymmetry with the momentum corresponds to a crossover from propagating spin waves to localized excitations (fractons)[79, 80].

In Figure 2.14, we show the spectral function in the $(\mathbf{q}, \omega)$ plane, corresponding to three different concentrations of localized spins, x=0.8, 0.6, and 0.35 respectively. The spectral function is plotted over the entire Brillouin zone. In contrast to the case of non-dilute systems, well defined excitations are found to exist in the dilute case only in a restricted region of the Brillouin zone close to the Γ point [**q**=(0 0 0)]. From the figure we conclude that well defined excitations cease to exist as we go to higher dilutions. Also the broadening of the excitation spectrum increases significantly as we move away from the Γ point. As we get closer to percolation threshold, this broadening can be attributed to the formation of localized modes. We believe that the momentum cut-off below which well defined excitations exist should be related to the percolation correlation length. A somewhat similar kind of behavior was observed in the excitation spectrum of the diluted magnetic semiconductor $Ga_{1-x}Mn_xAs$[81]. However the exchange couplings in that case were obtained from *ab initio* based studies, and the couplings were rather extended and dependent on the concentration of localized spins. We shall discuss this in more detail in the following chapter.

2.4.3   Spin-stiffness and percolation threshold

As already stated the SC-LRPA is consistent with the Goldstone theorem. Now as we know according to the Goldstone theorem, the spontaneous breaking of any continuous symmetry is associated with the appearance of low energy excitations, known as the Goldstone modes. In the case of the Heisenberg Hamiltonian, this spontaneous symmetry breaking is related to the rotation invariance of the spins. The low lying excitations which arise as a result of this are better known as magnons. Now in the case of ferromagnetic systems, the magnon excitation energy in the long wavelength limit ($q \rightarrow 0$) is quadratic in q,

$$\omega(q) \sim Dq^2 \tag{2.27}$$

The coefficient D is known as the spin-stiffness and it can be obtained by inelastic neutron scattering experiments or by ferromagnetic resonance measurements. Inelastic neutron scattering experiments are able to measure the magnon dispersion curves, from which the spin-stiffness coefficient can be extracted. Note that for the antiferromagnetic case the magnon dispersion relation is linear in q. The spin-stiffness constant is of general importance in a wide class of systems. For example, it is used to identify the quantum phase transitions in systems with metal-insulator transitions. In the present case, we are interested in estimating the spin-stiffness for the nearest neighbor Heisenberg model and study its variation with respect to the concentration of localized spins.

To begin with we plot the magnon energy $\omega(q)$ for different concentrations of localized spins as a function of q^2, as shown in Figure 2.15. In fact what we actually plot is the energy of the first peak in $A(\mathbf{q}, \omega)$ in the (1 0 0) [$\mathbf{q}=(\frac{2\pi}{La_0}$ 0 0)] direction as a function of q^2. The system size varies from L=20 to L=32. As can be seen from the figure for small momentum ($q \rightarrow 0$), $\omega(q) \approx D(x)q^2$. Hence from the slope of these curves we can extract the spin stiffness $D(x)$ for different x. We observe a strong decrease of the slope as we approach the percolation threshold. Note that, the perfect linear behavior of $\omega(q)$ as a function of q^2 vindicates the fact that the average over disorder
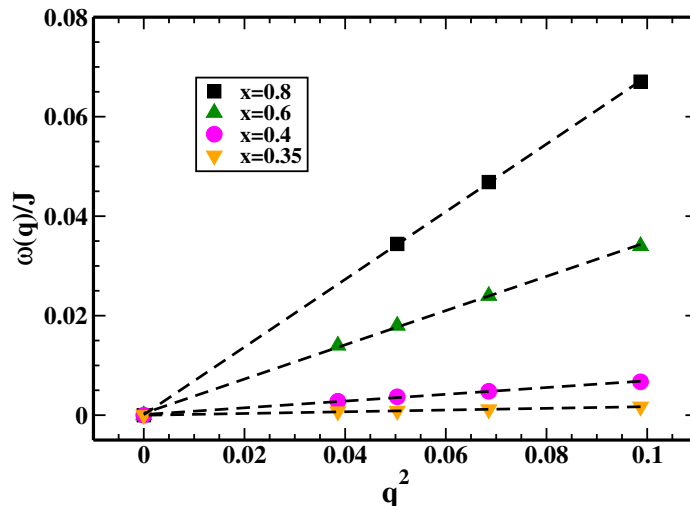
Figure 2.15: Magnon energy $\omega(q)$ as a function of q^2 for different values of x. Here L=20, 24, 28, and 32. (From Ref.[72]).

configurations was obviously sufficient. An insufficient averaging would lead to some kind of fluctuations in the dispersion curves. In Figure 2.16 we have plotted the spin stiffness $D(x)$ as a function of the concentration of the localized spins x. We find that the spin stiffness is almost linear from $x = 1.0$ down to $x = 0.5$ and only forms a concave toe close to the percolation (denoted by x_c in the figure). We have also shown the spin stiffness obtained by Kirkpatrick [40]. The author had used site percolation statistics on random resistor networks, as a natural generalization of lattice models, and obtained a relation between the site percolation probability $P^{(s)}(x)$, the conductance $G(x)$ and the spin stiffness coefficient $D(x)$. We find that our results are in very good agreement with those of Ref.[40]. The important thing to note here is that the method we have used is entirely different from that adopted in Ref.[40], since we extract the spin-stiffness directly from the curvature of the magnon excitations. We have also plotted the MF-VCA value which is given by $D^{MF-VCA}(x)=xD(x = 1)$. For a decreasing concentration of localized spins the difference between the MF-VCA and the SC-LRPA value increases
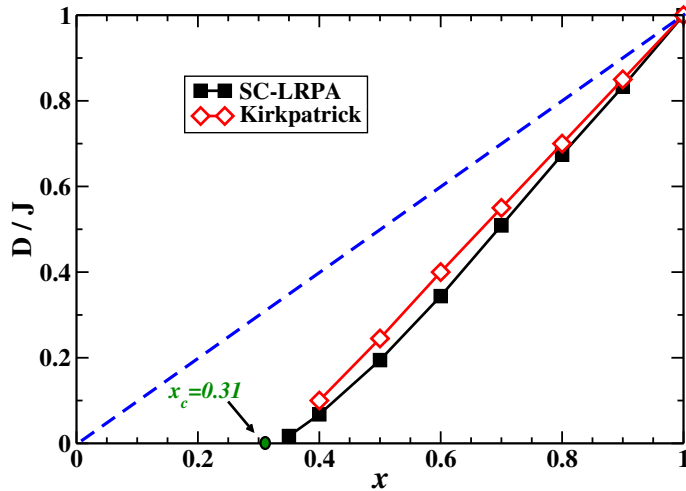
Figure 2.16: Spin-stiffness D as a function x. The squares correspond to the SC-LRPA values, and the diamonds represent the data from Ref.[40]. The dashed line denotes the VCA values. (From Ref.[72]).

significantly. Below x=0.5, the $D^{MF-VCA}(x)$ drastically overestimates the values obtained within the SC-LRPA. The percolation effects are clearly not reproduced. Thus the failure of the MF-VCA treatment to handle disorder effects in the diluted magnetic systems is established once again.

Note that the spin stiffness curve shown here is very different from what was obtained in the case of optimally annealed samples of the diluted magnetic semiconductor $Ga_{1-x}Mn_x As$ [81]. This difference of behavior is due to the fact that in the case of $Ga_{1-x}Mn_x As$ the concentrations were much smaller and that the couplings were rather extended and spin concentration dependent. We will come back to this later in this manuscript.

2.4.4   Curie temperature as a function of localized spins

After analyzing the magnon excitation spectrum and extracting the spin-stiffness we now discuss the critical temperatures of the nearest neighbor diluted Heisenberg model. Figure 2.17 shows the Curie temperature plotted

60
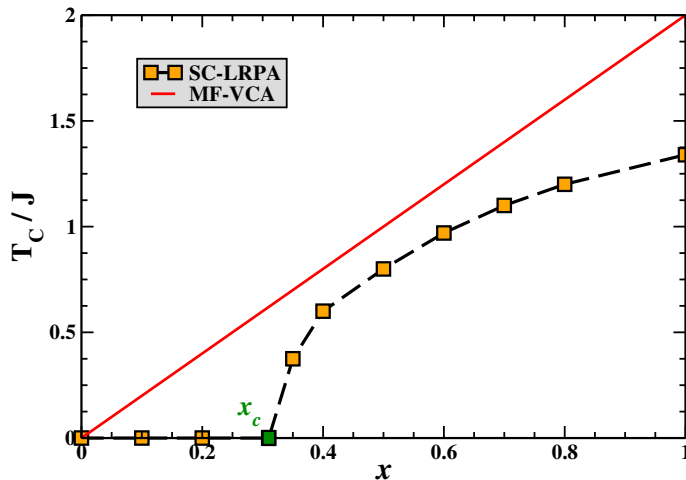
Figure 2.17: Curie temperature as a function of x. The solid (red) line is the MF-VCA T_C value. (x_c denotes the percolation threshold). (From Ref.[82]).

as a function of the concentration of localized spins. The symbols in the figure correspond to the T_Cs calculated within the self-consistent approach. The system size considered here is $L=32$ and a systematic average over a few hundred configurations of disorder was performed. Here again we notice that the Curie temperature corresponding to the clean case ($x=1$) reduces to that of the standard RPA value ($1.32J$) for the nearest neighbor simple cubic lattice. For increasing dilution we observe a non-linear decrease in the critical temperatures. This decrease is rather fast as we approach the percolation threshold (denoted by x_c in the figure) from above. The Curie temperature appears to vanish at the percolation threshold exactly, below which there is no ferromagnetic order. This once again proves the reliability and the accuracy of the SC-LRPA to treat dilution and/or disorder effects. For the sake of comparison we have also shown the Curie temperatures calculated within the MF-VCA, denoted by the solid line in the figure. As can be clearly seen, the MF-VCA always overestimates the critical temperatures for all finite dilutions. The disorder effects are evidently not taken into

consideration within the MF-VCA treatment, as it predicts a finite critical temperature even below the percolation threshold. The actual nature of the exchange couplings are not accounted for and the concentration of the spins only appear as a prefactor in the calculation of the Curie temperature within the MF-VCA formalism, as was the case seen in the estimation of the spin-stiffness.

2.5 Conclusions

Following the success of the SC-LRPA to determine the Curie temperatures in various disordered and diluted materials, we have tried to demonstrate here its ability to determine the magnetic excitation spectrum. For this we have considered the very general 3D diluted Heisenberg model with nearest neighbor ferromagnetic interactions. The excitation spectrum was almost impossible to study within the existing theoretical approaches, until now. However, within the semi-analytical we are able to provide a detailed and accurate analysis of the magnon excitation spectrum as well as the magnon DOS with respect to the change in dilution. We see that a proper treatment of disorder leads to an unusual behavior of the magnetic excitation spectrum compared to what is usually observed in non-dilute systems. The zone of stability of the well-defined magnon modes is found to shrink drastically as we approach the percolation threshold. The observed broadening in the excitation spectrum close to the percolation threshold is attributed to the formation of localized modes. We have also calculated the spin-stiffness, without any adjusting parameters, and found that our results are in very good agreement with those obtained from an earlier study, based on an entirely different theoretical approach. The calculated spin-stiffness is found to vanish at the percolation threshold exactly, which was not predicted within the MF-VCA approach. Similar to the case of Curie temperatures, the MF-VCA largely overestimates the spin-stiffness. This once again shows the importance of the disorder effects and spin fluctuations, and the need to treat them in a reliable manner. The self-consistent approach proves to be a reliable and accurate tool to determine the spin excitation spectrum in

diluted magnetic systems. The accuracy of the method can be further tested by directly measuring the excitation spectrum by experimental methods, such as inelastic neutron scattering.

Thus we can conclusively say that the SC-LRPA is one of the best available tools to deal with diluted magnetic systems. The efficient and accurate treatment of the disorder and/or dilution effects definitely gives this an edge over other existing methods. In the remaining part of this work, this approach shall be used quite extensively to determine various properties, such as the Curie temperatures, magnetic excitation spectrum, magnon DOS, spin-stiffness, and magnetization, for different kinds of diluted systems.

Chapter 3

Comparison between model and *ab initio* approach: The case of (Ga,Mn)As

3.1 Introduction

In the previous chapter, we have shown a detailed study of the the magnetic excitation spectrum in the diluted nearest-neighbor Heisenberg model[72]. The disordered Heisenberg model is very general and can be used to study any kind of system with a finite concentration of interacting localized spins. Now to describe and analyze the underlying physical principles in realistic diluted materials we need model approaches, which allows one to identify the most relevant physical parameters that control both the magnetic and the transport properties. In this chapter, we shall focus mainly on the well known and widely studied diluted magnetic semiconductors (DMSs), in particular (Ga,Mn)As, in the framework of a minimal model approach and try to identify the crucial parameters which control the ferromagnetism in these materials. The prospect of manipulating the electronic spin for spintronics applications and the possibility of room-temperature ferromagnetism has continued to attract considerable interest in DMSs over the past few years[53, 83]. Now it is well established that the ferromagnetism in these materials is medi-

ated by carriers (mainly holes) coupled antiferromagnetically to the localized spins. The magnetic and transport properties in these materials are found to be sensitive to the dilution effects as well as to the presence of compensating defects. Several theoretical studies, based on model approaches, have been performed to study and predict the properties of DMSs. Among them, one of the most frequently used models found in the literature is based on the realistic six- or eight-band Kohn-Luttinger **k.p** Hamiltonian[84] which includes a p-d exchange interaction between the localized spins and the itinerant carriers. Figure 3.1 shows the calculated Curie temperatures obtained within
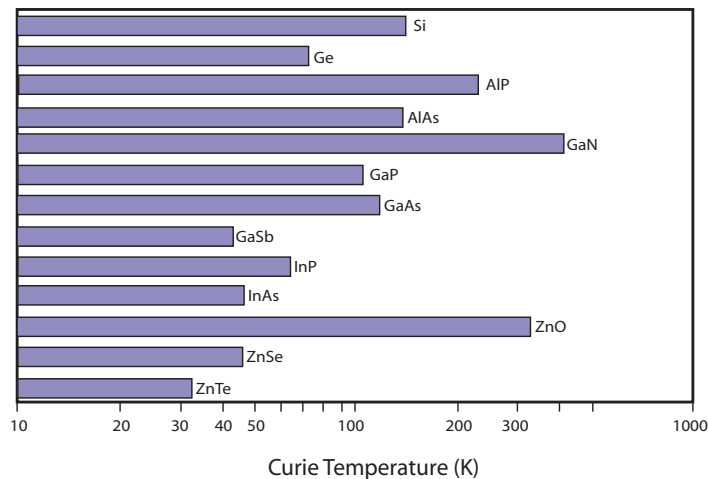
Figure 3.1: Predicted critical temperatures for different DMSs doped with 5% of Mn and containing 3.5 x 10^{20} holes/cm^3. (From Dietl *et al.*[6]).

this model[6]. The authors have predicted above room-temperature ferromagnetism in GaN and ZnO for a nominal concentration of 5% Mn atoms. However, the following approximations were adopted in the treatment of the Hamiltonian, (i) the local coupling (J_{pd}) is treated perturbatively, (ii) the disorder effects are treated within the VCA and effectively neglected, and (iii) the thermal fluctuations are treated within the MFA. These oversimplified approximations can lead to severe consequences such as strong overestimations of the Curie temperatures as well as the ferromagnetic zone of stability.

66

A perturbative treatment of the local coupling, within this approach, leads to RKKY (Ruderman-Kittel-Kasuya-Yosida) interactions for the magnetic couplings. The approach is based on the assumption that the states near the Fermi level have the same character as the host valence band and thus the influence of the impurity perturbation on the host band structure is neglected. However, for realistic DMS systems first principles calculations, in good agreement with experimental studies, suggest otherwise (as we shall see in the following section). Moreover, it was already shown that RKKY exchange interactions are inappropriate to account for the ferromagnetism in DMS systems as it leads to an instability of the ferromagnetic phase[85].

Hence we see that a reliable and robust model study calls for a non-perturbative treatment of the local couplings as well as an appropriate treatment of the disorder effects resulting from dilution. But before we dive into the details of our model approach, let us go first go through a brief overview of some relevant results obtained from *ab initio* based calculations for the case of DMSs.

3.2 An overview of *ab initio* calculations

First-principles calculations, based on DFT[86, 87], is in principle exact and entirely free of phenomenological parameters. DFT based calculations have proved to be an efficient tool to study the origin of magnetism and to predict the electronic and ground state properties of a wide class of diluted materials, and in particular DMSs. The basic idea behind DFT is to study a quantum mechanical many-body problem by using functionals based on the electron density of states (DOS) of the system. For more details on DFT we refer to the review article by Jones and Gunnarrson[88]. As discussed before one of the important aspects to be taken into account in the case of DMSs is the disorder that arises due to the random substitution of the lattice sites by the impurity atoms. Disorder plays a vital role in these materials[37] and hence it is necessary to average over several realizations of the particular system to obtain reliable estimates of the physical quantities. Within the DFT calculations, disorder is treated within the framework of

the coherent potential approximation (CPA)[45, 46]. In addition supercell calculations are used to study the nature of the magnetic interactions and the type of magnetic order[89, 90, 91]. In the following, we shortly discuss some important properties of DMSs obtained within this approach.

3.2.1 Electronic structure of Mn in DMSs

In DMSs several exchange mechanisms, like the double-exchange, the *p-d* exchange, or the superexchange, can play a role in determining the magnetic properties. These exchange mechanisms may depend on several factors, such as the lattice constant, the symmetry of the lattice, the electronic nature and concentration of the magnetic impurities as well as the concentration of any other impurities present in the host. The advantage of the first-principles calculations is that all these complexities of the real materials are taken into account.
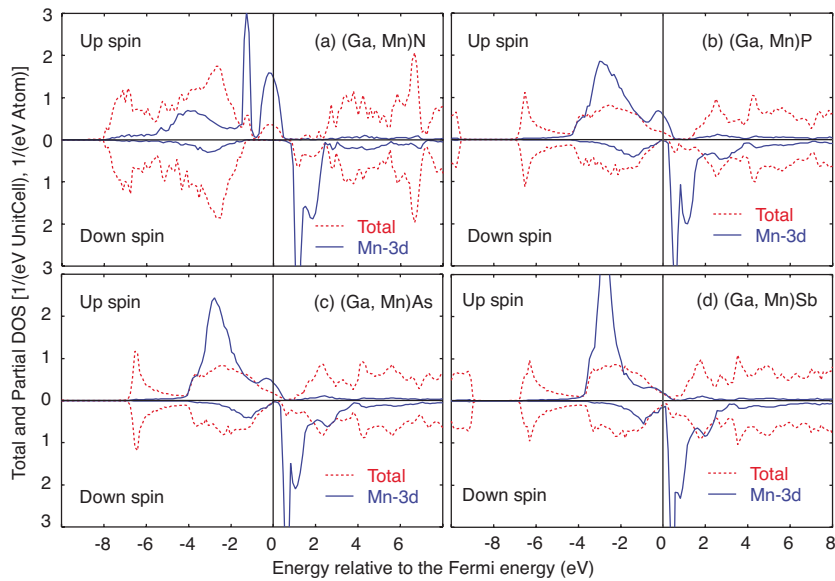
Figure 3.2: Density of states in (a)(Ga,Mn)N, (b)(Ga,Mn)P, (c)(Ga,Mn)As, and (d)(Ga,Mn)Sb. Total DOS (dotted lines) and partial density of 3*d* states (solid lines) at Mn site are shown. (From Ref.[53]).

Now when Mn or any other transition metal impurity is introduced in a semiconductor host at the substitutional site, which has an environment of tetrahedral symmetry, a $3d$ orbital ($3d_{xy}$, $3d_{yz}$, $3d_{zx}$) strongly hybridizes with the host p orbitals leading to the formation of a bonding state (t_b) in the valence band, and an anti-bonding state (t_a) higher up in the band gap. Also a highly localized non-bonding (e) state results from the small p-d hybridization from a doublet $3d$ orbital ($3d_{x^2-y^2}$, $3d_{z^2}$). Figure 3.2 shows the spin-polarized DOS for (Ga,Mn)N, (Ga,Mn)P, (Ga,Mn)As, and (Ga,Mn)Sb each containing 5% of Mn. The solid curves represent the local Mn DOS while the dotted curves give the total DOS. As we can see the local Mn DOS vary quite drastically in different materials, and this depends on the position of the host p level with respect to the Mn d level. In the case of (Ga,Mn)N, the N p level is located within the band gap and it lies below the Mn impurity bands, whereas in (Ga,Mn)Sb the center of the p band of Sb is located above the large peak of the majority d DOS. For (Ga,Mn)P and (Ga,Mn)As, we observe a clear two-peak structure in the majority d DOS of Mn, a weaker resonance at the Fermi level, and a large d peak at lower energies. Note that we observe the presence of a preformed impurity band in the case of (Ga,Mn)N, (Ga,Mn)P, as well as (Ga,Mn)As. The presence of the impurity band plays a significant role in these materials as we shall see in the following.

3.2.2 Non-RKKY nature of the exchange interactions in DMSs

The exchange interactions between the magnetic atoms is one of the most important features in the case of DMSs. A proper determination of the exchange integrals helps us to reliably estimate the critical temperatures, the magnon excitation spectrum, the spin-stiffness, and other important properties. Also the exchange interactions give us an idea of the stability of the magnetic state in these systems.

The exchange couplings for three typical DMSs, (Ga,Mn)As, (Ga,Mn)N, and (Zn,Cr)Te are shown in Figure 3.3. The concentration of impurity atoms
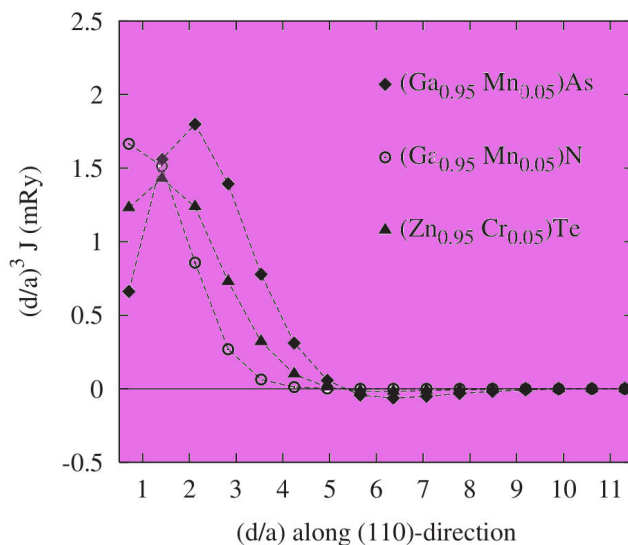
Figure 3.3: Mn-Mn exchange interactions, scaled by a RKKY-like factor $(d/a)^3$, in the (1 0 0) direction for (Ga,Mn)As, (Ga,Mn)N, and (Zn,Cr)Te. (From Ref.[92]).

in each case is 5%. In order to perceive the presence of any RKKY oscillations the couplings are scaled by the factor $(d/a)^3$, where d is the distance between the magnetic impurities and a is the lattice constant. The calculations were performed on a fcc lattice. We immediately observe that the couplings are free from any oscillations and they are ferromagnetic in nature. In (Ga,Mn)As the spatial extent of the interactions is larger as compared to (Ga,Mn)N, where it is relatively short ranged. While in the case of (Zn,Cr)Te, we notice that the couplings are somewhat intermediate. The relatively short-range nature of the interactions in DMSs makes the percolation effects very important in the dilute regime, and this emphasizes the need to treat disorder effects correctly. In the next figure, Figure 3.4, the exchange interactions for (Ga,Mn)As are shown along the dominating (100) direction, for different concentrations of Mn. We observe a decrease in the extent of the couplings with increasing concentration of Mn for relatively large distances. This reduction is due to the increase in the disorder and the half-metallic character of the host semiconductor with increasing concentration of Mn.

70
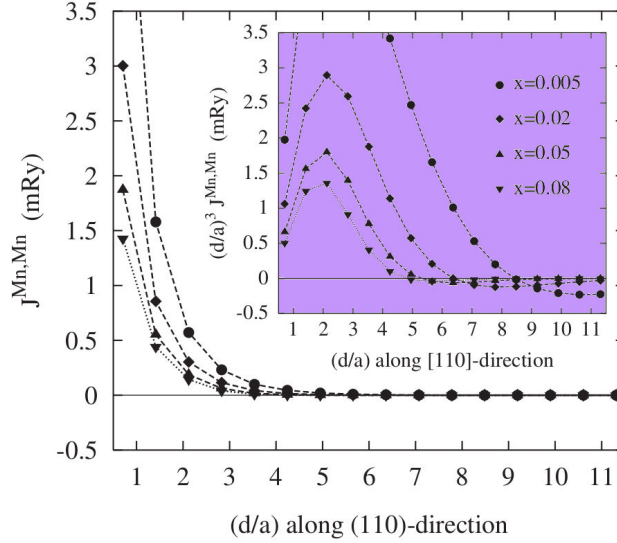
Figure 3.4: Exchange interactions in (Ga,Mn)As, along the (100) direction, for different Mn concentrations, as a function of the distance between the magnetic impurities. Inset: Same interactions scaled by a RKKY-like factor $(d/a)^3$. (From Ref.[92]).

On increasing the impurity concentration we increase the multiple scattering of the carriers on the impurities, which effectively reduces the size of the exchange couplings. The inset in the figure shows the same couplings but scaled by a RKKY-like factor $(d/a)^3$. Here also we notice the absence of any oscillations in the exchange interactions for all Mn concentrations.

Thus we see that the exchange couplings obtained from *ab initio* studies for DMSs are essentially ferromagnetic, relatively short ranged, and almost exponentially decaying. They are also found to depend on the concentration of magnetic impurities. These couplings were used to obtain Curie temperatures accurately, which were found to be in very good agreement with experiments. Here we have primarily discussed the case of III-V DMSs, but an *ab initio* study on the exchange couplings in II-VI semiconductors can be found in Ref.[93]. A more extensive review on the first-principles calculations of DMSs is given by Sato *et al.*[53]. Although in principle exact, the first principles calculations are essentially material specific. Despite the fact that

71

several physical aspects (hybridization, band structure, correlations) are included in this approach, it is difficult to identify their relevant contributions separately. Moreover the *ab initio* calculations are restricted by the size of the supercells on which the calculations are performed. Also, it is almost beyond the reach of *ab initio* techniques to reliably treat the effects of inhomogeneities in DMSs, as we shall see later. This makes the role of a minimal model approach absolutely indispensable.

3.3 A unifying minimal Hamiltonian for DMSs: The V-J model

The ideal tool to identify and analyze the effects of the relevant physical parameters in these diluted systems is a minimal model approach. The one-band V-J model is a prime example of such a model which involves a minimum number of independent parameters, and at the same time can provide a very good qualitative and quantitative understanding of the intriguing physics of these systems. The V-J model differs from the other commonly used impurity-band models[94, 95, 96] in the fact that it takes into account the Coulomb potential V due to the chemical substitution of a cation in the host lattice with a magnetic impurity. The one-band V-J Hamiltonian describing the interaction between the carriers and the localized impurity spins is given by

$$H = -\sum_{ij\sigma}(t_{ij}c_{i\sigma}^\dagger c_{j\sigma} + hc) + \sum_i J_i \mathbf{S_i}.\mathbf{s_i} + \sum_{i\sigma} V_i c_{i\sigma}^\dagger c_{i\sigma}, \qquad (3.1)$$

The hopping term $t_{ij}=t$ for i and j nearest neighbors only, otherwise zero. $c_{i\sigma}^\dagger$ $(c_{i\sigma})$ is the creation (annihilation) operator of a hole of spin σ at site i. J_i is the local p-d coupling between a localized impurity spin $\mathbf{S_i}$ and an itinerant spin carrier $\mathbf{s_i}$ (p- band). In the case of Mn doped III-V materials, $|\mathbf{S}_i|=5/2$. The on-site potential V_i describes the effects of substitutional disorder. $J_i=p_i J_{pd}$ and $V_i=p_i V$, where the random variable $p_i=1$ if the site is occupied by an impurity, otherwise zero. It should be noted that this

minimal one-band model can be used to study the properties of a wide class of disordered magnetic systems, such as manganites as well as the novel d^0 materials. But here we shall restrict ourselves to the case of DMSs only. The calculations are performed on a simple cubic lattice, where x and p denote the impurity concentration and the hole density respectively. In the absence of compensating defects (optimally annealed case) $p=x$. A non-perturbative treatment of the local coupling combined with an exact treatment of the disorder and dilution effects makes this model a reliable tool. This treatment also allows to take into account the localization of the itinerant carriers which can strongly affect the magnetic as well as transport properties, as we shall see later.

3.3.1 The key physical parameter: On-site scattering potential V.

Before going into the detailed calculations, we need to fix the model parameters. The above Hamiltonian (3.1) is characterized by three independent parameters, t, J_{pd}, and V. First the hopping term t is chosen according to the bandwidth W of the GaAs host. In III-V semiconductors the bandwidth is more or less close to that of GaAs ($\sim$7-8 eV). As mentioned earlier since the calculations are performed on a simple cubic lattice, where $W=12t$, the value of t is fixed to 0.7 eV for all (III,Mn)V compounds. In realistic materials, such as (Ga,Mn)As, the underlying lattice structure is fcc. However, in the dilute regime the impurity concentrations and the carrier densities are quite low for the lattice structure to play any significant role. This simplification does not have any drastic effect on the results as we shall see in the following. It should be noted that a variation of about $\pm 10\%$ in t does not affect the results considerably. In both Mn doped II-VI and III-V compounds, the value of J_{pd} is about 1 eV. Now the value of J_{pd} is taken as 1.2 eV, which is the well known value for the local coupling in (Ga,Mn)As[98, 99]. Thus we are left with the last parameter, the on-site potential V, which appears to be the crucial one. This is set in order to reproduce the bound hybridized p-d states energy (E_b) with respect to the top of the valence band, which is
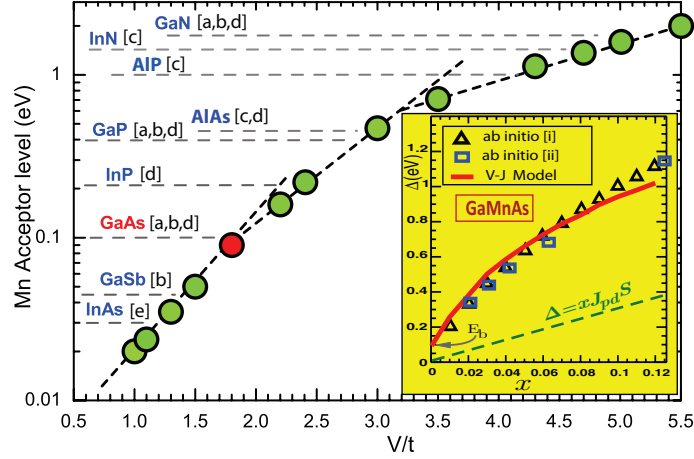
Figure 3.5: Mn acceptor level E_b (eV) as a function of V/t in III-V hosts (assuming $t \approx 0.7$ eV and $J_{pd}S=4.3t$). Inset: Spin splitting Δ as a function x in $Ga_{1-x}Mn_xAs$. (From Ref.[97]).

measured experimentally or obtained from *ab initio* studies. Now this bound state is threefold degenerate (see Fig. 3.6). At a small but finite concentration of Mn, since each Mn^{2+} provides a single hole, it leads to a one-third filled impurity band. Now, for a single Mn impurity in GaAs, the value of E_b is found to be approximately 110 meV[100, 101, 102]. Figure 3.5 shows the calculated Mn acceptor level (E_b) as a function of V/t in different III-V semiconductors. The realistic values of E_b for various hosts were obtained either experimentally or from first-principles calculations. From this the value of V is found to be $1.8t$ for (Ga,Mn)As and $5t$ for (Ga,Mn)N. The inset shows the spin splitting calculated for $Ga_{1-x}Mn_xAs$ as a function of x. It is given by $\Delta(x)=E_{max}^{\uparrow}-E_{max}^{\downarrow}$, where E_{max}^{σ} is the largest eigenvalue in the σ sector. As can be seen, the results obtained within the V-J model are in excellent agreement with those from first principle based LSDA calculations. The MF-VCA value on the other hand (dashed line in the figure), given by $\Delta(x)=xJ_{pd}S$, is found to strongly underestimate the real splitting. Hence the mean-field expression is not a reliable manner to extract the value of J_{pd} in III-V materials. However, this is found to be a good approximation for

(II,Mn)VI materials, which have small $|V|$ values.

3.3.2 Calculation of exchange couplings and comparison with *ab initio* and experimental results

Now in order to calculate the exchange couplings between the magnetic impurities, we assume a fully polarized ground state with all the impurity spins perfectly aligned in one direction, suppose $S_i^z = S$. Within this approximation, the second term on the right hand side of Equation 3.1 acts as an effective on-site potential, and the Hamiltonian can now be written as

$$H^\sigma = -\sum_{ij\sigma}(t_{ij}c_{i\sigma}^\dagger c_{j\sigma} + hc) + \sum_{i\sigma}V_i^\sigma c_{i\sigma}^\dagger c_{i\sigma}, \qquad (3.2)$$

At each site occupied by an impurity, a random on-site spin-dependent potential appears, which is given by

$$V_i^\pm = V \pm \frac{J_{pd}S}{2} \qquad (3.3)$$

Here V_i^+ and V_i^- are the effective potentials acting on the majority and minority spin carriers, respectively. Now this Hamiltonian (Equation 3.2) is diagonalized exactly in both spin sectors ($\sigma = \uparrow, \downarrow$), for a given impurity concentration x and disorder configuration c. The diagonalization provides us with the eigenvalues and eigenvectors denoted by $\{\omega_{\sigma,\alpha}^c, |\Psi_{\sigma,\alpha}^c\rangle\}$, where $\alpha = 1, 2, ..., N$ ($N = L^3$ is the total number of sites on the simple cubic lattice), which in turn can be used to evaluate the couplings as well as the optical conductivity. The magnetic coupling between two localized spins is given by the generalized susceptibility[103]

$$\bar{J}_{ij}(x, \bar{p}) = -\frac{1}{4\pi S^2}\Im\int_{-\infty}^{E_F} Tr(\Sigma_i G_{ij}^\uparrow(\omega)\Sigma_j G_{ji}^\downarrow(\omega))d\omega \qquad (3.4)$$

where the Green's functions are defined as

$$G_{ij}^\sigma(\omega) = \left\langle i\sigma \left| \frac{1}{\omega - \hat{H}^\sigma + i\epsilon} \right| j\sigma \right\rangle \qquad (3.5)$$

and $Tr(\hat{A})=\sum_i\langle i|\hat{A}|i\rangle$. Within this model the local exchange splitting at
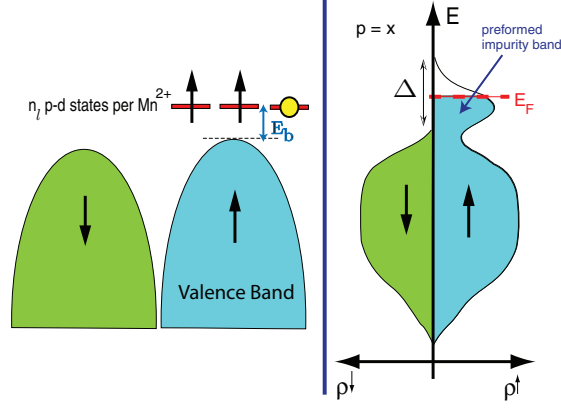
Figure 3.6: Left panel: Schematic representation of the 3 p-d states near the top of the valence band for (III,Mn)V compounds. Right panel: Spin resolved DOS and the formation of an impurity band for a finite Mn concentration (From Ref.[97]).

each site occupied by an impurity reduces to $\Sigma_i=V_i^+ - V_i^-=J_{pd}S$, which is a constant. The couplings are calculated on considerably large system sizes and a systematic averaging is performed over a few hundred configurations of disorder. The finite size effects on the magnetic couplings are also analyzed.

Now in order to facilitate a direct comparison between the model calculations and those obtained from *ab initio* based studies or experimental observations, the following point needs to be considered. As mentioned above, in the realistic case each Mn^{2+} provides $n_l= 3$ degenerate p-d states near the top of the valence band (see left panel of Figure 3.6). These states are known as Dangling Bond Hybrid states[104]. For a small but finite concentration of Mn^{2+}, an impurity band is formed (right panel of Figure 3.6) which merges into the valence band when x is large enough. Since each Mn^{2+} introduces a single hole, the resulting hybridized p-d states impurity band is one-third filled. Now in the one-band V-J model each Mn^{2+} provides a single state. Thus for reasons of consistency the model calculations for optimally annealed

samples ($p=x$) are performed for the hole density $\bar{p}=p/n_l$. Then in both cases the impurity band is one-third filled. Similarly the exchange couplings used to calculate the Curie temperatures and other magnetic properties are given by

$$J_{ij}(x,p) = n_l \bar{J}_{ij}(x, p/n_l) \tag{3.6}$$

and accordingly the optical conductivity is given by

$$\sigma(\omega, p) = n_l \bar{\sigma}(\omega, p/n_l) \tag{3.7}$$

where $\bar{J}_{ij}(x, p/n_l)$ and $\bar{\sigma}(\omega, p/n_l)$ correspond to the values obtained within the one-band model. We will come back to the definition of the optical conductivity in a short while. In what follows next, we shall discuss some of the magnetic and transport properties of DMSs, obtained within this one-band V-J model. We will observe an excellent agreement between the model calculations and those obtained from first-principle based studies as well as experimental results.

3.3.3 Curie temperatures in III-V DMSs: RKKY to Double exchange systems

As an example of the magnetic properties obtained within the one band V-J model, the Curie temperatures for different (III,Mn)V materials as a function of the bound state energy E_b is shown in Figure 3.7[97]. The concentration of Mn is fixed at x=5% and the calculations are performed assuming the case of optimally annealed samples, i.e. $p=x$. A two-step approach was adopted in this case to calculate the T_C's. The exchange couplings were obtained from the V-J model (Equation 3.6) followed by the treatment of the effective diluted Heisenberg Hamiltonian within the SC-LRPA. The T_C's calculated from the *ab initio* exchange integrals are also shown in the figure. We observe a very good agreement between the model calculations and those obtained from *ab initio* based studies. We also observe a clear resonant peak structure in the T_C curve and the calculations predict that (Ga,Mn)As

77
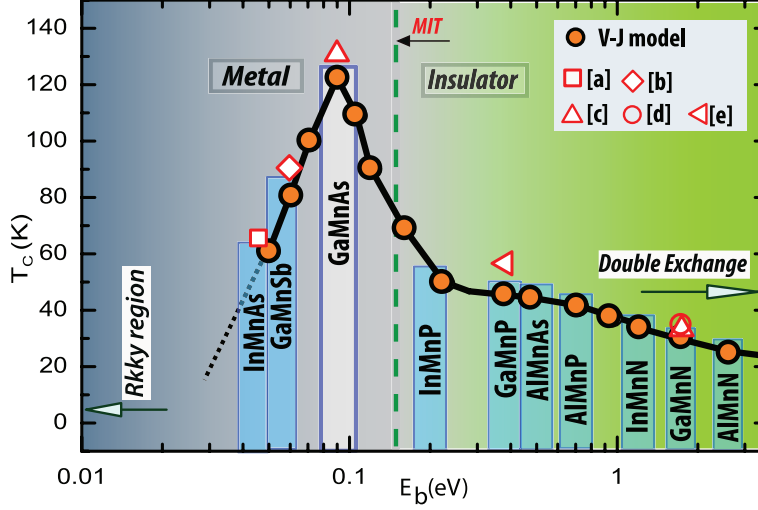
Figure 3.7: T_C as a function of the bound state E_b and for a Mn concentration of 5% in well annealed samples. The filled (open) symbols correspond to the T_C from the V-J model (*ab initio* exchange integrals). (From Ref.[97]).

has the highest critical temperature among the (III,Mn)V compounds. The narrow resonant peak ($30 \leq E_b \leq 200$ meV) is found to be located in the metallic phase but close to the metal-insulator phase transition. This could explain the experimental findings of both metallic and insulating compounds, and the observation of insulator-metal transition after annealing of as-grown samples. Now for small values of E_b (or V), the couplings are RKKY-like and hence the Curie temperatures obtained in this case are quite low. This region corresponds to the case of II-VI materials such as (Zn,Mn)Te or (Cd,Mn)Te, in which the critical temperatures are relatively small. With increasing E_b the critical temperatures are found to increase. This is due to the suppression of the RKKY oscillations and the couplings become relatively short ranged, as a result of the resonant states due to the preformed impurity band. Further increase in E_b leads to a strong reduction in the range of the couplings, the relevant couplings controlling the critical temperatures become smaller and hence the T_C values also reduce significantly. For very large values of E_b, the interactions become more double-exchange like which leads to very small

values of the Curie temperatures. In this regime the percolation effects play a very important role, which is included in this approach. It is found that (Ga,Mn)P is an insulator, which was also reported experimentally[105]. The T_C's predicted for (Ga,Mn)P (~ 50 K) and (In,Mn)As (~ 60 K) are found to be close to the experimental maximum value, which is ~ 60 K for annealed samples containing 6% of Mn[105, 106, 107, 108].

Thus we see that the Curie temperatures calculated within the one-band V-J model are found to be in very good agreement with first-principles based studies and experimental observations alike. It should be noted that the calculations do not involve any adjustable parameters. Also the resonant structure of the critical temperatures, with varying the bound state E_b (or effectively the local potential V), shows that (Ga,Mn)As is close to optimality among the (III,Mn)V compounds. (Ga,Mn)As is found to exhibit the highest Curie temperature, however it is still far below the room-temperature.

3.3.4   Comparsion between theory and experiment for the Optical conductivity

In this part we are going to study the feasibility of the V-J model to determine the transport properties in DMSs. In order to study this, the optical conductivity was calculated as a function of the frequency ω for the well annealed cases of (In,Mn)As, (Ga,Mn)As, and (Ga,Mn)P, at a fixed Mn concentration of 5%[97]. This is shown in Figure 3.8. As discussed shortly before, the optical conductivity is given by $\sigma(\omega, p) = n_l \sum_\sigma \bar{\sigma}_\sigma(\omega, p/n_l)$, where the subscript σ denotes the spin index. The regular part of the optical conductivity is given within the Kubo formalism, defined as

$$\bar{\sigma}_\sigma(\omega, p/n_l) = \frac{\sigma_0}{N} \sum_{\alpha \neq \beta} (n_\alpha^\sigma - n_\beta^\sigma) A_{\alpha\beta}^\sigma \delta(\hbar\omega - E_\alpha^\sigma + E_\beta^\sigma) \tag{3.8}$$

Here $\sigma_0 = \pi e^2/\hbar a$, where a is the simple cubic lattice parameter, $N = L^3$ is the total number of sites, and n_α^σ is the occupation number of the state $|\Psi_\alpha^\sigma\rangle$

corresponding to the energy E^σ_α. The matrix element $A^\sigma_{\alpha\beta}$ is given by

$$A^\sigma_{\alpha\beta} = \frac{|\langle \Psi^\sigma_\alpha \mid \widehat{j^\sigma_x} \mid \Psi^\sigma_\beta \rangle|^2}{E^\sigma_\beta - E^\sigma_\alpha} \tag{3.9}$$
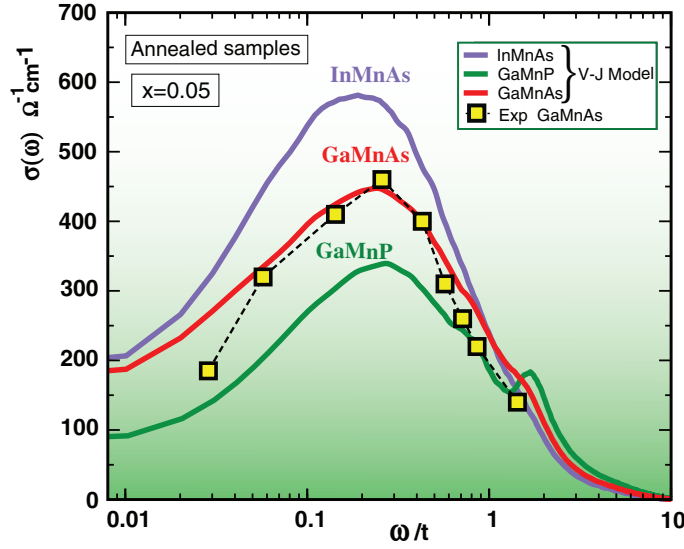
Figure 3.8: Optical conductivity as a function of ω/t for optimally annealed (In,Mn)As, (Ga,Mn)As, and (Ga,Mn)P, for a Mn concentration of 5%. The symbols correspond to experimental data for (Ga,Mn)As. (From Ref.[97]).

where $\widehat{j^\sigma_x}$ is the x component of the current operator in the σ sector ($\sigma = \uparrow, \downarrow$), given by

$$\widehat{j^\sigma_x} = -it \sum_{ij} (c^\dagger_{i,j\sigma} c_{i+\hat{x},j\sigma} - h.c) \tag{3.10}$$

Now coming back to the figure, the symbols represent the experimental data obtained for (Ga,Mn)As[109]. A very good quantitative agreement was obtained with the model calculations over almost the entire frequency range. Moreover the peak position at 0.2 eV in the optical conductivity could be exactly reproduced. For the case of (In,Mn)As, the conductivity is higher than the other two compounds at low frequencies. This is attributed to the

fact that the Fermi level is deeper in the valence band for (In,Mn)As, which means more extended states. The optical conductivity peak is located at 0.11 eV. Now in the case of (Ga,Mn)P, the optical conductivity exhibits a double peak structure. The principal peak is located at $\omega \simeq 0.2$ eV while the secondary one lies around $\omega \simeq 1.2$ eV. For this Mn concentration, in (Ga,Mn)P the impurity band just separates from the valence band. This secondary peak is believed to originate from the electronic transitions between the separated impurity band and the top of the valence band. Detailed experimental studies for the two latter materials would help to further substantiate these predictions.

It is worth mentioning that only recently the one-band V-J model was implemented to study the effects of compensating defects on the transport properties of (Ga,Mn)As and an excellent qualitative and quantitative agreement with experimental results was obtained[110]. The Drude weight (order parameter) is calculated as a function of the hole density and from the metal-insulator phase diagram it is shown that (Ga,Mn)As is indeed close to the metal-insulator transition. The model calculations are shown to reproduce the experimentally observed red-shift of the broad conductivity peak with increasing hole density from compensating to well annealed samples of (Ga,Mn)As. This feature is consistent with the fact that a preformed impurity band exists in the case of (Ga,Mn)As. It is shown that a non-perturbative treatment, beyond the valence band picture, is essential to capture the relevant physical features, which would otherwise lead to an incorrect blue-shift in the conductivity.

81

3.4 Dynamical magnetic properties of (Ga,Mn)As within the V-J model

In this section we are going to study the dynamical magnetic properties of Mn doped GaAs, obtained within the framework of the one-band V-J model. As seen in the previous section, the V-J model could be successfully used to estimate the Curie temperatures and the optical conductivity in a wide range of (III,Mn)V materials. The model calculations were found to be in very good agreement with *ab initio* based studies as well as experimental observations. Now the question is whether this simple model could be effectively implemented to study the nature of the magnetic excitations in these systems, and whether it can reproduce the spin-stiffness values obtained from first principle calculations and those measured experimentally. This was the primary motivation which led us to the current study[111].

Here we focus on the case of (Ga,Mn)As, which has been the most widely studied III-V DMS over the last decade. As already known, the substitution of Ga^{3+} by Mn^{2+} introduces a localized spin (S=5/2) as well as a hole. Disorder and spin fluctuations are found to play a very important role in this material. *Ab initio* based calculations show that Mn strongly affects the nature of the states close to the Fermi level (E_F) leading at low impurity concentrations to a preformed impurity band[90, 112]. Infrared and optical spectroscopy measurements have also shown that the E_F resides indeed in a Mn induced impurity band in (Ga,Mn)As[109]. However, most of the existing model studies[6, 83] are based on a perturbative treatment of Mn in GaAs, which is consistent with the valence band picture. The valence band theory cannot capture the essential features in this case, it is inconsistent with the *ab initio* based studies and it also fails to explain the proximity of (Ga,Mn)As to the metal-insulator transition. This calls for a model approach based on a non-perturbative treatment of the substitution effects as well as a proper account of the disorder and thermal fluctuations. In order to calculate the magnetic properties of (Ga,Mn)As, we follow a two-step approach as discussed previously. This involves, as a first step, the calculation of the exchange interactions between the magnetic impurities

within the V-J model, which is followed by the SC-LRPA treatment of the effective dilute Heisenberg Hamiltonian to calculate the Curie temperatures and other magnetic properties.

3.4.1 Mn-Mn Exchange couplings in (Ga,Mn)As

In Figure 3.9 we have shown the exchange couplings, calculated within the one-band V-J model, for well annealed $Ga_{1-x}Mn_xAs$ for three different Mn concentrations. Note that here we focus on optimally annealed cases, which implies that the concentration of compensating defects (As anti-sites or Mn interstitials) is negligible. We would also like to remind that the systems are homogeneously diluted with no correlations in disorder (absence of in-homogeneities). The model parameters are fixed at t=0.7 eV, J_{pd}=1.2 eV ($J_{pd}S$=3 eV), and V=1.8 t, as discussed in Section 3.3.1. The couplings are calculated for random distribution of magnetic impurities on simple cubic lattices, whose sizes vary between L=16 and L=24. A systematic average
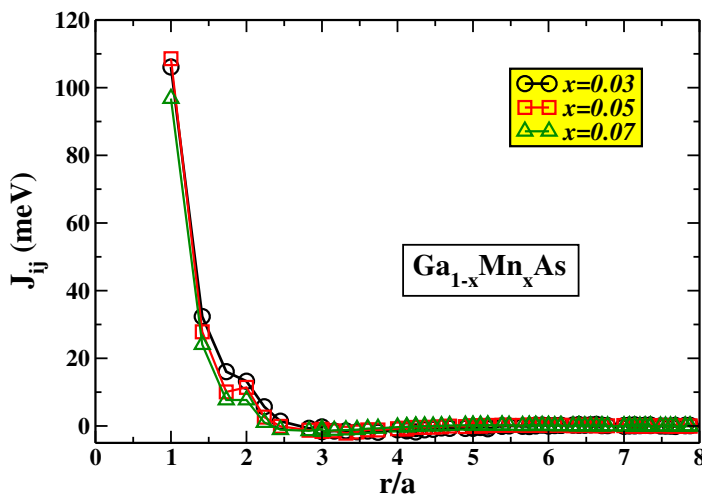
Figure 3.9: Exchange couplings in well annealed $Ga_{1-x}Mn_xAs$ as function of the distance between the impurities, for three different x. (From Ref.[111]).

over a few hundred configurations of disorder is performed and a careful study

of the finite size effects on the magnetic couplings is also made. Since our calculations are performed on a simple cubic lattice (1 atom per unit cell), for the value of the lattice parameter we take $a = \frac{a_0}{4^{1/3}} = 3.55$ Å, where a_0 = 5.65 Å, is the lattice constant in the real zinc-blende GaAs (4 Ga per unit cell). As can be seen from the figure, the couplings obtained for well annealed $Ga_{1-x}Mn_xAs$ are relatively short-ranged and essentially ferromagnetic. They are exponentially damped with increasing distance between the Mn impurities. These are similar in nature to those obtained from first-principles based calculations[92], although not exactly the same. The slight disagreement may be due to the fact that we consider only a single band in our simplified model and also the calculations are performed on simple cubic systems instead of the real fcc lattice, as is done in the *ab initio* based studies. However, as we shall see, these simplifications do not play any major role when it comes to the determination of the Curie temperatures and other magnetic properties. It is also worth noting that calculating the exchange couplings and the corresponding magnetic quantities simultaneously for a given configuration and then averaging these obtained quantities over several configurations leads to the same results as the ones we show here.

3.4.2   Comparsion between *ab initio* and model calculation of the Curie temperature

 Figure 3.10 shows the Curie temperature as a function of the Mn concentration for optimally annealed $Ga_{1-x}Mn_xAs$. To evaluate the T_C, the effective dilute Heisenberg Hamiltonian $H_{Heis}=-\sum_{i,j} p_i p_j J_{i,j}(x,p)\mathbf{S}_i \cdot \mathbf{S}_j$, is treated within the SC-LRPA formalism. The calculations are performed on very large systems (typically $L=50$) together with a systematic average over a few hundred configurations of disorder, for each impurity concentration. We immediately observe that our model calculations are in very good agreement with the T_C's obtained from *ab initio* exchange integrals[57, 113, 114], over the entire range of Mn concentration. These *ab initio* results could in turn reproduce accurately the experimental data[115, 116, 117, 118]. We again stress the fact that our model calculations are free from any adjustable pa-
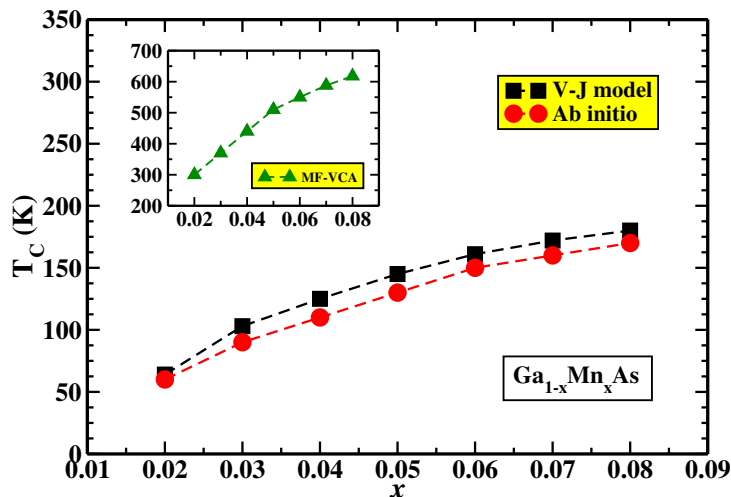
Figure 3.10: Curie temperature as a function of x in well annealed $Ga_{1-x}Mn_xAs$. The squares (circles) represent the V-J model (*ab initio*) calculations. Inset: MF-VCA T_C (in K) as a function of x. (From Ref.[111]).

rameters. These results clearly indicate that the model is able to accurately capture the physics in these dilute materials. For the sake of comparison, we have shown the T_C obtained from the MF-VCA in the inset of figure 3.10. As can be seen, it already leads to room-temperature for only 2% of Mn. Once again this shows the clear overestimations in the critical temperatures and hence the failure of the MF-VCA in treating thermal fluctuations and disorder effects reliably.

3.4.3 Average and typical magnon density of states

Next we study the magnon DOS in (Ga,Mn)As for different concentrations of Mn. Figure 3.11 shows the average and typical magnon DOS as a function of the energy ω. The DOS are calculated in a similar fashion as was discussed in Section 2.4.1. But this time the exchange couplings are obtained from the V-J model, they are rather extended and not restricted to nearest neighbors

85
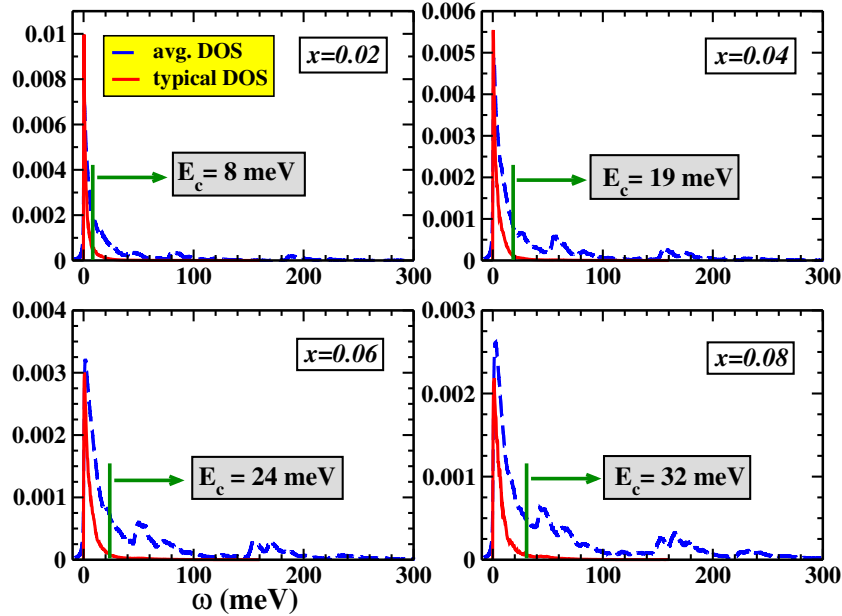
Figure 3.11: Magnon density of states as a function of the energy for four different x. The solid (dashed) lines represent the typical (average) density of states. E_c denotes the magnon mobility edge. (Here $N = 44^3$). (From Ref.[111]).

only. The size of the simple cubic lattice we consider here is $L=44$ and the average over disorder is done for a few hundred configurations. We see that the average DOS ($\rho_{avg}(\omega)$), represented by the dashed line in the figure, exhibits a multi-peak structure, which changes significantly with increasing dilution. For sufficiently high dilution, close to the percolation threshold, we observe a drastic increase in the low energy DOS. This can be attributed to the formation of isolated impurity clusters at low concentrations which have their own zero-energy eigenmodes, which in turn contribute to the average magnon DOS. However, as discussed previously, the average magnon DOS is not able to provide any information on the nature of the magnon states, that is whether they are extended or localized. In order to evaluate this, we have calculated the typical magnon DOS ($\rho_{typ}(\omega)$)[77] in (Ga,Mn)As, shown by the solid (red) line in the figure. The typical magnon DOS, unlike $\rho_{avg}(\omega)$, is a

86

local quantity and it provides direct access to the "mobility edge" separating the localized modes from the extended ones. From the figure we see that there is no significant change in the overall shape of $\rho_{typ}(\omega)$ with varying dilution. But from the $\rho_{typ}(\omega)$ curves we have extracted the energy E_c, which separates the localized states from the extended ones. For each Mn concentration the corresponding values of E_c are indicated in the figure. With increase in the Mn concentration E_c is found to vary from 8 meV for $x = 0.02$ to 32 meV for $x = 0.08$. This not so significant increase in E_c values suggests that even for relatively large concentrations of Mn majority of the magnon excitations in (Ga,Mn)As consist of localized states (fractons)[79, 80].

3.4.4 Magnon spectral function in optimally annealed (Ga,Mn)As

The dynamical spectral function, as we know, provides direct insight into the magnetic excitations spectrum of a system. In Figure 3.12 we show the magnon spectral function $A(\mathbf{q}, \omega)$ (see Equation 2.45) in the $(\mathbf{q}, \omega)$ plane over the entire Brillouin zone corresponding to three different concentrations of Mn in (Ga,Mn)As. The calculations are performed on $L=44$ simple cubic systems and a few hundred configurations are considered for the disorder averaging. However, we found that increasing the number of configurations beyond fifty does not have any significant effect on the results obtained. From the figure, we observe that well defined excitations exist only in a restricted region of the Brillouin zone essentially around the Γ-point [$\mathbf{q}=(000)$]. This is in contrast to what is usually observed in the case of weakly disordered systems, such as manganites. From this we realize that the nature of ferromagnetism in these diluted systems is very different from what is observed in non-dilute materials. A significant broadening in the excitation spectrum is also observed as we move away from the Γ point. This is consistent with our typical DOS calculations shown in Figure 3.11. Now similar results for the excitation spectrum of (Ga,Mn)As were obtained using the couplings from first-principles based tight-binding linear-muffin-tin-orbital approach[81]. In Ref.[81], the excitation spectrum was calculated in a similar
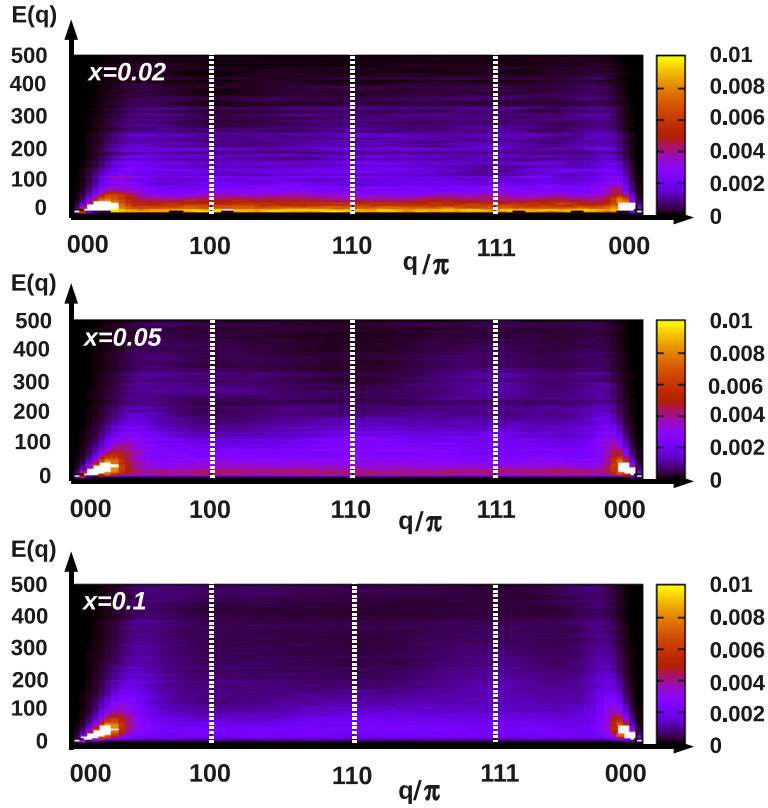
Figure 3.12: Spectral function $A(\mathbf{q}, \omega)$ in the $(\mathbf{q}, \omega)$ plane for three different Mn concentrations (x). The energy axis (y axis) is in meV. (Here $N = 44^3$. (From Ref.[111]).

manner based on the SC-LRPA treatment of the effective dilute Heisenberg Hamiltonian. Hence we find that the magnon spectrum obtained within our one-band model is in very good agreement with that provided by first principles based studies. This also shows that this model can be used in general to study the magnetic spin excitations in a wide class of DMS materials, as it was already shown to be successful in predicting the Curie temperatures in several (III,Mn)V materials[97]. This spectral function is directly accessible by inelastic neutron scattering experiments. Hence detailed experimental studies in this direction would be very useful in confirming our predictions of the excitation spectrum in optimally annealed samples of (Ga,Mn)As.

3.4.5 Calculated and measured Spin-stiffness in Mn doped GaAs

Now we proceed to calculate the spin-stiffness in the case of optimally annealed (Ga,Mn)As within the framework of our one-band V-J model. For this we adopt a similar approach as was used in the case of the nearest-neighbor diluted Heisenberg model (Section 2.4.3), which was shown to be reliable and accurate. As a first step, we have plotted the spin wave energy $\omega(\mathbf{q})$ as a function of $\mathbf{q}^2$ for different concentrations of Mn x, as shown in Figure 3.13. $\omega(\mathbf{q})$ is extracted from the first peak of $A(\mathbf{q},\omega)$ in the (100) di-
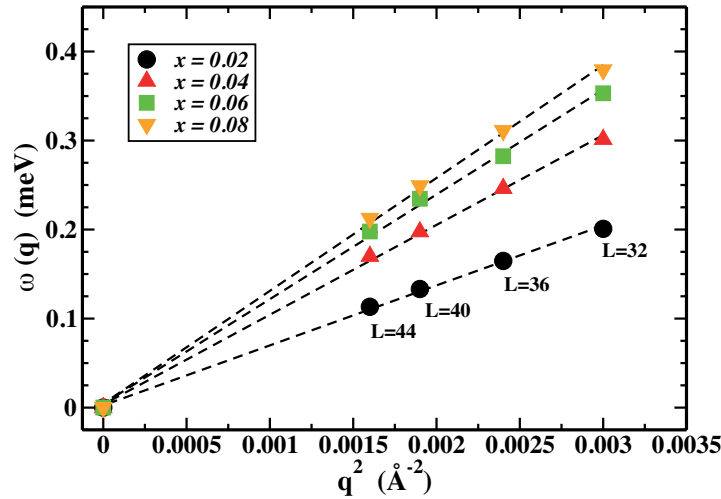
Figure 3.13: Magnon energy $\omega(\mathbf{q})$ as a function of $\mathbf{q}^2$ for different concentrations of Mn (x). ($N=L^3$, where $L=32$, 36, 40, and 44). (From Ref.[111]).

rection. Here the system sizes vary from $L=32$ to $L=44$. The slope of these curves gives the spin stiffness $D(x)$ for different values of x. It is important to note that the perfect quadratic nature of the dispersion curves shown here, corroborates the fact that the average over disorder was sufficient.

Figure 3.14 shows the spin-stiffness D (in meV.Å^2) extracted from the above dispersion curves as a function of the Mn concentration. As mentioned earlier, the lattice parameter for our simple cubic system is $a=\frac{a_0}{4^{1/3}}=3.55$Å, which has also been used to calculate the spin-stiffness here. We would like to remind that using the real zinc blende lattice parameter (a_0) instead would

lead to stiffness values $\sim$2.5 times larger than the ones shown here. Now we found that the spin-stiffness is sensitive to the couplings at comparatively large distances which appear to be strongly finite size dependent. Thus in order to make a correct estimation of $D(x)$, the couplings used are obtained from different system sizes ranging from L=16 to L=24. This leads to the
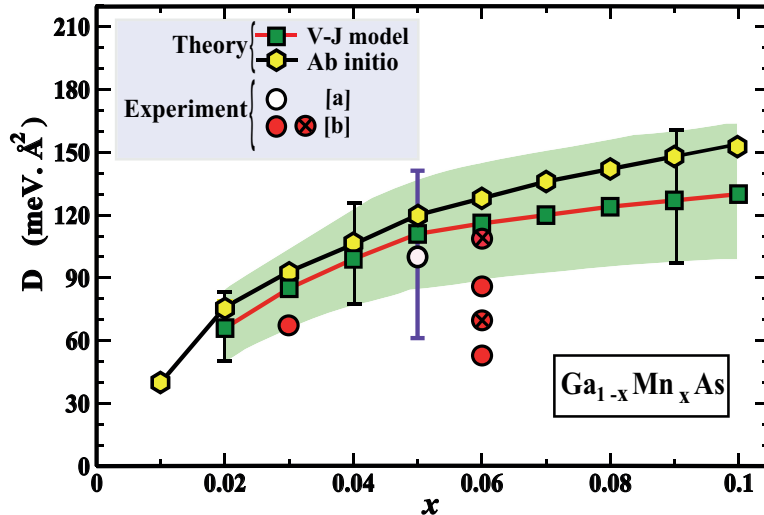
Figure 3.14: Spin-stiffness (in meV.Å^2) as a function of x. Squares correspond to the V-J model, hexagons to *ab initio* values[81] and circles [a,b] to experimental values from Ref.[119, 120]. The green shaded region corresponds to the errors bars for the V-J model (see text for details). (Note the circles with a cross represent the annealed samples from Ref.[120]). (From Ref.[111]).

error bars for $D(x)$ as shown by the shaded region in the figure. On the other hand it should be noted that the exchange couplings obtained from different system sizes do not have a significant effect on the calculated Curie temperatures. In the figure we have shown the $D(x)$ values obtained using the couplings from *ab initio* based studies[81]. The stiffness values shown in Figure 4 of Ref.[81] actually correspond to DS where S=5/2, hence the values we have plotted here have been scaled by a factor of S. We also show available experimental data for well annealed and as-grown samples of (Ga,Mn)As[119, 120]. We find a very good agreement between the stiffness values from our model calculations and those obtained from first principles

based studies, especially for relatively low concentrations of Mn. Thus the V-J model is once again able to successfully reproduce the results obtained within the *ab initio* based studies. Now concerning the experimental results of Sperl *et al.*[120], we find that the agreement for the 6% case corresponds to the well annealed sample of thickness 200 nm. This is consistent with the fact that our couplings are calculated for optimally annealed cases of (Ga,Mn)As. In Ref.[119], the authors reported a value of $D{\approx}100$ meV.Å² measured by ferromagnetic resonance in as-grown samples for x=0.05, which is also in good agreement with our model calculations but then the error bar in this case is about 40% and in all probability this stiffness would increase if the sample is subjected to optimal annealing. The deviation between our results and some experimental data can be explained by the fact that our calculations are performed for the optimally annealed case.

Thus we find an overall very good agreement for the spin-stiffness values obtained from our minimal model approach with those from first-principles based studies as well as experimental results. The model was already shown to be reliable to calculate the critical temperatures and optical conductivity in different (III,Mn)V compounds, as discussed previously. Here we have shown that it is equally reliable to determine the spin-stiffness values in optimally annealed samples of (Ga,Mn)As, and can as well be used to predict the same in other DMS materials.

3.5   Conclusion

 In this part of the work, we have shown that the role of a minimal model approach to study the magnetic and transport properties in diluted magnetic systems is almost indispensable. This proves to be the ideal tool to identify and analyze the relevant physical parameters which control the underlying physics of these systems. The one-band V-J model is shown to provide an overall understanding of the magnetic and transport properties, both qualitatively as well as quantitatively, for a wide range of (III,Mn)V materials. The non-perturbative treatment of the substitution effects combined with a proper treatment of the disorder effects within the V-J model, definitely

gives it an advantage over other existing model studies. For example, this is consistent with the impurity band picture in the case of (Ga,Mn)As, which was reported by first principles based calculations as well as experimental measurements. It is also able to explain the proximity of (Ga,Mn)As to the metal-insulator transition. The model was successful in reproducing the Curie temperatures obtained from first principles based studies for several DMS compounds. It could also reproduce accurately the measured optical conductivity in (Ga,Mn)As, as well as predict those for other materials such as (In,Mn)As and (Ga,Mn)P. Here we have successfully implemented the V-J model to study the Curie temperatures and the magnetic excitation spectrum in optimally annealed (Ga,Mn)As. The calculated Curie temperatures are found to be in excellent agreement with those from *ab initio* based studies, which could accurately reproduce the experimental values. We have also provided a detailed account of the magnon excitation spectrum and evaluated the spin-stiffness as a function of the Mn concentration. Surprisingly we also obtain a remarkable agreement between our model calculations and *ab initio* based studies for the spin-stiffness. In addition, we are also able to reproduce most of the available experimental values for the stiffness. This shows that our simple model is able to capture the relevant physics in these diluted materials. The power of this model lies in its ability to be generalized for a wide class of diluted magnetic materials, and thus it bridges the gap between first principles calculations and model approaches.

However, the question that still remains unanswered is whether it is possible to attain room temperature ferromagnetism in these materials. We have seen from the previous results that (Ga,Mn)As exhibits the highest Curie temperature among these materials, which has also been supported by experimental studies. But this is still far below the much coveted room temperature. This search for room temperature ferromagnetism serves as one of the motivations for the next portion of this work, which forms an essential part of this thesis. Here we would like to remind that so far we have only considered homogeneously diluted systems in all cases, without any correlations in the impurity positions. Now what happens if we have an inhomogeneous distribution of magnetic impurities, or in other words if we

have correlated disorder ? This forms the basis of our study which we are going to present in the following chapter.

Chapter 4

Nanoscale Inhomogeneities in diluted magnetic systems

4.1 Introduction

Until now we have primarily focussed on systems that were homogeneously diluted, that is the magnetic impurities were randomly distributed on the lattice. For a long time people had a firm notion that samples free from any kind of defects and inhomogeneities should lead to room-temperature ferromagnetism, and accordingly huge efforts were made to grow samples as *clean* as possible. However, for these kind of *clean* dilute samples, the highest Curie temperatures measured so far is in (Ga,Mn)As which is ∼170 K for about 7% of Mn[121, 116]. This is also confirmed by our model calculations[111]. Another material which has drawn considerable interest is (Ga,Mn)N, a wide band gap DMS. Different experimental groups have reported T_Cs varying surprisingly as wide as 10 K to 940 K[122, 123, 124, 125, 126] with a typical Mn content between 7 and 9%. Whereas recent theoretical studies, based on model calculations, predict a T_C of 30 K in homogeneously diluted and uncompensated $Ga_{1-x}Mn_xN$ for x=0.06[97], which is in good agreement with those obtained from *ab initio* based studies combined with the SC-LRPA method[57]. Monte Carlo calculations lead to a T_C of 35 K for x=0.06[113, 114] in $Ga_{1-x}Mn_xN$, using the same *ab initio* exchange cou-

plings. These theoretical calculations predict the highest attainable T_C in homogeneously diluted $Ga_{1-x}Mn_xN$. These observations obviously lead to some crucial questions. How do we explain the huge fluctuations of the critical temperatures in these materials? Is there a systematic way to boost the critical temperatures beyond that reported in the homogeneously diluted compounds? The main objective here is to provide an appropriate answer and look into the possible origins of the discrepancies between the theoretical predictions and experimental observations.

As it turns out, the assumption of the homogeneous nature of the samples does not appear to be feasible in realistic cases. Based on first-principles calculations, Sato *et al.*[127] suggested that it is difficult to obtain completely random distribution owing to the strong attractive chemical interactions between the impurities (transition metal ions in the case of DMSs). By calculating the mixing energies of the magnetic impurities in several DMS compounds, such as (Ga,Mn)N, (Ga,Cr)N, (Ga,Mn)As, and (Zn,Cr)Te, the authors showed a strong tendency toward spinodal decomposition in DMSs, which leads to an inhomogeneous distribution of magnetic impurities. (Spinodal decomposition implies alternating regions of low and high concentration of magnetic impurities in the system). Hence it would be unrealistic to completely discard the possibility of such inhomogeneities in these diluted materials. After observation of ferromagnetic order in Mn-doped Germanium (T_C=116 K for x=0.035)[128], several experimental studies reported relatively high critical temperatures ($\sim$ 280 K for x=0.06) in $Ge_{1-x}Mn_x$ films[129, 130, 131, 132]. However, once again the underlying reasons were not obviously clear. In Ref.[133], scanning photoelectron microscopy measurements revealed stripe-shaped Mn rich micro-structures which was believed to be the origin of ferromagnetism in (Ge,Mn). As discussed earlier, in Chapter 1, recent experimental studies have revealed the formation of self-organized Mn rich nanocolumns in $Ge_{1-x}Mn_x$, which gave rise to a very high T_C ($\geq$400 K)[19] for x=0.06. Magnetotransport measurements, in this case, have also shown a large anomalous Hall effect up to room temperature. The spinodal decomposition was suggested to be the reason for the high temperature ferromagnetism in this case. Similar nanometer-sized clusters, with in-
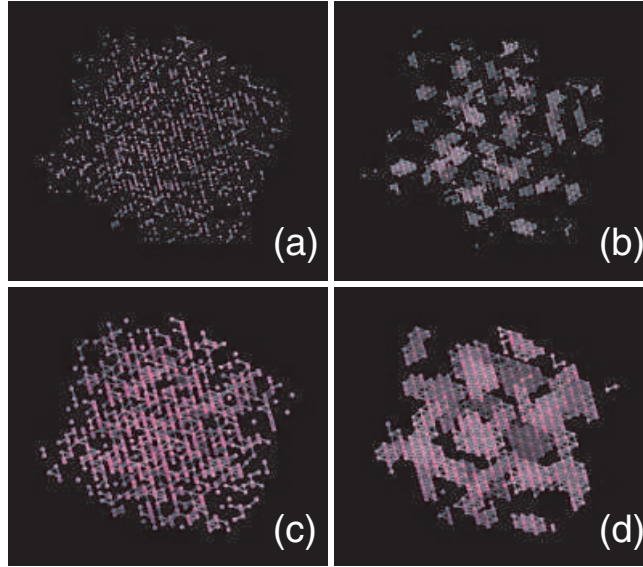
Figure 4.1: Snapshots (Ga,Mn)N for 5% Mn in (a) and (b), and 20% in (c) and (d). Random distributions in (a) and (c), and spinodal decomposition phases (after 100 MC steps) in (b) and (d). (From Ref.[134]).

creased Mn content compared to the surrounding matrix, were also detected by transmission electron microscopy (TEM) analysis in $Ge_{0.95}Mn_{0.05}$[135]. In a different class of diluted materials, the diluted magnetic oxides, recent experimental studies on (Zn,Co)O[136] have claimed the existence of two types of nanoscale ferromagnetic Co clusters. The first were spherical with diameters of about 5 nm leading to critical temperatures of $\sim$100 K and the others were columnar about 4 nm wide, with a maximum height of 60 nm, leading to significantly larger critical temperatures of $\sim$300 K. These results were confirmed by high-resolution transmission electron microscopy (HRTEM). Similar inhomogeneous impurity distributions have been experimentally detected in several other DMSs, such as (Al,Cr)N[137], (Ga,Mn)N[138], and (Zn,Cr)Te[139], by the use of TEM and energy-dispersive x-ray spectroscopy (EDS). Hence the presence of this kind of anisotropic nanoscale inhomogeneity has been established beyond doubt and this can certainly give rise to interesting magnetic and transport properties in these materials.

Now despite the existence of a large body of experimental work, the

effect of impurity clustering in these materials has been weakly studied on the theoretical front. *Ab initio* based studies for these type of inhomogeneous disordered systems are almost impossible to realize due to the large size of supercells required and standard methods are yet to be prescribed. In Ref.[134] the authors have simulated the spinodal decomposition in DMSs by using Monte Carlo (MC) simulations. Figure 4.1 shows the snapshots of this simulated spinodal decomposition phase, corresponding to 5 and 20% of Mn in (Ga,Mn)N. The initial completely random distribution of Mn (after 0 MC steps) are shown in Figure 4.1 (a) and (c), while (b) and (d) indicate the spinodal decomposition phase after 100 MC steps. Interestingly above room-temperature T_C's were predicted for this spinodal phase in (Ga,Mn)As and (Ga,Mn)N, as shown in Figure 4.2. However, the critical temperatures in this case were calculated within the "standard" random phase approximation (RPA). Here by the term "standard" we imply that the crucial self-consistency was not implemented in the calculations. The importance of this aspect will be discussed a little later. As we can see from Figure 4.2, the high T_C's were reported for samples containing sufficiently high concentrations of Mn, above 20%, which is far from the dilute regime. On the other hand in the dilute case, for approximately 5% of Mn, a suppression of the critical temperatures were observed in the presence of spinodal decomposition phases. This decrease was attributed to the absence of a percolating path for a Mn concentration of 5%. We would also like to emphasize that these calculations were performed on relatively small system sizes ($17 \times 17 \times 17$ fcc cells) and the average was done over only 10 configurations. In another work, Rao and Jena[140] have performed DFT based calculations of N-doped Mn clusters and given a hypothesis that a high Curie temperature detected in some of the (Ga,Mn)N samples is a result of the formation of small Mn clusters carrying giant magnetic moments. They attributed the large variation in Curie temperatures to the formation of N induced Mn clusters of different sizes in samples grown under different conditions. Their analyses suggests the importance of the growth mechanism in these kind of materials. Similar density-functional calculations on the effect of microscopic Mn clustering on the Curie temperatures of (Ga,Mn)N were also reported in
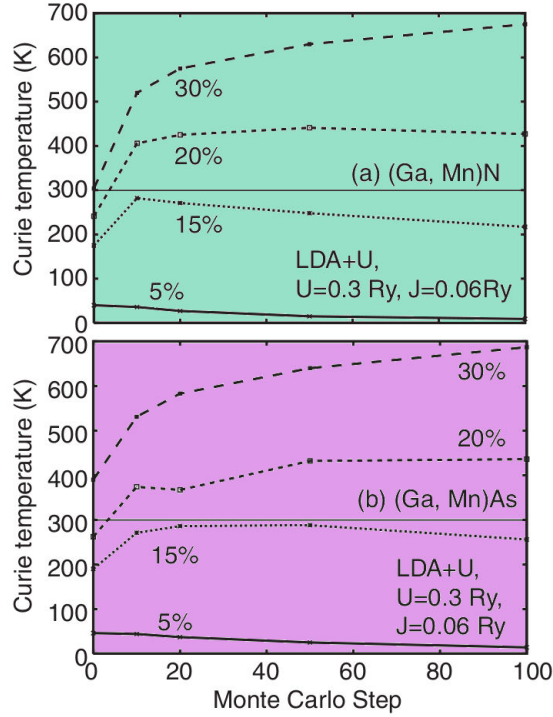
Figure 4.2: Curie temperatures of (a) (Ga,Mn)N and (b) (Ga,Mn)As as function of the number of Monte Carlo steps. (From Ref.[134]).

Ref.[141], but then the T_C's were calculated from mean-field approximation, which is already known to strongly overestimate the critical temperatures in homogeneously diluted systems. In Ref.[142], a theoretical investigation of the impurity correlations and magnetic clustering effects in DMSs was presented from a model Hamiltonian based approach considering classical Heisenberg spins with RKKY-like interactions. However, in this case, the authors found that the impurity correlations have only mild effects on the critical temperatures while the case of random disorder produced the highest T_C.

Hence we see there are several discrepancies and dissensions among the existing theoretical studies, and a proper understanding is still essentially missing. In the following sections, we are going to present a generalized and detailed study of the effect of nanoscale inhomogeneities on the Curie tem-

peratures, the spontaneous magnetization, and the spin excitation spectrum in diluted magnetic systems. As we shall see, the inhomogeneous impurity distribution gives rise to new and interesting features in these systems. For example, in contrast to previous observations, we find a colossal increase in the critical temperatures in presence of inhomogeneities. There are several factors which are found to play an important role, such as the concentration of inhomogeneities in the system, the relative size of the inhomogeneities, the concentration of magnetic impurities inside the inhomogeneities as well as the range of the effective exchange interactions. We try to provide a detailed analyses of the combined effects of these physical parameters on the different properties of these inhomogeneous diluted systems.

4.2 Effect of nanoclusters on the critical temperatures

In this section we will study the effects of inhomogeneities on the critical temperatures in diluted magnetic systems. For reasons of simplicity we have assumed here a simple cubic lattice for all calculations but it is important to note that the conclusions that will be drawn are general in nature. The inhomogeneities that we consider here are of spherical shape of radii r_0. In order to avoid additional parameters, in all our calculations the total concentration of impurities in the system is fixed to x=0.07. In the following we denote the concentration of nanospheres by x_{ns}=N_S/N, where N_S is the total number of sites included in all the nanospheres and N=L^3 is the total number of sites in the system. The concentration of impurities inside each nanosphere is denoted by x_{in}. The total number of impurities in the system and the number of impurities inside the nanospheres is given by N_{imp}^{tot} and N_{imp}^{in} ($=x_{in}N_S$) respectively. Now, as a first step, the nanospheres are generated randomly on the simple cubic lattice subject to the restriction that there is no overlap between them. Figure 4.3 shows snapshots of four typical random configurations corresponding to four different concentrations of nanospheres x_{ns} (0.02, 0.04, 0.06, and 0.08)[143]. As we increase the number of nanospheres in the
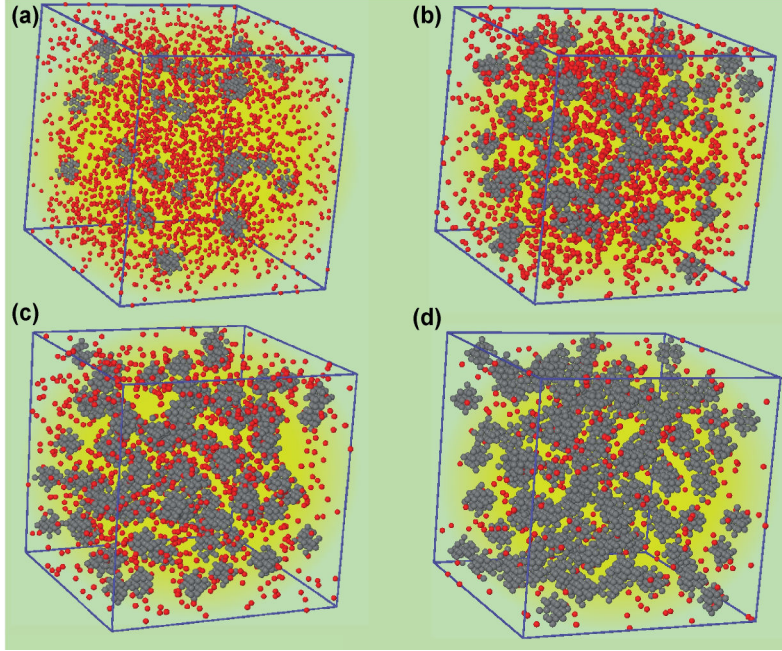
Figure 4.3: Snapshots corresponding to four different concentrations of nanospheres x_{ns} (a) 0.02, (b) 0.04, (c) 0.06 and (d) 0.08. The grey (red) atoms denote the impurities inside (outside) the nanospheres. (Here L=36, r_0=2a, and x_{in}=0.8). (From Ref.[143]).

system, x_{ns} increases and consequently the concentration of impurities outside decreases, since the total concentration of the system (x) is fixed. Now in order to evaluate the Curie temperatures, we treat the effective diluted Heisenberg Hamiltonian H_{Heis}=-$\sum_{i,j} J_{ij} \mathbf{S}_i \cdot \mathbf{S}_j$, within the SC-LRPA theory. We have already established the accuracy and reliability of the SC-LRPA to treat disorder and/or dilution effects in these systems, as shown in the previous chapters. The T_C is calculated for each random configuration and then averaged over a few hundred configurations of disorder. A proper sampling over disorder is very essential as the Curie temperatures can be sensitive to the kind of configurations in these inhomogeneous diluted systems, as we shall see shortly.

Now as we have seen previously, the exchange couplings in DMSs, obtained from *ab initio* based studies, are relatively short range in nature, al-

most exponentially decaying and ferromagnetic in nature[92, 113, 114]. Thus, without any loss of generality, for our study we have considered here generalized couplings of the form $J_{ij}=J_0 \exp(-|\mathbf{r}|/\lambda)$, where $\mathbf{r}=\mathbf{r}_i\text{-}\mathbf{r}_j$ and λ is the damping parameter. Now in the case of (Ga,Mn)As, for about 5% Mn a fit of the *ab initio* magnetic couplings provides a value of λ of the order of $a/2$. It should be noted that in the case of (Ga,Mn)N the *ab initio* couplings are of even shorter range. We will focus here on two particular cases, $\lambda=a$ and $\lambda=a/2$, where a is the lattice spacing. Although these length scales seem to be comparable, in the presence of inhomogeneities the effects on the critical temperatures as well as other magnetic properties can be very drastic. Now in order to measure directly the effects of the nanoscale inhomogeneities, we scale the averaged Curie temperatures of the inhomogeneous case $\langle T_C^{inh} \rangle$ with respect to the averaged Curie temperatures of the homogeneously diluted system $\langle T_C^{hom} \rangle$ for the same concentration $x=0.07$, and we denote their ratio by $\langle R_C \rangle$. The averaged Curie temperatures $\langle T_C^{hom} \rangle$ for the homogeneously diluted case are found to be 0.9 J_0 and 0.05 J_0, for $\lambda=a$ and $a/2$ respectively, for $x=0.07$.

In Table 4.1 we have provided the averaged Curie temperatures for systems containing 80%, 70%, 60%, and 40% homogeneously distributed magnetic impurities scaled with respect to that of the 7% homogeneous case, for $\lambda=a$ and $a/2$ respectively. This ratio is denoted by $\langle R^{hom} \rangle$. As stated earlier, the concentration of impurities within the inhomogeneities can also have a non-trivial effect on the critical temperatures. So the reason to consider the critical temperatures for such high concentrations will become clear in the discussions to follow, where we will assume similar kind of impurity concentration inside the nanospheres and try to analyze their relative effects on T_C.

4.2.1   Systems with relatively extended couplings

We begin with the case of the relatively long ranged couplings corresponding to $\lambda=a$. In Figure 4.4 we show $\langle R_C \rangle$ as a function of $N_{imp}^{in}/N_{imp}^{tot}$. In this case, we fix the concentration inside the nanospheres to $x_{in}=0.8$ and the

x	$\langle \mathrm{R}^{hom} \rangle$ $(\lambda=a)$	$\langle \mathrm{R}^{hom} \rangle$ $(\lambda=a/2)$
0.8	9.7	22
0.7	8.9	20
0.6	7.9	17
0.4	5.2	11

Table 4.1: The ratio, $\langle \mathrm{R}^{hom} \rangle$, of the homogeneous Curie temperatures for different x to that of $x=0.07$, for $\lambda=a$ and $a/2$ respectively.

T_C's are calculated for spheres of different radii. For this x_{in}, each nanosphere contains 5, 15, 26, 45 and 64 impurities for $r_0=a$, $\sqrt{2}a$, $2a$, $\sqrt{5}a$ and $\sqrt{6}a$ respectively. $N^{in}_{imp}/N^{tot}_{imp}=0$ corresponds to the homogeneously diluted case. A clear increase in the critical temperatures is observed with increasing fraction of impurities inside the nanospheres as well as with the nanospheres' size. For about 80% of the total impurities inside the nanospheres, T_C is enhanced by up to 150% for the smallest nanospheres with $r_0=a$ and almost 350% for the ones with $r_0=\sqrt{6}a$, which is already significant. This increase, for $r_0=\sqrt{6}a$, is more than one-third of that found for the 80% homogeneously distributed case (Table 4.1). Hence this shows that clustering of magnetic impurities can lead to a considerable increase of the critical temperatures due to the strong interactions within the nanospheres. The other important thing which we observe here is the T_C predicted by the mean-field virtual crystal approximation (VCA). As we have already seen, in many previous cases, the MF-VCA overestimates the true critical temperatures and often very strongly. However, in this case, our results show that in the presence of inhomogeneities the VCA value can no longer serve as an upper bound. Indeed, as can be seen from the figure, even for relatively small concentrations of nanospheres ($x_{ns}\sim 0.2$) we already surpass the VCA value, and for higher density of nanospheres the VCA in fact strongly underestimates the critical temperatures in these systems. This is contrary to what is generally observed in the case of homogeneously diluted systems, and at the same time

Figure 4.4: $\langle R_C \rangle$ as a function of $N_{imp}^{in}/N_{imp}^{tot}=(x_{in}/x)x_{ns}$ for $\lambda=a$. For a fixed $x_{in}=0.8$ and different radii r_0. The upper x-axis represents the values of x_{ns} corresponding to $x_{in}=0.8$. The solid red line indicates the T_C^{VCA} scaled w.r.t $\langle T_C^{hom} \rangle$. (Here squares and circles correspond to $L=32$ and $L=36$). (From Ref.[143]).

this also establishes the inaccuracy of the mean-field VCA to determine the critical temperatures in systems with inhomogeneities.

In the previous figure, we have shown the effects of the size of the inhomogeneities on the Curie temperatures, for a fixed x_{in}. Now what happens if we change the concentration of impurities inside the nanospheres ? For this we consider the case of nanospheres with fixed radii $r_0=2a$ and varying concentrations x_{in}. Figure 4.5 shows $\langle R_C \rangle$ as a function of $N_{imp}^{in}/N_{imp}^{tot}$ for different x_{in}. We see an overall monotonous increase in the Curie temperatures with increasing the concentration of nanospheres. However, what is interesting to observe here is that the enhancement of the critical temperatures also depends on the concentration of impurities inside the nanospheres. Decreasing the concentration inside the nanospheres effectively means re-

Figure 4.5: $\langle R_C \rangle$ as a function of $N_{imp}^{in}/N_{imp}^{tot}$ for $\lambda=a$, for a fixed $r_0=2a$ and different x_{in}. The solid red line indicates the T_C^{VCA} scaled w.r.t $\langle T_C^{hom} \rangle$. (Here squares correspond to $L=32$ and circles to $L=36$). (From Ref.[143]).

ducing the number of impurities inside a cluster of the same size and thus less inter-nanosphere interactions. This could possibly explain the relatively small increase in the T_C values with decreasing x_{in}. However, as we will see in what follows, the variation of the critical temperatures can be more complex than this simple picture. Hence we find that not only the relative concentration of nanospheres in the system but also the concentration inside the nanospheres can have a significant effect on the critical temperatures.

4.2.2 The case of short-ranged couplings

Now we move to the case of the shorter ranged couplings, $\lambda=a/2$, which will appear even more interesting and leads to surprising effects. Figure 4.6 shows the $\langle R_C \rangle$ as a function of $N_{imp}^{in}/N_{imp}^{tot}$ for a fixed $x_{in}=0.8$. T_C is calculated for nanospheres of different radii ($r_0=a$, $\sqrt{2}a$, $2a$, $\sqrt{5}a$ and $\sqrt{6}a$). We have
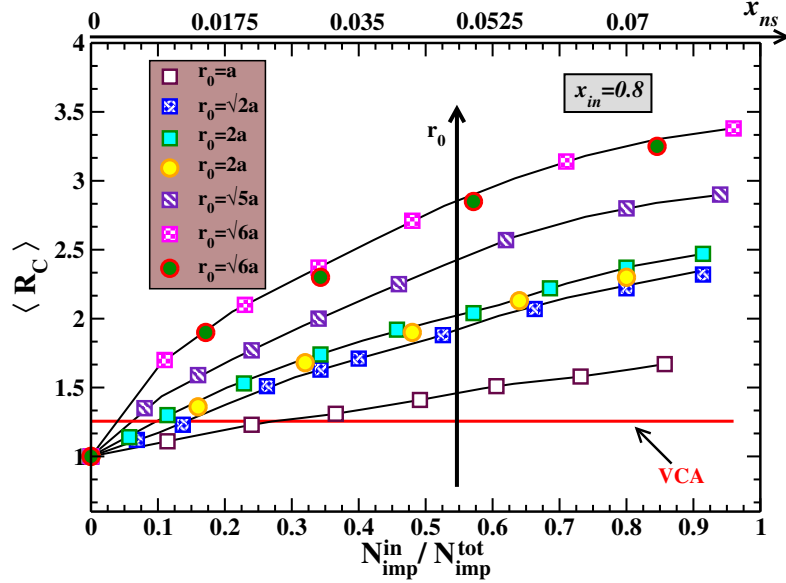
Figure 4.6: $\langle R_C \rangle$ as a function of $N_{imp}^{in}/N_{imp}^{tot}=(x_{in}/x)x_{ns}$ corresponding to $\lambda=a/2$. For a fixed $x_{in}=0.8$ and different r_0. The upper x-axis represents the values of x_{ns} corresponding to $x_{in}=0.8$. The solid red line indicates the T_C^{VCA} scaled w.r.t $\langle T_C^{hom} \rangle$. (Here squares correspond to $L=32$, circles to $L=36$, triangles to $L=40$ and diamonds to $L=44$). (From Ref.[143]).

considered system sizes varying from $L=32$ to $L=44$ to check for the finite size effects. The $L=44$ systems typically contain ~6000 impurities. In contrast to the case of $\lambda=a$ discussed above, the variation of T_C with $N_{imp}^{in}/N_{imp}^{tot}$ is not monotonous anymore. Here we see a colossal effect of the size of the nanospheres on the T_C. For the smallest nanospheres ($r_0=a$) there is hardly any noticeable effect, the critical temperatures remaining close to that of the homogeneous case. Now as we increase the radius of the nanospheres for a given concentration of nanospheres, there is a sharp and strong increase in the T_C values. As can be seen, even for a reasonably small concentration of nanospheres ($x_{ns}\sim0.2$) we obtain a remarkable jump of almost 900% for $r_0=2a$ and even 1600% for $r_0=\sqrt{6}a$, compared to that of the homogeneous case. This gigantic increase in the presence of nanospheres with $r_0=\sqrt{6}a$,

is more than 70% when compared to the T_C of the 80% homogeneous case (Table 4.1), which is rather extraordinary. This implies that in materials like (Ga,Mn)N, where the exchange interactions are really short ranged, it would be possible to reach a $T_C \geq 500$ K (as T_C for homogeneously diluted $Ga_{1-x}Mn_xN=40$ K for $x=0.07$[58, 57, 66]) by inducting nanoscale inhomogeneities. The presence of such nanoclusters may also explain the very high T_C's observed in $Ga_{1-x}Mn_xN$ by some experimental groups[126]. Hence it should be of great interest to analyze experimentally the effect of such nanoclusters on the critical temperatures in these kind of materials. Here again the mean field VCA is found to strongly underestimate the critical temperatures for most cases. This is expected since the mean-field VCA treatment is unable to capture all the relevant physical effects in both homogeneously disordered as well as inhomogeneous systems. Thus it becomes clear that in systems with relatively short ranged couplings the size of the inhomogeneities plays a very important role in controlling the critical temperatures. The non-monotonous behavior observed here indicates that several physical parameters such as typical length scales and relevant couplings compete to give rise to this new physics. Hence it is not straightforward to explain this variation by assuming the inhomogeneities to behave as 'super-spins' only.

In Figure 4.7 we consider the case of nanospheres of fixed radii $r_0=2a$, which is particularly interesting. $\langle R_C \rangle$ is shown as a function of $N_{imp}^{in}/N_{imp}^{tot}$ for different x_{in} (0.8, 0.7, 0.6 and 0.4). For a fixed x_{in}, we observe a gradual increase in the critical temperatures with increasing concentration of nanospheres and then it decreases with x_{ns} increasing further. In contrast to the case of $\lambda=a$, there is a clear maximum in the T_C around $N_{imp}^{in}/N_{imp}^{tot} \sim 0.2$ for $x_{in}=80\%$ and 70%. For this value of $N_{imp}^{in}/N_{imp}^{tot}$ as we increase the concentration inside the nanospheres we observe a huge jump in the critical temperatures, from a small increase for $x_{in}=40\%$ to almost 900% for $x_{in}=80\%$, compared to that of the homogeneous case. It should be noted that for $N_{imp}^{in}/N_{imp}^{tot}=0.9$ and $x_{in}=80\%$ the increase is reduced to about 600%, which is still considerably large. Whereas for $x_{in}=40\%$ we hardly obtain any significant increase compared to that of the homogeneous case. Hence in this case the concentration inside the nanospheres is found to have a crucial effect on
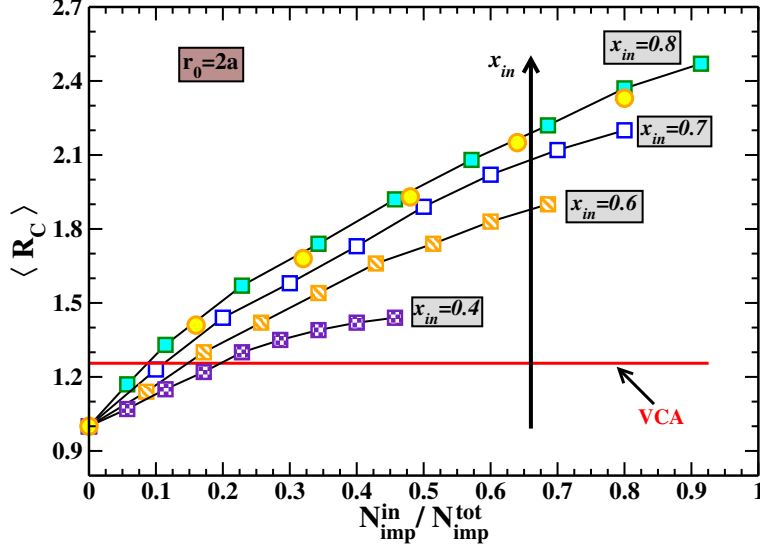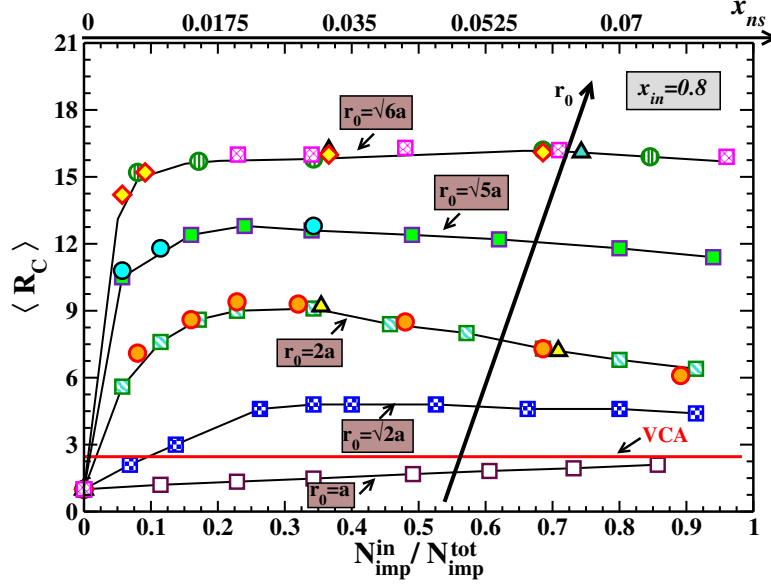
107
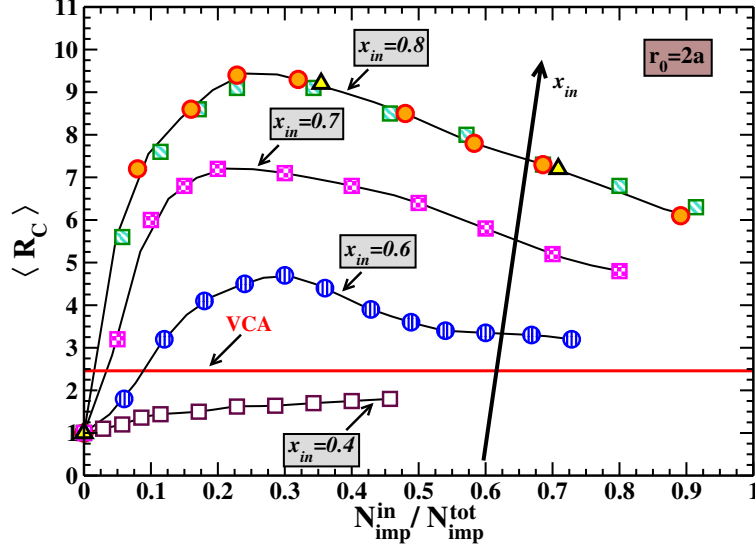
Figure 4.7: $\langle R_C \rangle$ as a function of $N_{imp}^{in}/N_{imp}^{tot}$ corresponding to $\lambda=a/2$. For a fixed $r_0=2a$ and different x_{in}. The solid red line indicates the T_C^{VCA} scaled w.r.t $\langle T_C^{hom} \rangle$. (Here squares correspond to $L=32$, circles to $L=36$, and triangles to $L=40$). (From Ref.[143]).

determining the critical temperatures of the system. Now in order to understand this unusual behavior, we have performed a careful statistical analysis of the T_C's for the particular case of $r_0=2a$. In the following we provide a detailed study of the Curie temperature distributions and try to analyze the reasons for the origin of this kind of behavior.

4.2.3 Detailed analyses of the critical temperature distributions

1. Case of $\lambda=a$

First we show the normalized R_C distributions corresponding to the case of $\lambda=a$, $r_0=2a$, and $x_{in}=0.8$ in Figure 4.8. The distributions shown correspond to an averaging over several hundred configurations of disorder ($\sim$500). We

observe that for all concentrations of nanospheres, the distributions are fairly uniform and relatively narrow. In fact the width of the distributions are comparable for each case. For x_{ns}=0.02, the R_C distribution is somewhat asymmetric, but with increase in the inhomogeneities concentration they become more symmetric. This regular nature of the distributions is consistent with the monotonous increase of the Curie temperatures, seen in Figure 4.5. We do not notice any unusual or unexpected behavior in this case. We can also say that for larger values of λ, the critical temperature distributions should exhibit even more symmetric behavior.
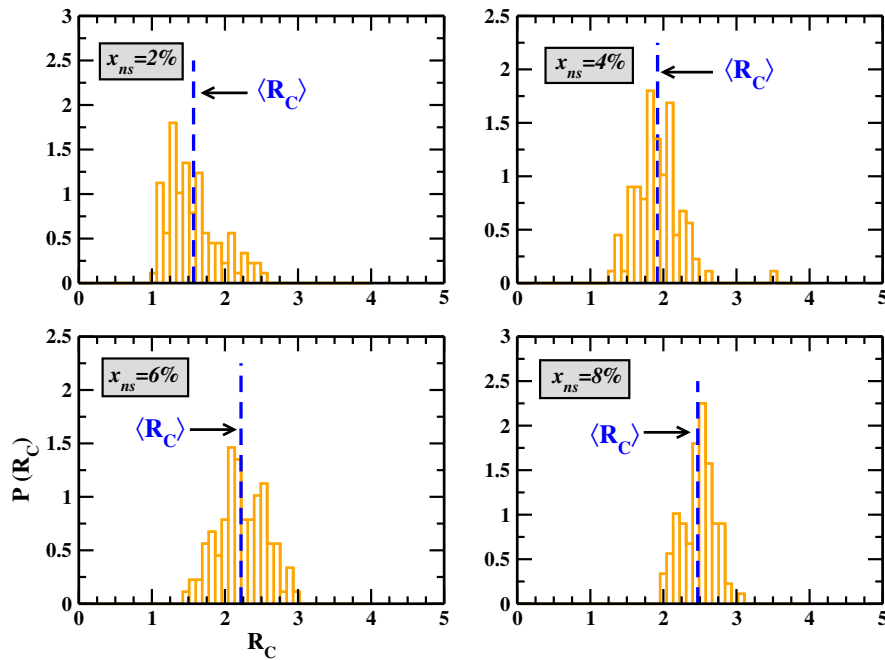
Figure 4.8: Normalized R_C distributions for four different x_{ns}: 0.02, 0.04, 0.06, and 0.08 corresponding to λ=a. Here r_0=2a, x_{in}=0.8 and L=32. The blue dashed lines indicate the $\langle R_C \rangle$ values which we have shown in Figure 4.5. (From Ref.[144]).
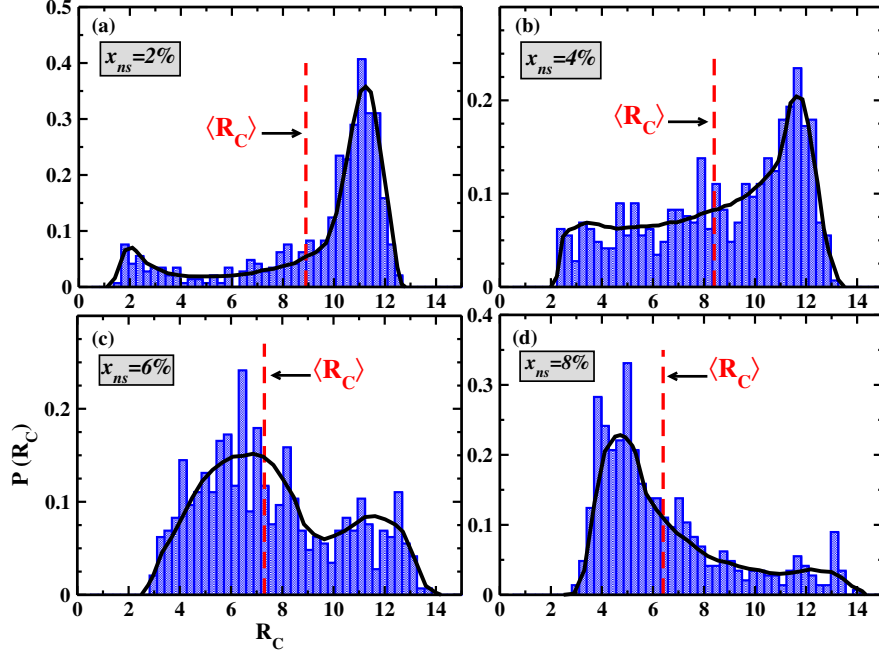
Figure 4.9: Normalized R_C distributions for four different x_{ns}, (a) 0.02, (b) 0.04, (c) 0.06, and (d) 0.08 corresponding to $\lambda=a/2$. Here $r_0=2a$, $x_{in}=0.8$ and $L=32$. The red dashed lines indicate the $\langle R_C \rangle$ values which we have shown in Figure 4.7. (From Ref.[143]).

2. Case of $\lambda=a/2$

Now in Figure 4.9 we show the corresponding distributions for the case of $\lambda=a/2$, $r_0=2a$, and $x_{in}=0.8$. Here too the distributions are obtained using a sampling over several hundred configurations of disorder . In this case we obtain very interesting wide distributions for the different concentrations of nanospheres. For $x_{ns}=0.02$, we observe a kind of bimodal distribution, one peak with a large weight at *high* T_C ($T_C^{high} \sim 11 \langle T_C^{hom} \rangle$) values and another one at *low* T_C ($T_C^{low} \sim 2 \langle T_C^{hom} \rangle$) with a much smaller weight. When increasing x_{ns} to 0.04, the width of the distribution is almost unaffected but we notice a clear transfer of weight from the high T_C values to the lower one. By further increasing x_{ns} to 0.06, the transfer of weight increases further, the

110

low T_C region has a significantly larger weight. Finally for relatively high x_{ns} ($\sim$0.08), the weight is now concentrated around the lower T_C values and the distribution exhibits a tail like structure at higher critical temperatures. This transfer of weight is the reason for the maximum in the T_C observed in Figure 4.7. The origin of this kind of distribution is not so obvious in the beginning. However, the analysis of the configurations revealed an interesting feature. We have considered two different kinds of configurations. The first set of configurations of nanospheres corresponds to the situation where the distance between the nanospheres is restricted to small separation. The second kind corresponds to large separations between the nanospheres. First it is found that in both cases the distribution of T_C is relatively narrow and unimodal. However in the first case the T_C distribution is centered around T_C^{low} whereas in the second case it is centered around T_C^{high}. It is somehow surprising and counter-intuitive that the largest T_Cs are obtained from the configurations where the inter-nanosphere couplings are weaker. Now the nature of distributions shown in Figure 4.9 can be explained as follows. In the case of low concentration of nanosphere (Figure 4.9 (a)) the probability to find the nanospheres relatively far apart from each other is high and respectively the probability to find them close to each other is relatively small. Hence this leads, in the distribution, to a significant weight around the high T_C values. As we gradually increase x_{ns}, the probability to find configurations with the nanospheres at relatively large separation decreases while those corresponding to small separation increases. As a consequence the weight in the distribution around T_C^{high} reduces and that corresponding to the low T_C increases, as observed in Figure 4.9 (b)-(c). Finally for the largest x_{ns}($\sim$0.08) the weight is mainly concentrated around the low T_C region (Figure 4.9 (d)). Interestingly this kind of behavior is not observed in the case of λ=a (Figure 4.8). In that case, the distribution of the critical temperatures is always found to be relatively narrow and unimodal. This implies that all kinds of configurations (nanospheres far apart or close to each other) leads to similar values of the critical temperature.

4.2.4 Crucial role and importance of self-consistency in inhomogeneous systems

Let us now briefly discuss the importance of the self-consistent treatment within the RPA, which we have adopted throughout all the calculations performed till now. In order to demonstrate the effects of the self-consistency on the calculation of the Curie temperatures, we have plotted in Figure 4.10(a)

Figure 4.10: (a) $\langle R_C \rangle^{NS-RPA}$ as a function of $N_{imp}^{in}/N_{imp}^{tot}$ corresponding to $\lambda = a$. For a fixed $x_{in}=0.8$ and different r_0. (b) $\langle R_C \rangle^{LRPA}/\langle R_C \rangle^{NS-RPA}$ for the same parameters. (Here $L=32$). (From Ref.[144]).

$\langle R_C \rangle^{NS-RPA}$ as a function of $N_{imp}^{in}/N_{imp}^{tot}$, corresponding to the case of $\lambda = a$.

112

Here the subscript 'NS-RPA' stands for the non-self-consistent RPA. In the self-consistent LRPA expression for the Curie temperature, the parameters $\lambda_i = lim_{T \to T_C} \langle S_i^z \rangle / m$, ($i$=1,2,...$N_{imp}$) are determined self-consistently at each temperature (see Equation B.22 in Appendix B). Whereas in the NS-RPA approach, λ_i=1 for all values i. The localization effects are taken into consideration but the self-consistency is excluded. Now in the present case, the concentration inside the nanospheres is kept fixed at x_{in}=0.8 and the T_C's are calculated for different r_0. These parameters are chosen in order to facilitate a direct comparison with the results corresponding to the SC-LRPA, shown in Figure 4.5. At a first glance we indeed observe a monotonous increase of the Curie temperatures with increasing fraction of impurities within the nanospheres as well as the size of the nanospheres. The qualitative nature of the curves is similar to what is observed in Figure 4.5. However if we plot the ratio of the Curie temperatures obtained within our self-consistent approach and those determined from the NS-RPA, as shown in Figure 4.10(b), we find that the NS-RPA underestimates the critical temperatures by a fair amount. The magnitude of this underestimation increases with the increase in the size of the inhomogeneities. For example, in the case of the smallest nanospheres with r_0=a, for $N_{imp}^{in}/N_{imp}^{tot} \sim 0.3$, the T_C is underestimated by only about 5%. But for larger radii of nanospheres, such as r_0=2a, this underestimation is about 15%, and for r_0=$\sqrt{6}a$, this is almost up to 35%. This already shows the importance of the self-consistent treatment as well as the fact that the NS-RPA approach is not adequate to calculate the critical temperatures reliably in these inhomogeneous systems.

Now we come to the more interesting case of the relatively short ranged couplings (λ=a/2). Figure 4.11(a) shows $\langle R_C \rangle^{NS-RPA}$ as a function of the $N_{imp}^{in}/N_{imp}^{tot}$, for a fixed x_{in}=0.8 and different values of r_0. Unlike the case of λ=a, the qualitative nature of the curves shown here bear no resemblance to what was obtained within the self-consistent treatment. We observe a steady increase in the Curie temperatures with increase in the fraction of the impurities inside the clusters as well as increase in the size of the clusters, in this case. The NS-RPA calculations fails to reproduce the non-monotonous behavior which was observed in certain cases, as shown in Figure 4.7. More-
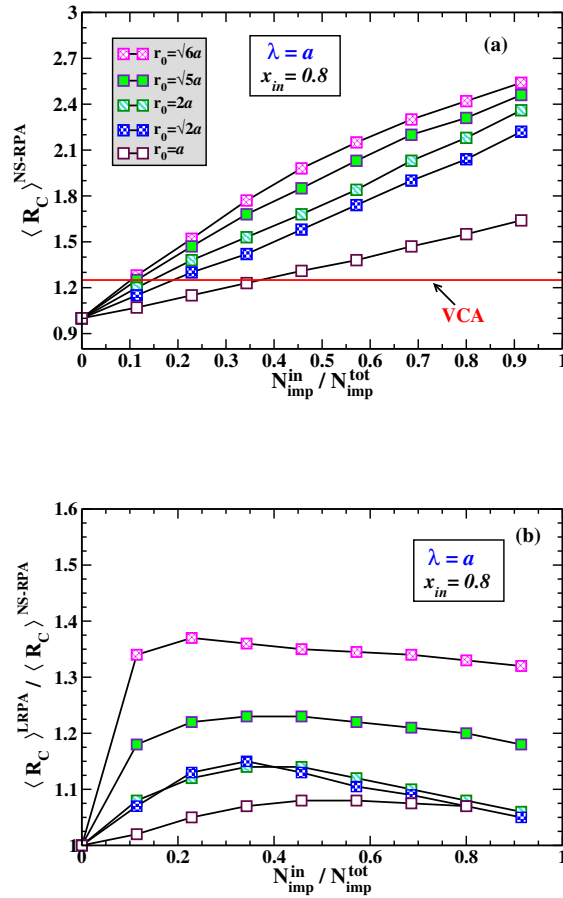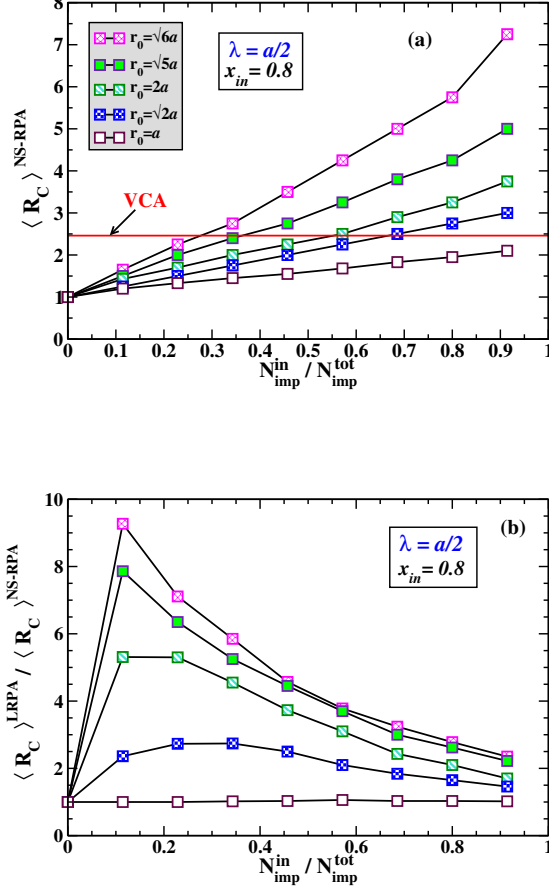
Figure 4.11: (a)$\langle R_C \rangle^{NS-RPA}$ as a function of $N_{imp}^{in}/N_{imp}^{tot}$ corresponding to $\lambda=a/2$. For a fixed $x_{in}=0.8$ and different r_0. (b) $\langle R_C \rangle^{LRPA}/\langle R_C \rangle^{NS-RPA}$ for the same parameters. (Here $L=32$). (From Ref.[144]).

over this approach can also lead to some serious underestimations. To analyze this we have plotted in Figure 4.11(b), the ratio $\langle R_C \rangle^{LRPA}/\langle R_C \rangle^{NS-RPA}$ as a function of $N_{imp}^{in}/N_{imp}^{tot}$, for the same parameters and corresponding values of r_0, as shown in Figure 4.11(a). We immediately observe that the critical temperatures are underestimated strongly for increasing size of the nanospheres. For $r_0=a$, there is hardly any noticeable difference between the two approaches. However, for $N_{imp}^{in}/N_{imp}^{tot} \sim 0.2$, we find that the NS-RPA un-

derestimates the critical temperatures by more than 50% for $r_0{=}2a$, and by almost 80% for $r_0{=}\sqrt{6}a$. The underestimations can be found to be relatively small for larger fraction of impurities within the nanospheres. Nevertheless, this shows that the NS-RPA, underestimates the critical temperatures significantly, in certain cases, in systems with effective short ranged interactions. Hence this is not the best tool to calculate the Curie temperatures in systems with inhomogeneities as it can lead to strong underestimations of the true critical temperatures. Thus the importance and the validity of the self-consistent treatment adopted within our approach stands vindicated.

4.2.5 Remarks on measured T_C in (Ga,Mn)N and (Ge,Mn)

In the context of the above results, we would like to draw attention to the following important point. We have found that in systems with effective short ranged exchange interactions it is possible to obtain two different critical temperatures depending on the size and concentration of the inhomogeneities and also the typical separation between them. For example, in the case of $\lambda{=}a/2$, for nanospheres of radii $r_0{=}2a$, $x_{ns}{=}0.02$ and $x_{in}{=}0.8$, the T_C^{high} value is almost *five* times that of the T_C^{low} value. This could possibly explain the wide range of T_C values observed experimentally for materials like (Ga,Mn)N[122, 123, 124, 125, 126] and the apparent dissension between theoretical predictions and experimental observations for these kind of materials. It is interesting to note in this context, that Li *et al.*[145] proposed two different ordering temperatures in $Ge_{1-x}Mn_x$, T_C and T_C^* with $T_C{\ll}T_C^*$. The higher critical temperature T_C^* is associated with the ferromagnetic ordering temperature within isolated spin clusters and the onset of global ferromagnetism only occurs at T_C. For $x{=}0.05$ the values of T_C and T_C^* were found to be 12 K and 112 K respectively. However, further detailed experimental studies on these materials would help to substantiate these results.

4.3 Unconventional Temperature dependence of the Spontaneous Magnetization

As we know, owing to the strong motivation of attaining room-temperature ferromagnetism for possible spintronics applications, the Curie temperature has been the primary focus of research in the diluted magnetic materials. In the previous section we have seen that the presence of nanoscale inhomogeneities can lead to very high T_C's (often above room-temperature) in diluted magnetic systems with very short ranged exchange couplings. However, another important aspect which can help to further reveal the nature of ferromagnetism in these strongly disordered systems is the temperature dependence of the spontaneous magnetization $M(T)$. Among the many interesting features that magnetization possesses, some worth noting are the concavity/convexity of the curve and the critical behavior near the transition point. In the particular case of DMSs, one of the very first observations of ferromagnetism in (In,Mn)As[18], revealed a surprising non-mean-field like behavior of the spontaneous magnetization with temperature. The experimentally determined magnetization curve had an unusual outward concave-like shape which is in stark contrast to the typical convex behavior obtained within the standard Weiss mean-field theory[146] as well as that observed in conventional ferromagnetic materials. The (In,Mn)As samples studied in Ref.[18] were reported to be insulating, and similar concave $M(T)$ behavior was also observed in insulating samples of $Ge_{1-x}Mn_x$ determined by superconducting quantum interference device (SQUID) magnetometry and magnetotransport measurements[128]. Theoretical predictions, based on a percolation transition of bound magnetic polarons in the strongly localized regime[147], were made to explain this non-mean-field like magnetization behavior. Similar magnetization behavior in DMS systems, in the insulating regime, was also predicted by other theoretical studies based on numerical calculations[148, 149, 150]. The deviation in the $M(T)$ behavior from the standard Brillouin-function shape is believed to be partly due to the small carrier density compared to the localized spin density, as well as due to the wide distribution of the exchange interactions and

116

hopping integrals[150]. On the other hand, in metallic DMSs, for example $Ga_{1-x}Mn_xAs$ for x=0.05−0.10, the magnetization behavior is found to be almost linear in temperature[151, 152]. This behavior is somewhat intermediate between the concave-like $M(T)$ curves in the insulating regime and the classic convex magnetization. However, experimental studies suggest that annealing treatments can have a strong effect on the nature of the magnetization behavior[115, 153]. Upon optimal annealing the magnetization curves are found to become more convex and Brillouin-function-like compared to their linear behavior before annealing. This anomalous behavior of the magnetization once again highlights the importance of disorder in these systems.

In this section we are going to study the spontaneous magnetization in diluted magnetic systems from a generalized perspective. Our main focus is to analyze the effect of nanoscale inhomogeneities on the spontaneous magnetization behavior in these systems, which has rarely been studied until now. Most of the theoretical studies mentioned before were based on mean-field-like theories, which we know is inadequate to treat disorder in these systems. In Ref.[154], the authors have used some complementary theoretical approaches in addition to the mean-field theory, which include the dynamical mean-field theory (DMFT), to study the magnetization in doped magnetic semiconductors. However, their DMFT results were found to be qualitatively similar to those of the standard mean-field theory. Also the effects of correlations in disorder have hardly been considered in any of the previous studies. Here we first study the nature of the magnetization in homogeneously diluted systems with no correlation in impurity positions, and then extend this to systems containing clusters of magnetic impurities. We will observe interesting deviations from the homogeneous magnetization curves. The presence of inhomogeneities gives rise to unusual and anomalous behavior of the temperature dependent magnetization. Again this is found to depend on the several relevant physical parameters, as was observed in the case of the Curie temperatures.

4.3.1 Summary of the calculation procedure

Now to calculate the spontaneous magnetization, we start with the effective diluted Heisenberg Hamiltonian $H_{Heis} = -\sum_{i,j} J_{ij} \mathbf{S}_i \cdot \mathbf{S}_j$, which is treated within the SC-LRPA theory (as in Section 4.2). The impurity spins are assumed to be classical, although this theory is valid for quantum spins as well. We consider a fully polarized, collinear ferromagnetic ground state at $T=0$ K, assumed in the z-direction. Within the SC-LRPA formalism, for a given disorder configuration, the local magnetizations $\langle S_i^z \rangle$ ($i=1, 2, ..., N_{imp}$) are calculated self-consistently at each temperature. The local magnetization is evaluated using the Callen like expression[63],

$$\langle S_i^z \rangle = \frac{(S - \Phi_i)(1 + \Phi_i)^{2S+1} + (1 + S + \Phi_i)\Phi_i^{2S+1}}{(1 + \Phi_i)^{2S+1} - \Phi_i^{2S+1}} \tag{4.1}$$

where

$$\Phi_i = \int_{-\infty}^{+\infty} \frac{\rho_i(\omega)}{exp(\omega/k_B T) - 1} d\omega \tag{4.2}$$

and $\rho_i(\omega) = -\frac{1}{2\pi\langle S_i^z \rangle}\Im G_{ii}(\omega)$ is the local magnon DOS at site i. Following this the average magnetization of the system is given by

$$\langle S_z^{avg} \rangle = \frac{1}{N_{imp}} \sum_i \langle S_i^z \rangle \tag{4.3}$$

Here again we assume a simple cubic lattice with periodic boundary conditions. We fix the total concentration of impurities in the system to $x=0.07$, as before. The inhomogeneities are assumed to be of spherical shape of radii r_0. The concentration of impurities inside each nanosphere is denoted by x_{in}. In this case, to avoid additional parameters and for the sake of simplicity, we restrict ourselves to nanospheres of fixed radii $r_0=2a$ (a is the lattice spacing) and $x_{in}=0.8$. The concentration of nanospheres in the system is defined by $x_{ns}=N_S/N$, where N_S is the total number of sites included in all the nanoclusters and $N=L^3$ is the total number of sites in the system. The configurations are generated in a similar fashion as described in the previ-

ous section. Now concerning the exchange interactions, we have assumed isotropic interactions of the form $J_{ij}=J_0\exp(-|\mathbf{r}|/\lambda)$, same as the ones we had used to calculate the Curie temperatures. The justification to consider these type of couplings in the case of DMSs were discussed in the previous section. In the following we consider a range of λ's (the damping parameter), corresponding to relatively long-ranged couplings down to short-ranged ones, and try to analyze their effects on the magnetization behavior.

4.3.2 Magnetization curves in Homogeneous systems

We first consider the homogeneously diluted case where the magnetic impurities are randomly distributed on the simple cubic lattice. Figure 4.12 shows the average magnetization for different values of λ, corresponding to one configuration of disorder, as a function of the reduced temperature T/T^*, where T^* is the temperature corresponding to the situation when $\langle S_z^{avg}\rangle=0.001S$. We consider the temperature T^*, instead of the actual T_C, as it is difficult to obtain an absolute convergence of the average magnetization as $T{\rightarrow}T_C$, as also the fact that here we are interested to study the nature of the magnetization curves and not the exact critical temperatures. Now as we can see from the figure, for relatively long-ranged couplings ($\lambda{=}2a$), the magnetization curve has a typical convex shape which is the usual behavior predicted by the standard mean-field theories[146], and observed frequently in conventional ferromagnetic materials. Now on decreasing λ, we notice that the convexity decreases sharply and for $\lambda{=}a/3$ the magnetization is almost linear over a broad temperature range. In fact similar behavior (linearity) of the magnetization was observed in metallic samples of (Ga,Mn)As by magnetic circular dichroism (MCD) studies[151]. This shows that the relatively short-ranged interactions are more relevant for the case of DMS materials and also vindicates the choice for our exchange couplings. In order to have a qualitative idea of the relative change in the behavior of the magnetization with λ, we have plotted in the inset of Figure 4.12 the curvature (κ) of the magnetization curves at the specific value of $T/T^*{=}0.5$. The curvature is defined by $\kappa{=}\left|\frac{\partial^2\langle S_z^{avg}\rangle/S}{\partial u^2}\right|\left(1+\left[\frac{\partial\langle S_z^{avg}\rangle/S}{\partial u}\right]^2\right)^{-3/2}$, where $u{=}\frac{T}{T^*}$. As can be clearly seen,

119
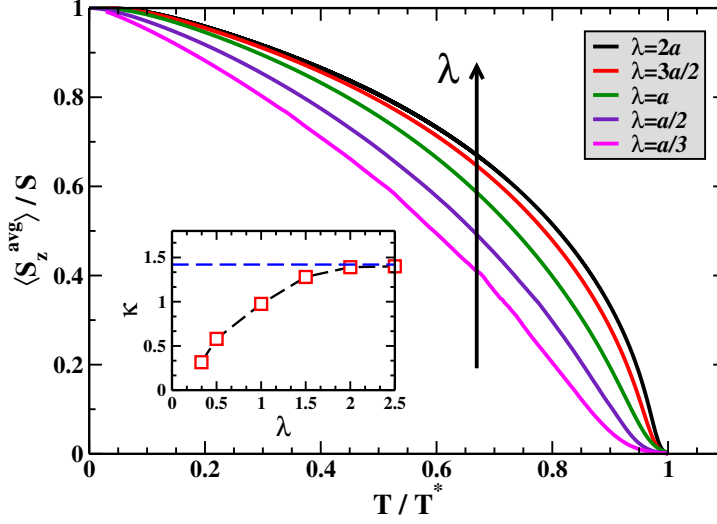
Figure 4.12: Average magnetization as a function of T/T^* for different values of λ, corresponding to the homogeneous case for one configuration. (Inset) Curvature of the $\langle S_z^{avg} \rangle$ curves as a function of λ, calculated at T/T^*=0.5. (Here N=24^3). (From Ref.[155]).

with increase in λ the curvature changes significantly, increasing by almost a factor of five from λ=$a/3$ to λ=$2a$. For $\lambda \geq 2a$, one sees that κ has already saturated and the magnetization has a standard Brillouin shape. This implies that $\lambda \geq 2a$ corresponds to the long range coupling regime. It is already known that the nature and extent of the magnetic interactions in these materials play a vital role in determining the critical temperatures. Here it becomes evident that the range of the interactions also have an important contribution in the spontaneous behavior of the magnetization.

In Figure 4.12, we have shown the magnetization for only one configuration in a homogeneously diluted system. However, we know that for these diluted materials disorder plays an important role and the properties can be sensitive to the random impurity configurations. Hence it would be worth observing the effects of disorder configurations on the nature of the magnetization. Figure 4.13 shows the average magnetization calculated for 25
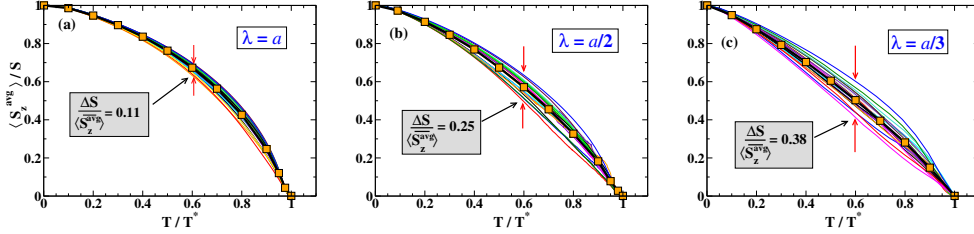
Figure 4.13: Average magnetization for the homogeneous case calculated for 25 configurations, for (a)$\lambda=a$, (b)$\lambda=a/2$, and (c)$\lambda=a/3$. The thick black lines with symbols indicate the configuration averaged magnetization. $\frac{\Delta S}{\langle S_z^{avg}\rangle}$ is a measure of the fluctuation at T/T^*=0.6. (Here N=24^3). (From Ref.[155]).

configurations of disorder corresponding to three different values of λ. We have also calculated $\frac{\Delta S}{\langle S_z^{avg}\rangle}$, which gives a measure of the fluctuations of the extremal magnetization curves from the configuration averaged one ($\langle \overline{S_z^{avg}}\rangle$), at the particular value of T/T^*=0.6. For $\lambda=a$ (Figure 4.13(a)), we observe that the spontaneous magnetization is weakly sensitive to the disorder configurations, the overall shape of the curves is unchanged. $\frac{\Delta S}{\langle S_z^{avg}\rangle}$ is found to vary within 10% of the configuration averaged magnetization. For $\lambda=2a$ (not shown here), these fluctuations were found to be even smaller, varying within less than 5%. For the short ranged couplings, $\lambda=a/2$, the magnetization curves are still convex but the fluctuations are stronger now. $\frac{\Delta S}{\langle S_z^{avg}\rangle}$ is more than doubled as compared to the intermediate range of $\lambda=a$. As can be seen from Figure 4.13(b), some of the curves have a regular convex behavior while some are more linear in nature. Now on further reducing λ (Figure 4.13(c)), the deviations become even stronger, and a significant number of configurations exhibit a clear linear temperature dependence. The fluctuation at T/T^*=0.6 increases by almost a factor four, compared to the case of $\lambda=a$. Even, in some cases, the magnetization profiles are slightly concave toward the high temperature. It should be noted that the more linear or concave magnetization curves correspond to relatively high T_C's. This figure clearly shows that the disorder effects are significantly enhanced in the case of short-ranged interactions. The primary reason is that the probability to find

121

regions of weakly interacting impurities increases significantly for the case of short-ranged interactions. This is the case in most of the DMSs, where a non-trivial behavior of the magnetization is observed. From Figure 4.13 one can also see that the configuration averaged magnetizations are similar in nature to the single configuration magnetization, for the corresponding values of λ, shown in Figure 4.12.

4.3.3 Effects of inhomogeneities

So far we have only considered homogeneously diluted systems assuming a fully random distribution of the impurities. Now we move to the case of clustered magnetic defects, which is the primary objective of our study. As stated earlier, the inhomogeneities considered here are in the form of nanoscale spherical clusters of radii $r_0=2a$, and the concentration inside each cluster is fixed at $x_{in}=0.8$. Figure 4.14 shows for $\lambda=a$, the average magnetization of the whole system, $\langle S_z^{tot} \rangle$, as a function of T/T^*, for four different concentrations of nanospheres, $x_{ns}=1\%$, 3\%, 5\%, and 7\%. In addition, we have also shown the average magnetization inside and outside the clusters denoted by $\langle S_z^{in} \rangle$ and $\langle S_z^{out} \rangle$, respectively. The curves shown here correspond to a single configuration of disorder, the variation with disorder configurations will be discussed later. We immediately observe that in the presence of inhomogeneities the spontaneous magnetization has a non-trivial behavior and exhibits a drastically different nature when compared to the homogeneous case (Figure 4.12). This can be clearly seen even for the lowest concentration of nanospheres. For $x_{ns}=0.01$, for which 11\% of the total impurities are inside the nanospheres, $\langle S_z^{tot} \rangle$ decreases rapidly till about $T/T^*{\sim}0.5$, then it becomes concave and decays slowly toward the higher temperatures. By gradually increasing the concentration of the nanospheres, an interesting change in the average magnetization behavior is observed. For $x_{ns}=3\%$ ($P_N=0.34$), $\langle S_z^{tot} \rangle$ falls off less sharply at low temperature, for 5\% it is almost linear over the entire temperature range, and for 7\% it becomes more convex. Thus a crossover in the curvature of $\langle S_z^{tot} \rangle$ appears at $x_{ns}{\approx}0.05$. On the other hand, $\langle S_z^{in} \rangle$ exhibits a clear convex nature which does not change
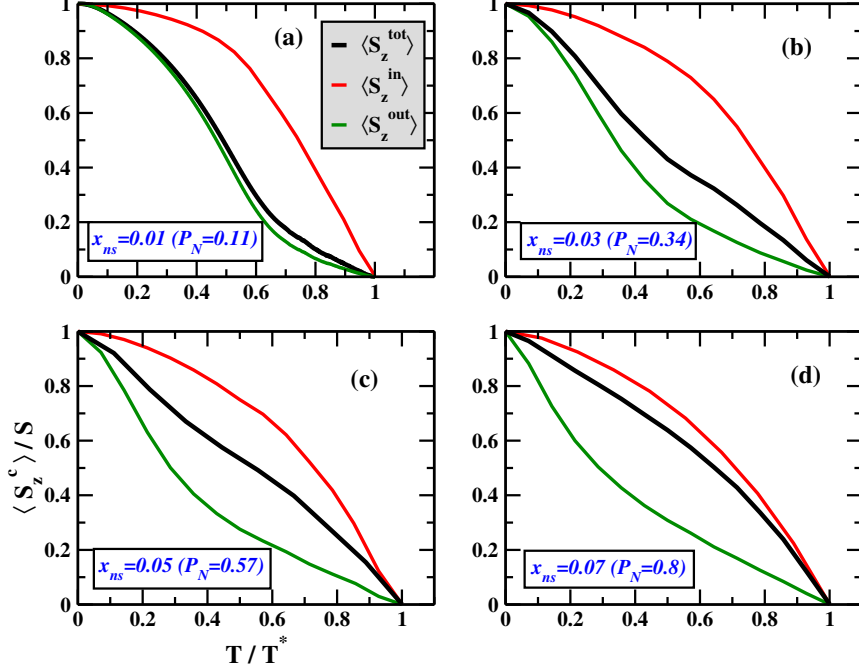
Figure 4.14: $\langle S_z^c \rangle$ stands for the total average magnetization ($\langle S_z^{tot} \rangle$), magnetization inside the nanospheres ($\langle S_z^{in} \rangle$) and outside ($\langle S_z^{out} \rangle$), for four different concentrations of nanospheres (x_{ns}): (a) 0.01, (b) 0.03, (c) 0.05, and (d) 0.07. P_N is the percentage of total impurities contained in the nanospheres. Here $\lambda = a$, $r_0 = 2a$, $x_{in} = 0.8$ and $N = 24^3$. The x-axis is in units of T/T^*. (From Ref.[155]).

with x_{ns}. This indicates that the average magnetization inside the clusters remains almost uniform and is mainly controlled by the intra-cluster couplings. We can clearly see that the inhomogeneities have a very strong effect on the impurities outside the clusters. $\langle S_z^{out} \rangle$ has a very pronounced concave nature which can even be seen for relatively small x_{ns}. The slope at low temperatures becomes steeper with increasing concentration of nanospheres. For example, at $T/T^* \sim 0.3$, $\langle S_z^{out} \rangle$ has a value of 0.85 for $x_{ns} = 0.01$, 0.62 for $x_{ns} = 0.03$, and about 0.4 for $x_{ns} = 0.05$. Similar concave behavior of the temperature dependent magnetization is observed in the case of some insulating DMS materials. However, in most of the cases studied until now clustering

effects have hardly been considered. Note that we have also performed the calculations for $\lambda=2a$ (not shown here). In this extended coupling regime, it was found that the effect of inhomogeneities are very weak. $\langle S_z^{tot} \rangle$, $\langle S_z^{in} \rangle$, and $\langle S_z^{out} \rangle$ exhibit a convex nature and were found to be relatively close to each other.
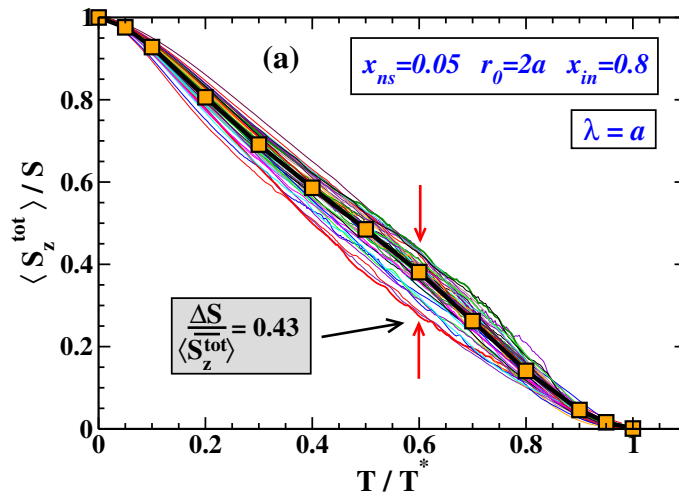
Figure 4.15: Total average magnetization as a function of T/T^* for x_{ns}=0.05 calculated for 50 configurations (thin continuous lines), for $\lambda=a$. The thick black lines with symbols indicate the configuration averaged magnetization $\langle \overline{S_z^{tot}} \rangle$. $\frac{\Delta S}{\langle \overline{S_z^{tot}} \rangle}$ is a measure of the fluctuation at T/T^*=0.6. (Here r_0=2a, x_{in}=0.8 and N=24^3). (From Ref.[155]).

Now, it would also be interesting to observe the effect of the random cluster configurations on the magnetization behavior. For this we consider the particular case of x_{ns}=0.05, and we have shown the average magnetization calculated for 50 configurations of disorder in Figure 4.15, for the case of $\lambda=a$. We see that $\langle S_z^{tot} \rangle$ is very sensitive to the disorder configurations, in the presence of inhomogeneities. The curves have a more or less similar shape over the entire temperature range. However, the deviations from the configuration averaged magnetization are quite large when compared to the corresponding homogeneous case (Figure 4.13(a)). As can be seen, the

fluctuation at $T/T^* = 0.6$ is almost three times to that observed in the homogeneous case. This once again illustrates the importance of disorder in these inhomogeneous systems and a proper treatment of these effects is very crucial. At the same time it should be noted that the configuration averaged magnetization shown here is qualitatively similar to the single configuration magnetization shown in Figure 4.14(c). Moreover the somewhat similar nature of the magnetization curves is also consistent with our T_C calculations in the previous section, where we saw that for relatively long ranged couplings the critical temperatures do not vary drastically with the disorder configurations. Note that we have only shown here $\langle S_z^{avg} \rangle$ for different configurations for the ease of visualization, but we would like to remark that $\langle S_z^{in} \rangle$ and $\langle S_z^{out} \rangle$ also show similar sensitivity to the cluster disorder configurations.

As we have seen in the case of the Curie temperatures, the relatively short-ranged couplings appeared to be more interesting (Section 4.2.4) in the presence of inhomogeneities. This is also important from the practical point of view, as the exchange couplings in some DMS materials are effectively short-ranged in nature. Hence it would be interesting to analyze the effects of this kind of interaction on the magnetization behavior in inhomogeneous systems. In Figure 4.16 we show $\langle S_z^{tot} \rangle$, $\langle S_z^{in} \rangle$, and $\langle S_z^{out} \rangle$ as a function of T/T^*, for four different concentrations of nanospheres, in the case of relatively short-ranged couplings, namely $\lambda = a/2$. To start with, we first discuss the results for a single configuration of disorder. For the lowest x_{ns} (Figure 4.16(a)), the behavior of $\langle S_z^{tot} \rangle$ is almost similar to that observed in the case of $\lambda = a$ (Figure 4.14(a)). But on increasing x_{ns} further (Figure 4.16(b)), we immediately observe that $\langle S_z^{tot} \rangle$ decreases much more rapidly at lower temperatures followed by a slow decay toward the high temperatures. Also, in Figures 4.16 (c) and (d), an inflection appears in $\langle S_z^{tot} \rangle$ around $T/T^* \sim 0.6$. In this case $\langle S_z^{in} \rangle$ too exhibits a non-trivial behavior for all values of x_{ns}, which is unlike the case of $\lambda = a$. For example, for $x_{ns} = 0.05$ (Figure 4.16(c)), there is a shoulder-like feature in $\langle S_z^{in} \rangle$ around $T/T^* \sim 0.05$, which is absent for $\lambda = a$ (Figure 4.14(a)). Thus unlike the case of $\lambda = a$, where the intra-cluster couplings dominate, there are other relevant couplings, like the inter-cluster ones and those between the cluster impurities and bulk impurities, which
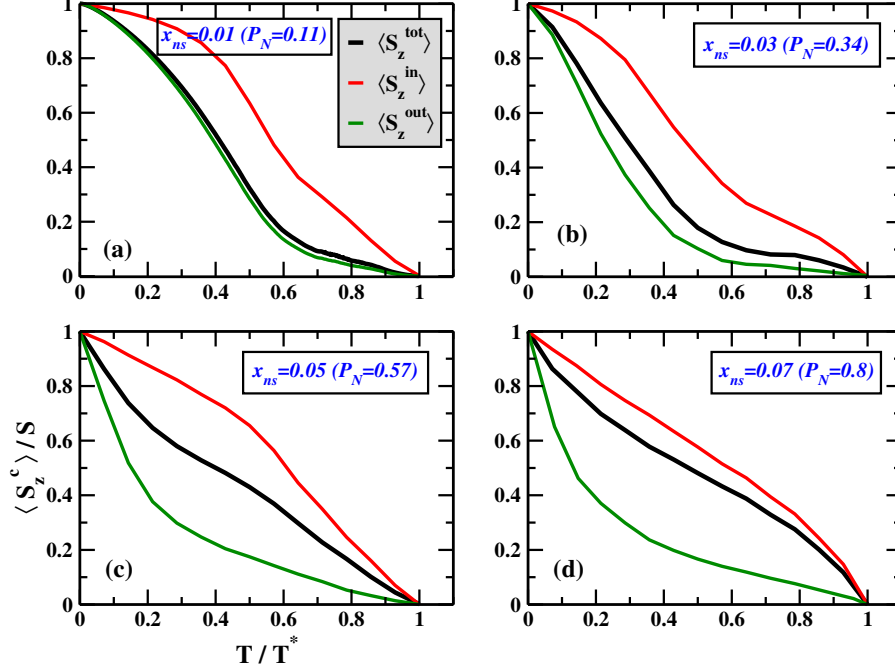
Figure 4.16: $\langle S_z^c \rangle$ stands for the total average magnetization ($\langle S_z^{tot} \rangle$), magnetization inside the nanospheres ($\langle S_z^{in} \rangle$) and outside ($\langle S_z^{out} \rangle$), for four different concentrations of nanospheres (x_{ns}): (a) 0.01, (b) 0.03, (c) 0.05, and (d) 0.07. P_N is the percentage of total impurities contained in the nanospheres. Here $\lambda = a/2$, $r_0 = 2a$, $x_{in} = 0.8$ and $N = 24^3$. The x-axis is in units of T/T^*. (From Ref.[155]).

come into play. On the other hand, the $\langle S_z^{out} \rangle$ curves are typically concave for all considered x_{ns}, and exhibit a long tail toward the higher temperatures. They exhibit a sharp fall-off at low temperatures with increasing x_{ns}. At $T/T^* \sim 0.2$, for $x_{ns} = 0.01$, the value of $\langle S_z^{out} \rangle$ is about 0.8 which falls rapidly to almost 0.3 for $x_{ns} = 0.05$. With increasing x_{ns}, the concentration of impurities outside the clusters gradually decreases, leading to an increase of the typical distance between them. Consequently the impurities outside interact more weakly with each other and this explains the sharp fall-off in $\langle S_z^{out} \rangle$ at lower temperatures.

Now to study the magnetization for different configurations, in Figure
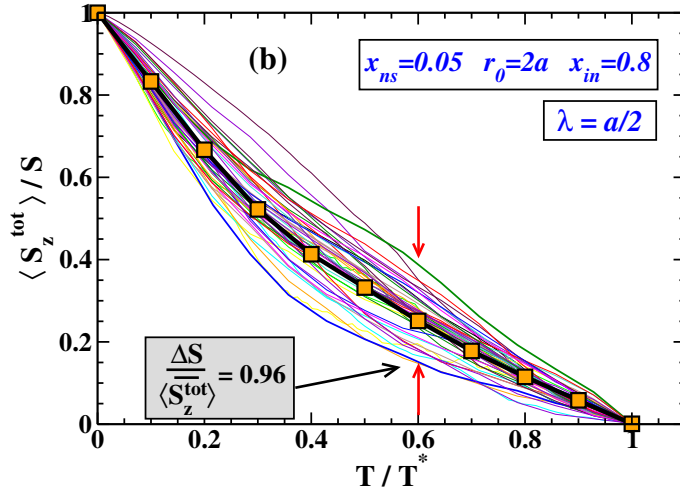
Figure 4.17: Total average magnetization as a function of T/T^* for x_{ns}=0.05 calculated for 50 configurations (thin continuous lines), for $\lambda=a/2$. The thick black lines with symbols indicate the configuration averaged magnetization $\langle\overline{S_z^{tot}}\rangle$. $\frac{\Delta S}{\langle\overline{S_z^{tot}}\rangle}$ is a measure of the fluctuation at T/T^*=0.6. (Here r_0=2a, x_{in}=0.8 and N=24³). (From Ref.[155]).

4.17 we have shown the average magnetization calculated for 50 disorder configurations for the particular case of x_{ns}=0.05, corresponding to $\lambda=a/2$. In contrast to the case of $\lambda=a$ (Figure 4.15), we observe a drastic variation in the magnetization curves for different configurations which reflects the strong sensitivity of these inhomogeneous systems to disorder. For example, the fluctuation at T/T^*=0.6 is found to increase by more than a factor of four compared to that for $\lambda=a$. Also the fluctuations from the configuration averaged magnetization are significantly large, over the entire temperature range, when compared to the corresponding homogeneous case for $\lambda=a/2$ (Figure 4.13(b)). This increase in fluctuation can be seen to be more than five times at T/T^*=0.6. Some of the magnetization curves are concave in nature, while some exhibit a more linear behavior and a few of them even show a convex-like nature toward the higher temperatures for $T/T^*\geq0.6$. It is important to remind here that in systems with effective short-range exchange

127

interactions the typical separations between the clusters play a decisive role, which we have already seen in the previous section concerning the Curie temperatures. In this context it should be noted that the more concave-like curves shown here correspond to higher critical temperatures, while the more linear or convex-like ones coincide with the low T_C's.

4.3.4 Surface imaging of local magnetizations

On analyzing the temperature dependent magnetization, in the presence of inhomogeneities, we have found very interesting and non-trivial behavior in the nature of the magnetization curves which show strong deviations from those of the homogeneous case. However, so far we have only studied the average magnetization of the system which actually depends on the local magnetizations, S_z^i's, at each impurity site. At this point, it would be worthwhile to study the nature of these local magnetizations which might help in providing a better understanding of the observed anomalous magnetization behavior.

The homogeneous case

To begin with, we first focus on the homogeneously diluted systems for fully random distribution of impurities. Figure 4.18 shows the snapshots of the local magnetizations in a 2D-plane corresponding to two different values of λ. The top panel in the figure corresponds to the case of $\lambda=a$, while the bottom panel represents the case of $\lambda=a/2$. The distributions are plotted at three intermediate temperatures T_1, T_2, and T_3 (shown from left to right in the figure), which correspond to the situation when $\langle S_z^{avg} \rangle$=0.75S, 0.4S, and 0.1S respectively. The results shown here correspond to one and the same configuration of disorder for the two λ's. As we can see from the figure there is hardly any noticeable difference, for the change in the local magnetizations with temperature, between the two cases corresponding to $\lambda=a$ and $\lambda=a/2$. At low temperature the local magnetizations remain relatively large, and a gradual thermal decay is observed with increasing temperatures. For the temperature T_3, which is sufficiently close to the critical temperature, we see
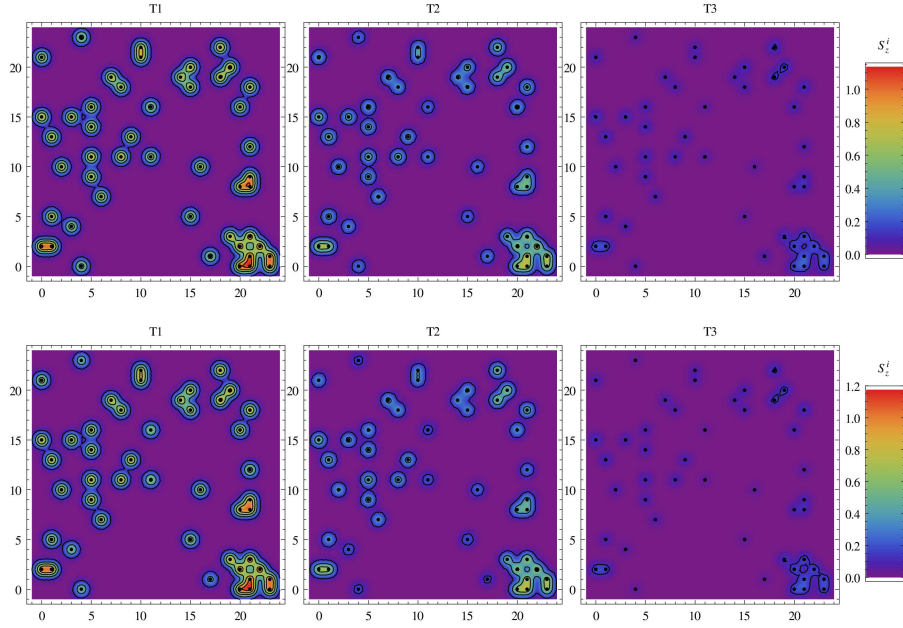
Figure 4.18: Snapshots of S_z^i's corresponding to the homogeneous case. The top (bottom) panels correspond to $\lambda=a$ ($\lambda=a/2$). From L-R: T_1, T_2, and T_3 denote the temperatures when $\langle S_z^{avg} \rangle$=0.75$S$, 0.4$S$ and 0.1S respectively. (Here L=24). (From Ref.[155])

that the local magnetizations at each site are very small, which is as expected. However, on taking a closer look at the figure, we notice that the impurities which are relatively close to each other tend to have a higher magnetization at low temperatures compared to the impurities far away. This is due to the fact that the closer the impurities are, the stronger the exchange interactions, as they are exponentially decaying with the distance between the impurities. The local magnetizations corresponding to the two different λ's appear to be almost similar in behavior, and this seems insufficient to account for the observed different natures of the average magnetization for $\lambda=a$ and $\lambda=a/2$ (Figure 4.12). However, it should be noted that the distributions shown here correspond to just one particular plane of the system which typically contains only a small fraction, typically 5% in this case, of the total impurities in the system. The average magnetization, on the other hand, is determined by the local contributions of all the impurities in the system. Nevertheless, it is

useful to have a qualitative idea of the behavior of the local magnetizations in the absence of any impurity correlations.

Inhomogeneous case

Now moving to the case of the inhomogeneous systems, Figure 4.19 shows the local magnetizations in a 2D-plane corresponding to the particular case of x_{ns}=0.05, for relatively long ranged couplings ($\lambda=a$). This corresponds to the case of the average magnetization shown in Figure 4.14(c). The snapshots are taken for three different temperatures, T_1, T_2, and T_3, similar to what is shown in the previous figure. We choose the plane in a way such that it contains the maximum number of clusters for this particular configuration. The impurity clusters can be clearly identified from the impurities outside as can be seen in the figure. At low temperature (T_1), we see that the local magnetizations for the impurities inside the nanospheres are relatively higher than the ones outside, by almost a factor three in some cases. (The color bar in the figure indicates the relative intensities of the local magnetizations). For an intermediate temperature T_2, the magnetization for the impurities outside gradually weakens but the cluster impurities still tend to retain relatively higher magnetization values, due to the strong intra nanosphere interactions. Now at a relatively high temperature T_3, which corresponds to the situation when $\langle S_z^{avg} \rangle$=0.1$S$, most of the impurities outside the clusters are found to lose their magnetization almost entirely. However, even then, inside the nanospheres the local magnetizations are comparatively high, with some clusters retaining higher values than the other ones. This may be due to the fact that some of the clusters experience the effects of the cluster impurities coming from the other planes, above or below the particular plane shown here, and hence they are strongly coupled compared to the impurities within the other clusters which may not be experiencing similar effects. This also shows that the strong intra cluster couplings dominate the magnetic ordering at relatively high temperatures, which controls the spontaneous magnetization behavior in these inhomogeneous systems. The impurities outside, on the other hand, are weakly coupled with each other and they tend to lose

their magnetizations much faster with increasing temperatures. This is reflected in the sharp fall off of $\langle S_z^{out} \rangle$, shown in Figure 4.14(c). Thus we see that the behavior of the local magnetizations is consistent with our results for the average magnetization, which we have discussed in Section 4.3.3.

Figure 4.19: Snapshots of S_z^i's corresponding to the case of x_{ns}=0.05 for λ=a. From L-R: T_1, T_2, and T_3 denote the temperatures when $\langle S_z^{avg} \rangle$=0.75$S$, 0.4$S$ and 0.1S respectively. (Here r_0=2a, x_{in}=0.8 and L=24). (From Ref.[155]).

Now in Figure 4.20 we show the local magnetizations corresponding to the case of relatively short ranged couplings, λ=$a/2$, with the other parameters being the same as that of Figure 4.19. We observe a somewhat similar behavior of the local magnetizations as was seen for the case of λ=a. For the low temperature T_1, the impurities within the nanospheres are found to exhibit higher magnetization values compared to the impurities outside. With increase in temperature, the local magnetization for the impurities outside is found to decay rather fast while the ones inside the clusters still tend to retain relatively high magnetizations. However, the distribution corresponding to the situation at the high temperature T_3, appears to be interesting. At this temperature, as can be seen from the figure, it is not only the impurities outside the clusters which carry very small magnetization but also the impurities belonging to one of the clusters (seen in the bottom left corner of the snapshots) appear to lose their magnetization almost entirely. This is unlike the case of λ=a, where most of the impurities inside the clusters were always found to carry a relatively higher value compared to the ones outside even at the high temperature T_3. Now, this may be attributed to the
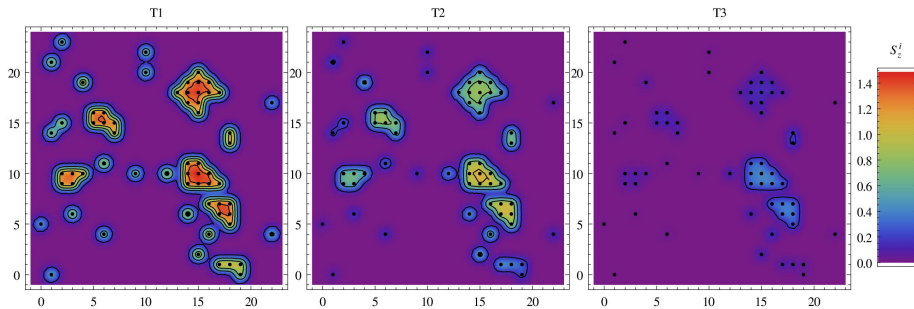
131
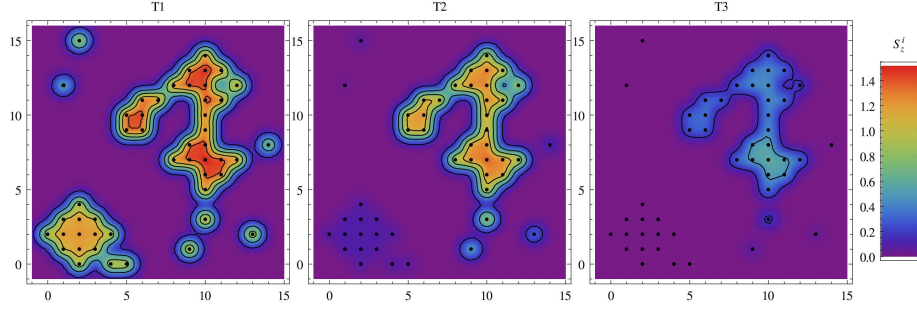
Figure 4.20: Snapshots of S_z^i's corresponding to the case of x_{ns}=0.05 for λ=$a/2$. From L-R: T_1, T_2, and T_3 denote the temperatures when $\langle S_z^{avg} \rangle$=0.75$S$, 0.4$S$ and 0.1S respectively. (Here r_0=2a, x_{in}=0.8 and L=16). (From Ref.[155]).

fact that since the effective exchange interactions are of short-range in this case, the impurities outside as well as the impurities within some particular cluster, which may be far away from the other cluster impurities, are weakly interacting. This results in a rapid decay of their respective local magnetizations, in comparison to the other clusters which are relatively close to each other and which tend to retain higher values of local magnetizations due to the strong cluster interactions. The distributions shown here are consistent with the average magnetization behavior for the corresponding case shown in Figure 4.16(c). For higher temperatures, we can see that it is only some of the impurities within the nanospheres with strong interactions which seem to carry most of the magnetization. Thus for relatively high concentration of nanospheres it is the strong intra cluster couplings which tend to dominate the spontaneous magnetization behavior and this results in a slow decay of the average magnetization close to the critical temperatures (Figure 4.16(c)). On the other hand, the fast and strong decay of the local magnetizations for the impurities outside the clusters could explain the rapid initial fall off observed in $\langle S_z^{out} \rangle$ at relatively low temperatures in Figure 4.16(c).

4.3.5 Some general remarks

We can briefly make the following remarks from the above results. The behavior of the local magnetizations appears to be interesting from a fundamental perspective. It helps to furnish an overall better understanding, though qualitative in nature, of the anomalous magnetization behavior in these inhomogeneous systems. The local magnetizations provide direct insight into the real physical intricacies of the system, which in turn are responsible for the average magnetization response. The range of the effective exchange interactions is found to play an important role in determining the spontaneous magnetization. Although we have shown here the local magnetizations corresponding to one particular value of x_{ns}, it can be said that the same corresponding to the other x_{ns} should be qualitatively similar in nature and consistent with the respective average magnetization behavior.

Now in all the above calculations for the inhomogeneous systems, we have mainly focused on the nanoclusters of radii $r_0=2a$ and a fixed $x_{in}=0.8$. It would be equally interesting to perform similar calculations for nanospheres of other radii and with different concentrations of impurities inside. We certainly expect similar unconventional behavior of the spontaneous magnetizations. However, the quantitative nature of this magnetization response can only be confirmed by further detailed calculations.

4.4 Spin-wave excitations in inhomogeneous systems

After analyzing the effects of nanoscale inhomogeneities on the Curie temperatures and the spontaneous magnetization behavior in the preceding sections, we focus here on the magnetic spin excitations in the inhomogeneous diluted systems. As seen before, in the case of homogeneously diluted systems, a detailed investigation of the magnon excitation spectrum can provide valuable insight into the role and importance of disorder in these diluted magnetic systems. The emerging physical phenomena can become even more interesting and complex in the presence of inhomogeneities. However, until now, most of

the studies, experimental as well as theoretical, dealing with inhomogeneous systems have focused either on the Curie temperatures or on the spontaneous magnetization behavior. The effects of impurity clustering on the spin-wave excitations can be scarcely found in the literature. A meticulous study of these excitations might reveal further interesting properties of these inhomogeneous systems as well as provide a better understanding of the interplay between several physical parameters. This was the main motivation behind the study we are going to discuss here.

In this section, we will present a detailed study of the magnon DOS, the magnon spectral function and the spin-stiffness as a function of the concentration of inhomogeneities. We find interesting and significant variations in these properties when compared to those of the homogeneously diluted cases. A similar method is adopted here, as used in the previous cases (Sections 4.2 and 4.3), considering a simple cubic lattice with periodic boundary conditions. The basic approach is same as before with disorder being treated within the SC-LRPA theory. All the calculations are performed at T=0 K. Once again the inhomogeneities are in the form of nanospheres with radii r_0, which are randomly distributed on the lattice. We work at a fixed concentration of impurities in the system, x=0.07, similar to the previous cases. The notations of the other relevant phenomenological parameters remain consistent with what we have used earlier in this chapter, unless otherwise stated. Finally for the exchange couplings too, we use the same isotropic interactions of the form J_{ij}=J_0 exp(-|$\mathbf{r}$| /λ). We consider here two typical values of λ: (i) λ=a, for relatively long-ranged couplings, and (ii) λ=$a/2$, for short-ranged ones.

4.4.1 Resolved magnon DOS in presence of inhomogeneities

We begin with the calculation of the magnon DOS for the homogeneous case. Figure 4.21 shows the average magnon DOS (ρ_{avg}) as a function of the energy ω, corresponding to the two different values of λ. The system size considered here is L=56, and the disorder averaging is performed for

134
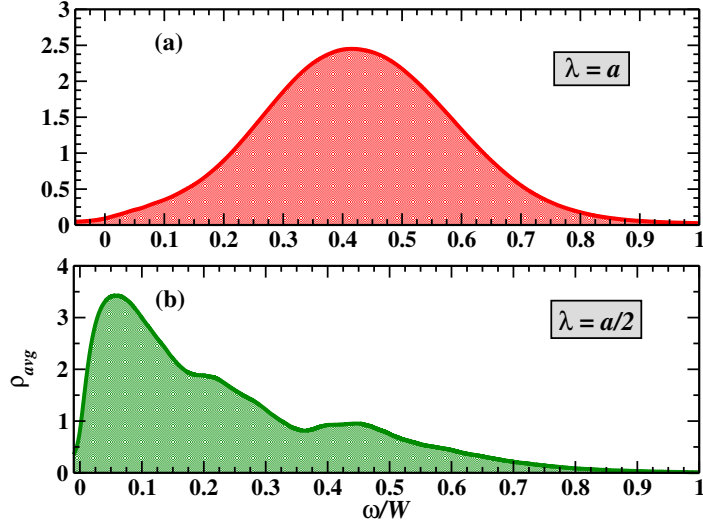
Figure 4.21: Average magnon DOS corresponding to the homogeneous case for (a) $\lambda=a$, and (b) $\lambda=a/2$. The average concentration is $x=0.07$. The x axis is in units of ω/W, where W is the magnon spectrum bandwidth. $W \approx 4J_0$ and $0.8J_0$, for $\lambda=a$ and $a/2$ respectively. The system size is $N=56^3$. (From Ref.[156]).

few hundred configurations. ρ_{avg} is found to exhibit a regular Gaussian-like shape for the case of $\lambda=a$ (Figure 4.21(a)). The broad peak is located at $0.42W$ with a half-width of about $0.36W$ (W is the magnon excitation bandwidth). For longer ranged couplings, ρ_{avg} remains essentially similar to that of $\lambda = a$. On the other hand, for short-ranged couplings ($\lambda = a/2$), ρ_{avg} has a more irregular and richer structure (Figure 4.21(b)). The peak in ρ_{avg} is now located at much lower energy, $0.06W$, and a clear long tail extending toward the high energies with multiple shoulders appears. These additional features result from clusters of impurities weakly coupled to the rest of the system. These shoulders become even more pronounced for shorter ranged interactions. It is interesting to note that a somewhat similar kind of magnon DOS was obtained in the case of (Ga,Mn)As (see Figure 3.11). However, it is not exactly the same, since in that case realistic couplings, calculated within the V-J model, were used to calculate the DOS. Although the magnon DOS

shown here do not provide enough quantitative information, they will be useful in the discussions to follow.
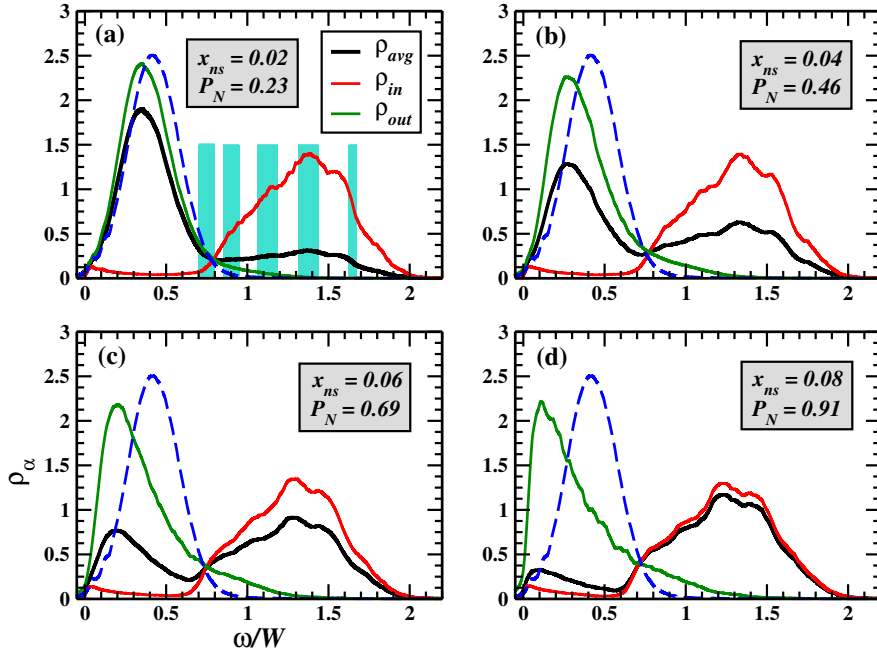
Figure 4.22: ρ_α denotes the average magnon DOS (ρ_{avg}), local magnon DOS inside (ρ_{in}), and outside the nanospheres (ρ_{out}), for four different x_{ns}. P_N is the percentage of total impurities inside the nanospheres. The shaded regions in (a) correspond to the calculated eigenmodes of a single isolated nanosphere. The parameters are $\lambda=a$, $r_0=2a$, and $x_{in}=0.8$. The x axis is in units of ω/W, where $W \approx 4J_0$ is homogeneous magnon bandwidth. The blue dashed curve indicates the homogeneous ρ_{avg} from Figure 4.21(a). (From Ref.[156]).

Now moving on to the magnon DOS in the inhomogeneous case, we consider the case of nanospheres with fixed radii $r_0=2a$ and $x_{in}=0.8$. In Figure 4.22 we have plotted, in addition to ρ_{avg}, the local magnon DOS inside the nanospheres (ρ_{in}) as well as the local DOS outside (ρ_{out}) as a function of the energy, for four different concentrations of nanospheres, corresponding to $\lambda=a$. The respective average DOS for the homogeneous case is also shown in the figures (blue dashed curves) to facilitate comparison. We should specify

here that ρ_{in} denotes the local magnon DOS averaged over all the impurities contained within the nanospheres, and similarly ρ_{out} denotes the local magnon DOS averaged over all impurities outside. Let us first focus on ρ_{avg}. From Figure 4.22(a), we immediately notice that a relatively small concentration of inhomogeneities ($x_{ns}{\sim}0.02$) causes a significant change in the magnon DOS. Indeed, in comparison to the homogeneous case, the excitations spectrum bandwidth is now doubled, and ρ_{avg} has a bimodal structure, with a broader peak at higher energies. With increasing x_{ns}, we observe a gradual transfer of weight from the low to high energy peak. The low energy peak shifts to smaller energies which is consistent with the decrease in the concentration of impurities outside the nanospheres. In order to have a better understanding of the features seen in ρ_{avg}, we now analyze ρ_{in} and ρ_{out}. We observe that ρ_{in} remains unchanged in all cases and exhibit a very small weight from 0 to $0.7W$. Thus the high energy peak seen in ρ_{avg} can clearly be attributed to the nanocluster modes. A careful analysis of a single isolated cluster reveals that the first non-zero eigenmodes are located at $0.7W$, which explains the very small weight in ρ_{in} below this value. Note that in Figure 4.22(a), the shaded regions correspond to the discrete spectrum of an isolated single nanosphere, which is calculated over a few hundred configurations (random position of the impurities inside the nanosphere). The weak variation of ρ_{in} with respect to x_{ns}, indicates that the disappearance of the discreteness in ρ_{in} (as seen in the isolated nanosphere spectrum) results mainly from the interactions between the cluster impurities and those outside. The above discussion of ρ_{avg} and ρ_{in} explains naturally the behavior of ρ_{out}. In the case of more extended couplings, it is expected that (i) ρ_{avg} loses progressively the bimodal nature, (ii) the pseudo-gap in ρ_{in} at low energies is filled gradually, and (iii) the second peak in ρ_{in} becomes narrower and shifts to higher energies with respect to the spectrum of a single isolated cluster.

In the next figure, Figure 4.23, we show ρ_{avg}, ρ_{in}, and ρ_{out} for four different values of x_{ns}, but this now corresponds to the case of the relatively short ranged interactions, $\lambda{=}a/2$. The other parameters being the same as used in the previous case. In this case, we observe even more interesting changes in the average DOS as compared to the homogeneously diluted case. The
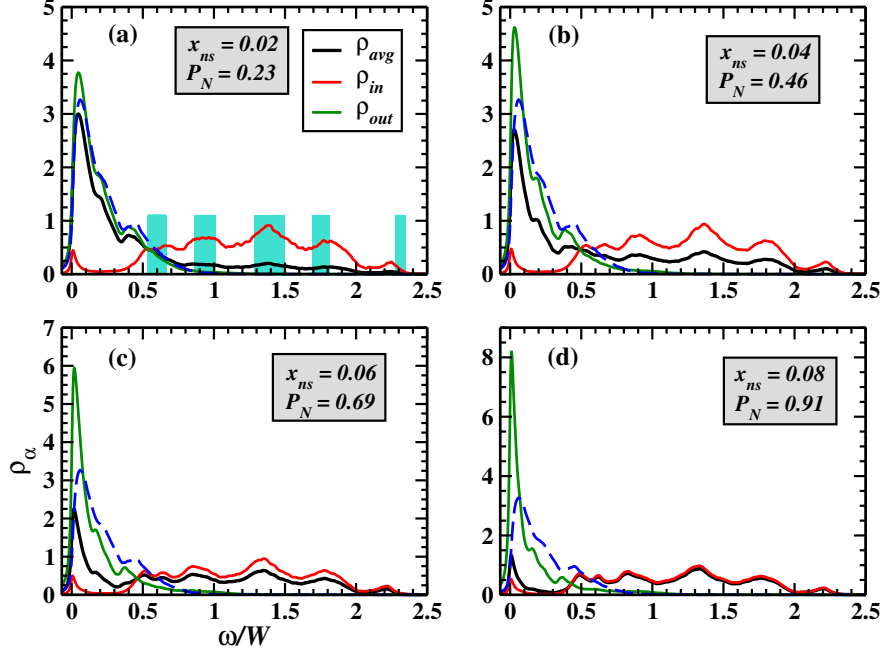
Figure 4.23: ρ_{avg}, ρ_{in}, and ρ_{out} for $\lambda=a/2$, for four different x_{ns}. The shaded regions in (a) correspond to the calculated eigenmodes of a single isolated nanosphere. The other parameters being same as in Figure 4.22. The homogeneous magnon bandwidth is $W\approx0.8J_0$. The blue dashed curve indicates the homogeneous ρ_{avg} from Figure 4.21(b). (From Ref.[156]).

magnon bandwidth increases by 250% with respect to that of the homogeneous system. As seen before, we observe a clear transfer of weight in ρ_{avg}, from the low to higher energies with increasing x_{ns}. In contrast to the bimodal nature observed for $\lambda=a$, ρ_{avg} now exhibits a long wavy tail, extending toward higher energies. ρ_{in} shows (i) a clear multiple peak structure now, (ii) is independent of x_{ns}, and (iii) a well defined gap of approximately $0.5W$ is observed. The reasons for the appearance of these multiple peaks in ρ_{in} are the enhanced discreteness (larger sub-gaps) of the eigenmodes of the single isolated nanosphere and the reduced interactions of the cluster impurities with those outside. Concerning ρ_{out}, besides a shift to lower energies as seen for $\lambda=a$, we now observe that the peak becomes narrower with increase in

x_{ns}. (The latter feature was absent for the longer ranged couplings). The reason for this is with increasing x_{ns}, the concentration of impurities outside decreases and the effective interactions between them become weaker. This effect will be even more pronounced for shorter ranged couplings. Even though the couplings are comparable, drastic changes between Figures 4.22 and 4.23, shows that $\lambda=a$ corresponds to the intermediate range couplings and $\lambda=a/2$ definitely to the short range regime. Similar kind of dramatic effects have also been reported on the effects of nanoscale inhomogeneities on critical temperatures[143].

4.4.2   Dynamical magnon spectral function

In this part we will focus on the nature of the magnon spectral function in the presence of inhomogeneities. As seen before, the spectral function can provide valuable insight into the spin excitation spectrum of the system. Now to compare the effects of inhomogeneities, we first calculate the spectral function for the homogeneously diluted case.

In Figure 4.24 we show the average magnon spectral function $\bar{A}(\mathbf{q},\omega)$ as a function of the energy for different values of the momentum $\mathbf{q}$ in the (1 0 0) direction, corresponding to the case of $\lambda=a$. The corresponding homogeneous case for $\lambda=a/2$ is plotted in Figure 4.25. The calculations are performed on a system size of $L=66$ and a systematic average over a few hundred configurations of disorder is done. However, it is found that increasing the number of configurations beyond 50, for this system size, does not affect the results considerably. First in both cases, as q increases the peaks become broader and more asymmetric with a tail extending toward higher energies. Well-defined excitations exist only for relatively small values of the momentum, beyond $q_x a \approx 0.24\pi$ no well-defined magnons exist. However, for $\lambda=a$, the well-defined excitations persist up to energy values of about $0.25W$, whilst for $\lambda=a/2$ the excitations reaches only up to $0.035W$, where W is the λ-dependent magnon spectrum bandwidth. We remind that $W\approx 4J_0$ and $0.8J_0$, for $\lambda=a$ and $a/2$, respectively. These homogeneous spectral functions serve as a standard of comparison to what follows next.

Figure 4.24: Average spectral function $\bar{A}(\mathbf{q}, \omega)$ as a function of the energy in the (1 0 0) direction for different values of q_x, corresponding to the homogeneous case for $\lambda = a$. The energy axis (x-axis) is in units of ω/W. The system size is $N = 66^3$. (The intensity of the peaks have been multiplied by the factors indicated in the parentheses). (From Ref.[156]).

Now coming to the case of the nanoclusters, Figure 4.26 shows the average spectral function $\bar{A}(\mathbf{q}, \omega)$ as a function of the energy in the (1 0 0) direction, corresponding to the case of $\lambda = a$. The results are shown for four different values of x_{ns}: 0.02, 0.04, 0.06, and 0.08. As we increase x_{ns}, there is a broadening in the excitations, accompanied with an increase in asymmetry and a shift toward the lower energies is observed. These effects are already pronounced even for the lowest concentration of nanospheres. For instance, for $q_x a \approx 0.12\pi$, the magnon energies are $0.09W$, $0.075W$, and $0.067W$, for $x_{ns} = 0$, 0.02, and 0.04, respectively. In order to analyze the effects of inhomogeneities on the magnon lifetime for a given $\mathbf{q}$, we define the ratio $R(\mathbf{q}) = \gamma(\mathbf{q})/\omega(\mathbf{q})$, where $\gamma(\mathbf{q})$ is the half-width of the excitations. The excitations are well-defined in character only when $R(\mathbf{q}) < 1$. For the aforesaid q_x, the corresponding $R(\mathbf{q})$'s are 0.2, 0.33, and 0.66, for $x_{ns} = 0$, 0.02, and 0.04, which corresponds to an increase of about 60% and 200% respectively,
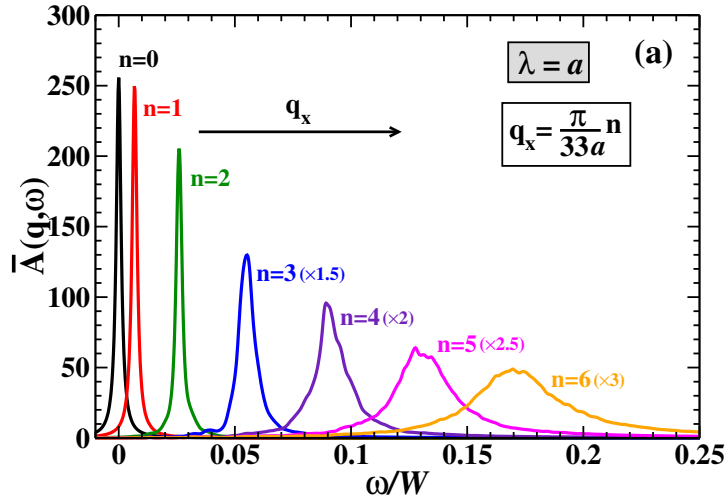
Figure 4.25: Average spectral function $\bar{A}(\mathbf{q}, \omega)$ as a function of the energy in the (1 0 0) direction for different values of q_x, corresponding to the homogeneous case for $\lambda = a/2$. The energy axis (x-axis) is in units of ω/W. The system size is $N = 66^3$. (The intensity of the peaks have been multiplied by the factors indicated in the parentheses). (From Ref.[156]).

compared to the homogeneous case, for these two values of x_{ns}. It is interesting to note that these effects could hardly be anticipated from the magnon DOS results (Fig. 2). In fact the analyses of the DOS suggested that the low energy excitations should be weakly affected by the inhomogeneities. In the following, we discuss the spectral function in the presence of short-ranged interactions, shown in Figure 4.27. As in the previous case, well-defined excitations exist only for small values of the momentum. However, here we find that the shift toward the lower energies is strongly enhanced. If we consider the particular case of $q_x a \approx 0.12\pi$, the magnon energies are shifted by 30% and 60% respectively, for $x_{ns} = 0.02$ and 0.04, with respect to that of the homogeneous case. The $R(\mathbf{q})$'s for this value of q_x are 0.4, 0.8, and 1.3 for $x_{ns} = 0$, 0.02, and 0.04. This indicates that the excitations have dramatically lost their well defined character as compared to the previous case (Figure 4.26). Hence we see that the presence of inhomogeneities can alter
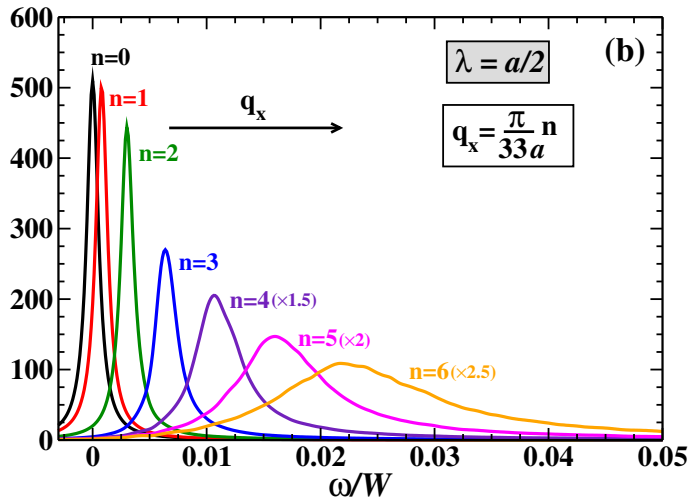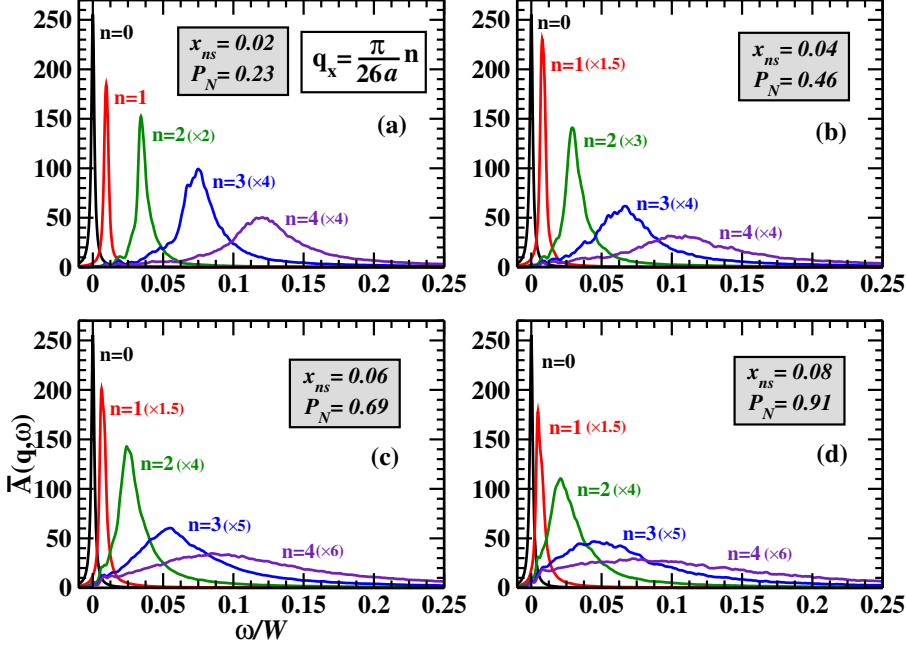
Figure 4.26: Average spectral function $\bar{A}(\mathbf{q}, \omega)$ as a function of the energy in the (1 0 0) direction, for four different x_{ns}. P_N indicates the percentage of total impurities inside the nanospheres. The parameters are $\lambda = a$, $r_0 = 2a$, $x_{in} = 0.8$, and $N = 52^3$. The x axis is in units of ω/W. (The intensity of the peaks have been multiplied by the factors indicated in the parentheses). (From Ref.[156]).

the nature of the spin excitations significantly in these diluted systems. At the same time it should be noted that the spectral functions, in the figures shown here, is plotted only in the (1 0 0) direction. Now it would be interesting to observe the change in the excitation spectrum over the entire Brillouin zone.

Figure 4.28 shows the spectral function in the $(\mathbf{q}, \omega)$ plane, plotted over the entire Brillouin zone, for the homogeneously diluted case. This corresponds to the case of $\lambda = a$. The system size considered here is $L = 44$ and the average over disorder is performed for few hundred configurations. From the figure we see that well-defined excitations only exist almost till half of the
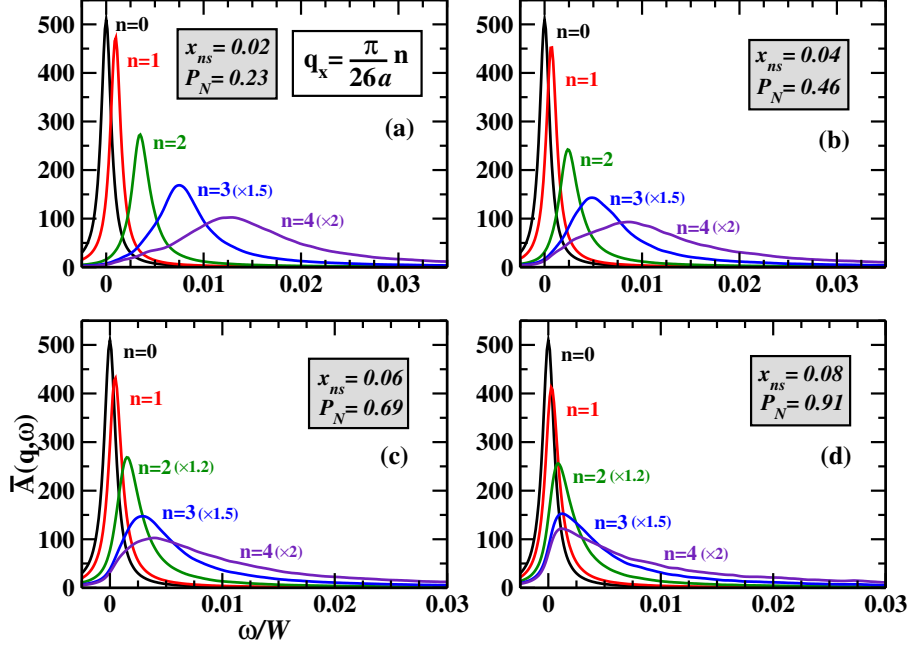
Figure 4.27: Average spectral function $\bar{A}(\mathbf{q}, \omega)$ for the case of $\lambda = a/2$, with the other parameters same as in Figure 4.26. (From Ref.[156]).

first Brillouin zone. The spectrum shows a uniform broadening on moving further away, around an energy value of $1.5J_0$. This is consistent with the $\bar{A}(\mathbf{q}, \omega)$ results shown in Figure 4.24, where more asymmetric peaks were observed for increasing values of $\mathbf{q}$ in the (1 0 0) direction. We also find that the relevant energy range for the magnon excitations is in accordance with the homogeneous magnon DOS results, shown in Figure 4.21(a). Now to analyze the effects of the nanoscale inhomogeneities, we show in Figure 4.29 the corresponding spectral functions in the $(\mathbf{q}, \omega)$ plane, for four different concentrations of nanospheres. We immediately observe that the clusters have a significant impact on the magnon excitation spectrum. For a relatively low x_{ns} (~ 0.02), the effects can be hardly noticed, with well-defined excitations still existing around a restricted region of the first Brillouin zone. However, with increasing concentration of nanospheres, drastic changes accompanied

Figure 4.28: Spectral function $A(\mathbf{q}, \omega)$ in the $(\mathbf{q}, \omega)$ plane, corresponding to the homogeneous case for $\lambda = a$. The energy axis (y-axis) is in units of ω/J_0. (Here $N = 44^3$). (From Ref.[157]).

with the appearance of prominent features in the spectrum are observed. The well-defined excitations are also found to be strongly reduced and the spectrum shows considerable broadening. Some characteristic excitations are found to appear at comparatively higher energies between $3J_0$ and $6J_0$. The intensity of these excitations increases with increasing x_{ns} as can be seen from Figures 4.29(b)-(d). This may be accounted for by the increasing localization of the magnon modes within the nanospheres with increasing cluster concentration. This gives rise to the relatively high energy excitations in the magnon spectrum around the middle of the Brillouin zone. These features also point to the crossover from extended states to localized magnon modes with increase in the clustering phenomenon. We observe, interestingly, a kind of 'gap' appearing in the excitations around energies of $2J_0$, at $x_{ns}=0.06$ and above. This feature is consistent with the very low weight observed in the average magnon DOS around the same energies for the corresponding x_{ns} values (Figure 4.22). Hence we see that the presence of nanoscale impurity

144

Figure 4.29: Spectral function $A(\mathbf{q}, \omega)$ in the $(\mathbf{q}, \omega)$ plane corresponding to $\lambda = a$, for four different x_{ns} : (a) 0.02, (b) 0.04, (c) 0.06, and (d) 0.08. The energy axis (y-axis) is in units of ω/J_0. (Here $r_0 = 2a$, $x_{in} = 0.8$, and $L = 44$). (From Ref.[157]).

clusters can lead to very interesting and new features in the spin excitation spectrum of these diluted magnetic systems.

Now we analyze the same excitation spectrum but in the case of relatively short-ranged couplings, for $\lambda = a/2$, which is found to be more relevant for some realistic materials. First we show the spectral function in the $(\mathbf{q}, \omega)$ plane, corresponding to the homogeneous distribution of impurities, in Figure 4.30. The same system size and number of disorder configurations is used to obtain $A(\mathbf{q}, \omega)$ here, as used in the previous case. We observe a very different behavior, compared to the case of $\lambda = a$ (Figure 4.28). Well-defined excitations can be seen to exist only in a restricted region of the Brillouin zone, around the Γ point [$\mathbf{q} = (0\ 0\ 0)$]. We find a very large and non-uniform broadening of
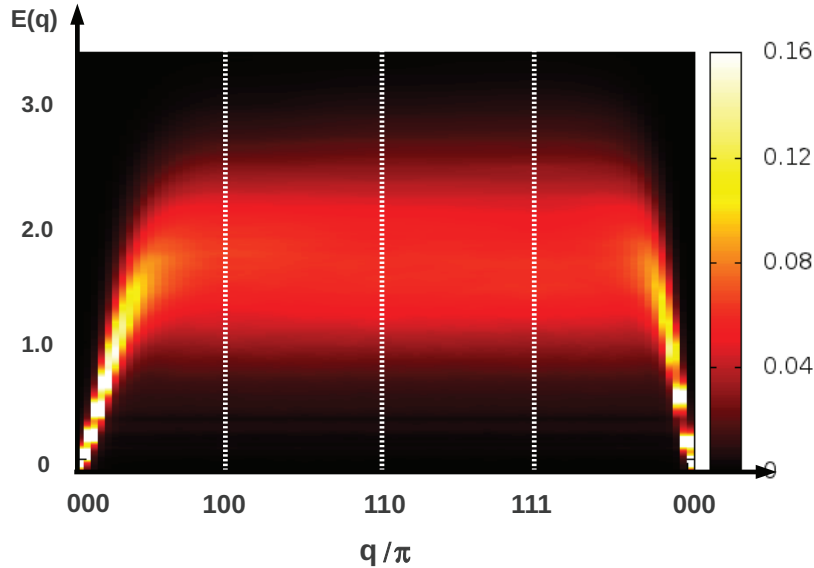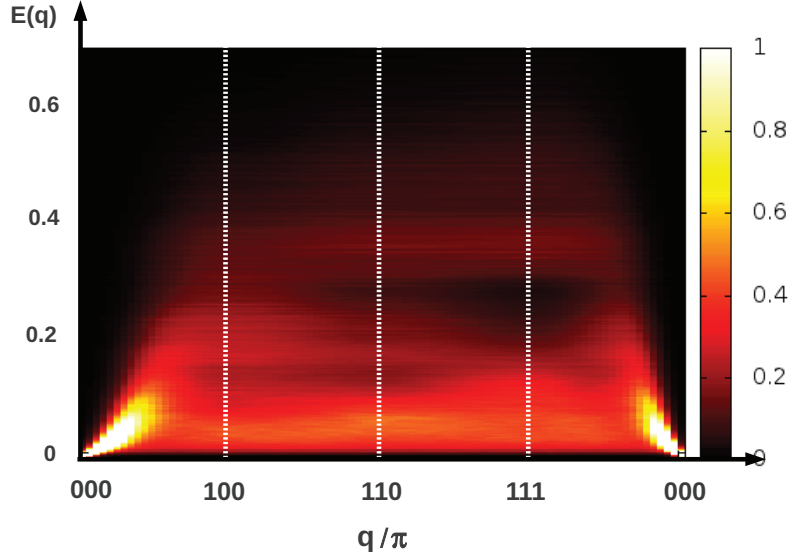
Figure 4.30: Spectral function $A(\mathbf{q}, \omega)$ in the $(\mathbf{q}, \omega)$ plane, corresponding to the homogeneous case for $\lambda = a/2$. The energy axis (y-axis) is in units of ω/J_0. (Here $N = 44^3$). (From Ref.[157]).

the spectrum which indicates that the magnon lifetime is strongly reduced in this case. We also observe low-lying excitations around the center of the Brillouin zone corresponding to low energy values, which is found to be absent in the case of $\lambda = a$. This shows that the effective range of the exchange interactions also plays a significant role in determining the spin dynamics, namely the magnon excitations, in these diluted systems. Now it is interesting to note that the spectral function shown here is very similar to the spectral function obtained for the case of optimally annealed (Ga,Mn)As (see Figure 3.12). Here we work at a fixed concentration of $x=0.07$, which is close to the Mn concentrations used for (Ga,Mn)As. However, as we know, the exchange couplings in (Ga,Mn)As were obtained within the one-band V-J model. Nevertheless, the similar nature of the spectral function justifies once again the choice of our generalized couplings.

Now moving to the case of inhomogeneities, Figure 4.31 shows the spec-
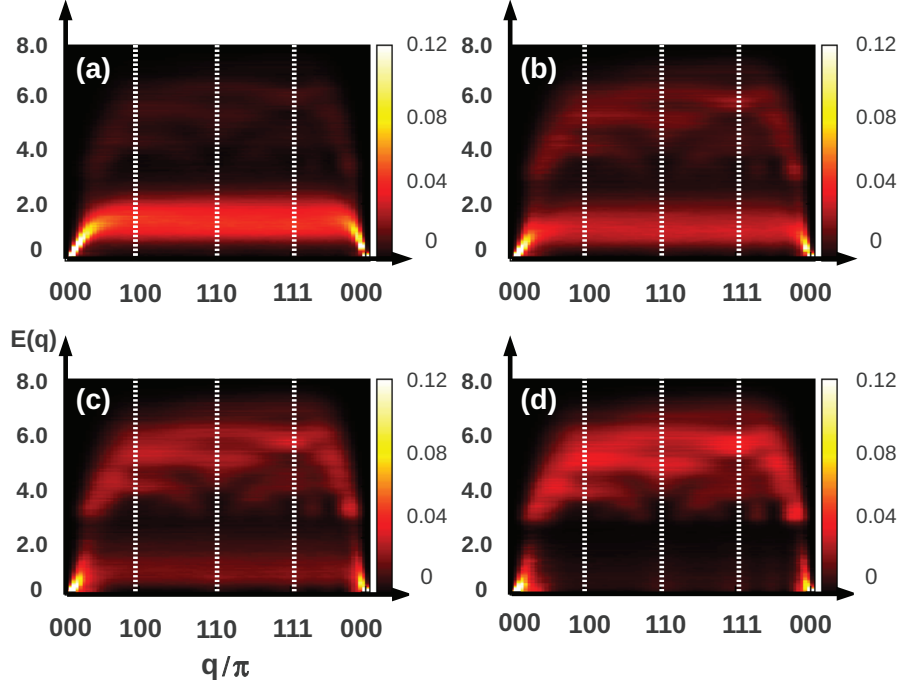
146
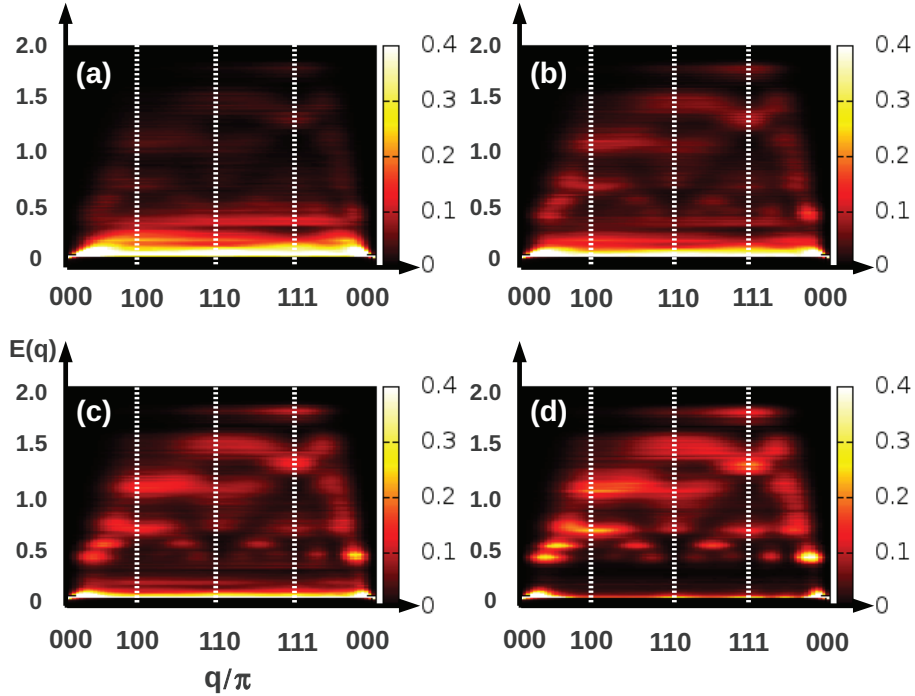
Figure 4.31: Spectral function $A(\mathbf{q}, \omega)$ in the $(\mathbf{q}, \omega)$ plane corresponding to $\lambda = a/2$, for four different x_{ns} : (a) 0.02, (b) 0.04, (c) 0.06, and (d) 0.08. The energy axis (y-axis) is in units of ω/J_0. (Here $r_0 = 2a$, $x_{in} = 0.8$, and $L = 44$). (From Ref.[157]).

tral function in the $(\mathbf{q}, \omega)$ plane, corresponding to the case of $\lambda = a/2$, for four different values of x_{ns}. Here too we observe interesting and strong deviations in the excitation spectra as compared to the homogeneous case (Figure 4.30). The effects of the inhomogeneities are relatively feeble for a small concentration of nanospheres ($x_{ns} \sim 0.02$). Some excitations of low intensity can be seen to appear at relatively higher energies for $x_{ns} = 0.04$. These excitations become more and more conspicuous with increasing values of x_{ns}, as can be seen from Figures 4.31(c) and (d). Well-defined excitations, close to the Γ point, also cease to exist with increasing x_{ns} and we observe a full suppression of the low lying excitations at high x_{ns}. This may be again due to the localization of the magnons inside the clusters, which is enhanced with the

increase in the concentration of nanospheres. The magnon excitations in this case exhibit a qualitatively different nature from what is observed in the case for $\lambda=a$ (Figure 4.29). More localized excitations are found to exist over the entire Brillouin zone, for both relatively low and high energy values, which is unlike the case of $\lambda=a$. The occurrence of these characteristic excitations, typically between energy values of 0.5 and $2J_0$, is found to be consistent with the multiple peak structure of the magnon DOS observed in Figure 4.23. The results for the spin excitation spectrum obtained here, within our simple model approach, could be further substantiated by detailed experimental studies on these inhomogeneous diluted systems. Inelastic neutron scattering measurements have proved to be an efficient tool in this context.

4.4.3   Spin-wave stiffness suppression by inhomogeneities

 After analyzing the magnon DOS and the spin excitation spectrum, it would be interesting to observe the effects of inhomogeneities on the spin-stiffness in these materials. We have already seen (Section 4.2) that in the presence of these nanoscale inhomogeneities the Curie temperatures can be enhanced drastically, especially in systems with short-ranged interactions. However, one can not say instinctively what to expect in the case of the spin-stiffness. Experimental studies measuring the spin-stiffness in inhomogeneous systems are also lacking. We have calculated here the spin-stiffness in the presence of nanoclusters, as a function of the concentration of inhomogeneities. Now in order to gauge the effects of the inhomogeneities, we show here the normalized spin-stiffness coefficient $D_n=D^{inh}/D^{hom}$, where D^{inh} denotes the spin-stiffness of the inhomogeneous system, and D^{hom} that of the homogeneously diluted system. The values of the spin-stiffness D^{hom} are found to be 2.9 J_0 and 0.07 J_0, for $\lambda=a$ and $a/2$ respectively, for $x=0.07$. The spin-stiffness is in fact extracted from the magnon excitation curves, in a similar fashion as discussed in Sections 2.4.3 and 3.4.5.

In Figure 4.32 we show the normalized spin-stiffness D_n as a function of the concentration of nanospheres, corresponding to the case of $\lambda=a$. The
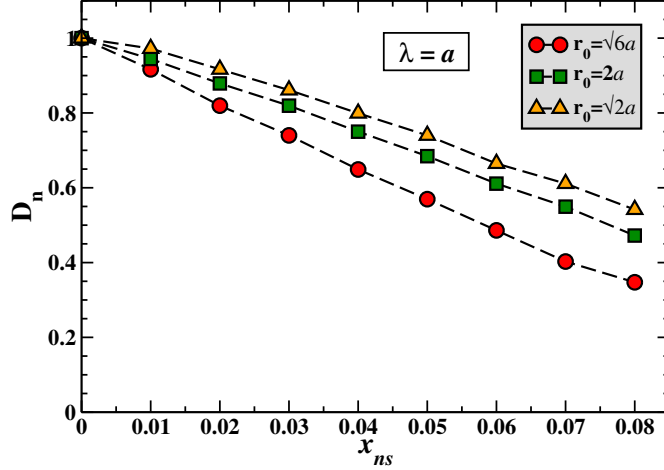
Figure 4.32: Normalized spin-stiffness D_n as a function of x_{ns}, for three different r_0: $\sqrt{6}a$, $2a$, and $\sqrt{2}a$. (Here $\lambda=a$ and $x_{in}=0.8$). (From Ref.[156]).

results are shown here for three different radii of nanospheres, where the concentration of impurities inside the nanospheres in each case is fixed at $x_{in}=0.8$. We observe a very interesting and surprising decrease of the spin-stiffness coefficient in the presence of inhomogeneities. The decrease is found to be almost monotonous with increase in x_{ns}. ($x_{ns}=0$ corresponds to the homogeneously diluted case). In fact, even more surprisingly, we notice that the suppression of the spin-stiffness is more for the spheres with larger radii. For $x_{ns}\sim0.03$, the spin-stiffness is reduced by almost 15% compared to the homogeneous value for $r_0=\sqrt{2}a$, and almost by 30% for $r_0=\sqrt{6}a$. This is in contrast to what is observed in the case of the Curie temperatures, although the effects are not as drastic. The decrease in the spin-wave stiffness, observed here, is consistent with the shift in the excitation peaks at low **q** values seen in Figure 4.26. It is interesting to note here that similar decrease in the spin-stiffness values was reported in double exchange systems in the presence of short-range correlated disorder[60], and the small ratios of D/T_C were found to be in very good agreement with those measured in manganites. But those

149

systems correspond to the clean limit, and cannot be compared to the diluted regime discussed here.
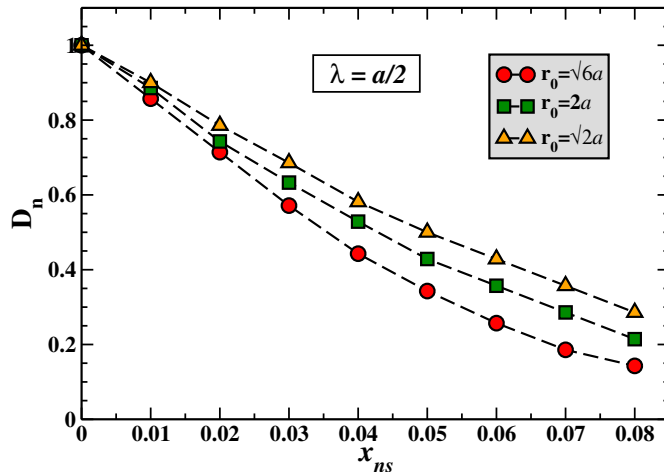
Figure 4.33: Normalized spin-stiffness D_n as a function of x_{ns}, for three different r_0: $\sqrt{6}a$, $2a$, and $\sqrt{2}a$. (Here $\lambda=a/2$ and $x_{in}=0.8$). (From Ref.[156]).

Now in Figure 4.33 we plot the normalized spin-stiffness D_n, corresponding to the case of the short-ranged couplings for $\lambda=a/2$. In this case too, we observe a similar monotonous decrease in the spin-stiffness coefficient with increase in the concentration of nanospheres. The decrease is found to be almost linear till $x_{ns}=0.04$. Compared to the case of $\lambda=a$, the suppression in the spin-stiffness values is found to be even more here. For $x_{ns}\sim0.03$, the spin-stiffness is reduced by more than 40% of the homogeneous value for the largest nanospheres with $r_0=\sqrt{6}a$. This is again consistent with our initial expectation, when we observed a strong shift of the low momentum $A(\mathbf{q},\omega)$ peaks toward lower energies with increasing x_{ns} (Figure 4.27). The effects of the nanoscale clusters on the spin-stiffness are in striking contrast to that observed on the critical temperatures, where we have observed an increase by almost one order of magnitude. These results show that in systems with effective short-ranged exchange interactions the spin-stiffness can be

significantly reduced in the presence of nanoscale inhomogeneities. However, detailed experimental studies, using inelastic neutron scattering or ferromagnetic resonance measurements, would prove to be very useful in confirming our predictions.

4.4.4 General Remarks

In the context of the results shown here we would like to mention that all these calculations were performed very recently, and the results are yet to be published [156]. A better understanding of the precise origin of these effects calls for a more detailed analysis. We are in course of investigating the different features discussed here by performing other detailed calculations. For example, in the inhomogeneous systems we have focused only on the particular case of nanospheres with radii r_0=2a and x_{in}=0.8. Now it would be very useful to consider nanospheres of other radii and with different concentrations of impurities inside, to analyze the nature of the magnon DOS and the excitation spectrum. Also interesting to observe would be the sensitivity of the spin-stiffness coefficient to the variation of the concentration of impurities inside the nanospheres,

As mentioned before, all the above calculations are performed at T= 0 K. Now it is possible to extend this study to the case of finite temperatures as well. It would be very interesting to analyze the effects of temperature on the spin dynamics of these inhomogeneous systems. This might further reveal newer and yet unknown properties of these complex systems. We believe that the finite temperature spin excitations, especially close to the critical temperatures, might help in providing a better understanding of the likely origin of anomalous magnetization behavior observed in these inhomogeneous systems.

4.5 Conclusion

To conclude, we have presented here a detailed and extensive study of the effects of nanoscale inhomogeneities on the Curie temperatures, the sponta-

neous magnetization, and the spin-wave excitations from a generalized perspective. We have shown that the presence of inhomogeneities can indeed lead to rich and interesting physics in these diluted magnetic systems. The important findings of this study can be summarized as the following:

- In materials with effective short ranged exchange interactions it is indeed possible to go beyond room-temperature ferromagnetism by inducting nanoscale clusters of magnetic impurities. A gigantic increase in the critical temperatures of up to 1600%, compared to that of the homogeneously diluted case, is obtained in certain cases.

- A plausible explanation for the wide variation of T_C's, observed experimentally, in some materials like (Ga,Mn)N is provided. Our study reveals that the relative separation between the inhomogeneities can play a decisive role in controlling the Curie temperatures.

- The temperature dependent magnetization is found to exhibit a non-trivial non-mean-field like behavior in the presence of inhomogeneities. A distinctly slow decay is observed in the average magnetization in systems with short ranged exchange couplings. This may be attributed to the strong couplings within the nanospheres which tend to prolong magnetic order near the critical temperatures.

- The nature of the local magnetizations is shown to provide a better qualitative understanding of the spontaneous magnetization of the systems. The effective exchange interactions are found to play an important role in controlling the magnetization behavior, consistent with what is found in the case of T_C.

- The average magnon DOS reveal interesting features and strong deviations when compared to that of the homogeneous case. Even for a relatively small concentration of inhomogeneities ($\sim 2\%$) the magnon bandwidth is found to be increased by almost a factor of three in systems with short-ranged interactions. We find that the average magnon

DOS resembles more the local DOS inside the nanoclusters at relatively high x_{ns}. This indicates the importance of the cluster impurities in determining the nature of the magnon DOS.

- The nanoscale inhomogeneities give rise to interesting features in the spin-wave spectrum. With increasing concentration of nanoclusters, well-defined excitations are strongly reduced and prominent excitations are found to appear at relatively higher energies in the spectrum. Although the exact origin is not so clear, these high energy excitations may be associated with the increasing localization of the magnons within the clusters. These findings can be further confirmed by detailed experimental studies, using inelastic neutron scattering measurements.

- Interestingly a decrease in the spin-stiffness coefficient is observed with increase in the concentration of inhomogeneities. We have found that in certain cases, the spin-stiffness can be reduced by almost 40% of the value corresponding to the homogeneous case. This relatively strong suppression of the spin-stiffness due to the clustering phenomenon is found to be exactly opposite to what is found in the case of the Curie temperatures. This clearly underlines the importance of disorder and highlights the competition between several relevant length scales (exchange couplings, size of inhomogeneities, etc.) in these complex inhomogeneous systems.

Chapter 5

General conclusion and Perspectives

5.1 Conclusions

This work mainly concerns the magnetic properties of diluted and disordered systems, and lays special emphasis on the effects of nanoscale inhomogeneities. The importance of disorder and percolation effects in these systems is outlined in the very beginning. In this context, we have discussed some of the theoretical approaches used very frequently in the literature. It is proved, beyond doubt, that the SC-LRPA is the most reliable and accurate tool to deal with these systems. Within this approach, the spin fluctuations are treated within the RPA and the disorder effects are almost exactly treated in real space. Also important is the fact that the localization and always leads to an incorrect estimation of the Curie temperatures and other magnetic properties. Now one might be tempted to use the Monte Carlo calculations, considered as in principle exact. However, we have seen that the SC-LRPA enjoys distinct advantages over the MC methods, in terms of finite size effects, reliable statistical sampling, and more importantly computational resources. Here we have further established the efficiency and accuracy of the SC-LRPA to study the magnetic excitation spectrum in diluted systems, for which we have considered the 3D nearest-neighbor diluted

Heisenberg model. A broadening in the excitation spectrum is observed close to the percolation threshold, which is attributed to the formation of localized magnon modes. We have also extracted the spin-stiffness values, which was found to vanish at the percolation threshold exactly. In addition, the calculated spin-stiffness was found to be in very good agreement with those obtained from a different theoretical approach. Hence we have successfully demonstrated that a proper treatment of the disorder and/or dilution effects is required for an accurate estimation of the relevant properties, and the SC-LRPA is the best tool for this.

Following this we have shown the indispensable role of a minimal model approach to study various properties of diluted magnetic systems. The V-J model had already been successfully implemented to ascertain the magnetic and transport properties in a wide range of III-V DMSs. We have studied here the Curie temperatures and the magnetic excitation spectrum for optimally annealed (Ga,Mn)As, within this one-band model. An excellent agreement was achieved between our calculated T_C's and those obtained from *ab initio* exchange integrals, as well as experimental values. We have also obtained a remarkable agreement for the spin-stiffness calculated from this model with those from *ab initio* couplings. We could as well reproduce most of the experimentally measured spin-stiffness in optimally annealed (Ga,Mn)As. The main feature of the V-J model is the non-perturbative treatment of the substitution effects in addition to the proper and reliable treatment of the disorder effects (percolation, localization). The Coulomb potential V was shown to play a crucial role in understanding the origin of ferromagnetism in DMSs. Although the V-J model has been primarily discussed in the context of DMSs here, it can be generalized to a wide class of diluted magnetic systems which makes it all the more powerful. This essentially helps to narrow down the gap between first-principles based studies and minimal model approaches.

Finally we have studied the effects of nanoscale inhomogeneities in diluted magnetic systems, which as already mentioned is the primary objective of this research work. The formation and appearance of inhomogeneities in various materials was already observed experimentally, and different inter-

esting properties were also reported. The most appealing among them was the room-temperature ferromagnetism observed in some cases. However, the exact origin of these high T_C's was not well understood and a proper theoretical description of the effects of this kind of impurity clustering was also lacking for a long time. In a major part of this manuscript, we have tried to provide a generalized and comprehensive study of the effects of nanoscale inhomogeneities on different magnetic properties of the diluted systems. We have proposed an innovative path to room-temperature ferromagnetism in these diluted materials, by the possible inclusion of nanoscale impurity clusters. It is shown that the Curie temperatures in some particular cases can be enhanced by up to 1600% compared to that of the homogeneously diluted case. This kind of phenomenal boost in the ordering temperatures of diluted magnetic systems have not been reported so far theoretically. We have also provided a credible explanation for the wide variation of the critical temperatures measured experimentally in certain materials. The effects of the inhomogeneities on the temperature dependent magnetization have been analyzed in details. The magnetizations are found to exhibit an anomalous non-mean-field like behavior, which also effectively depends on the range of the exchange interactions. The strong intra cluster couplings, which tend to prolong magnetic order, are believed to be one of the reasons for this anomalous magnetization behavior. Apart from these, we have also observed very interesting and unusual features in the magnetic excitation spectrum as compared to that of the homogeneous systems. The appearance of prominent high energy excitations, with increasing concentration of inhomogeneities, could be possibly attributed to the increasing localization of magnons in the nanoclusters. At the same time it was rather surprising to observe the effect on the spin-stiffness coefficient, which was found to be suppressed with an increase in the concentration of inhomogeneities. All our findings reported herein could be further corroborated by more detailed experimental and theoretical studies.

Thus in a nutshell we can say that the nanoscale inhomogeneities can give rise to very rich and new physics in these diluted magnetic systems. If, by proper control of the growth conditions the formation of these inhomo-

156

geneities can be manipulated, it will possibly open up a whole new branch of condensed matter physics, which had hitherto been almost unexplored. We believe that this study will pave the way for a better understanding of the impurity clustering effects and in particular help to identify the origin of high temperature ferromagnetism in dilute magnetic systems. These systems in turn can serve as potential building blocks for future spintronic devices.

5.2 Some future perspectives

5.2.1 Nanocolumns

In all our calculations, concerning inhomogeneous systems, the inhomogeneities are assumed to be in the form of nanospheres. Now it is possible to extend this study to a different kind of inhomogeneity − the nanocolumns. The presence of nanocolumns was already detected experimentally in some
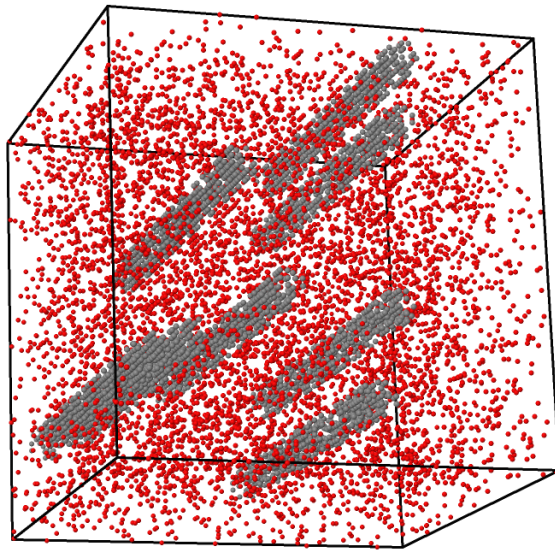

Figure 5.1: Snapshot of a simple cubic lattice containing nanocolumns. The grey (red) atoms denote the impurities inside (outside) the nanocolumns.

materials like (Ge,Mn)[19] and (Zn,Co)O[136]. In both the cases, as discusse before, room-temperature ferromagnetism has been reported. The

nanocolumns can lead to a magnetocrystalline anisotropy in the system, since the columns are fully extended in only one direction. This is essentially different from the case of the systems containing nanospheres. Thus the nanocolumns appear to be interesting from a fundamental perspective as well. We believe that a detailed analyses of the effects of nanocolumns would yield quantitatively new features in the Curie temperature, the spontaneous magnetization, the spin dynamics and a host of other properties in these materials. Hence we intend to perform similar calculations, as done within the framework of this thesis, assuming inhomogeneities in the form of nanocolumns in the near future.

5.2.2 Effect of inhomogeneities on transport properties

As already seen, in a major part of this thesis, nanoscale inhomogeneities can have quite drastic and interesting effects on the magnetic properties of the disordered and diluted systems. This gives rise to rich and fascinating physics in these systems. Now, from this perspective, it would be equally interesting to study the effects of these inhomogeneities on the transport properties, such as optical conductivity, resistivity, etc. We firmly believe that the transport properties will show interesting and new features in the presence of impurity clustering effects. Here we would like to focus on the particular case of the optical conductivity and the associated Drude weight. As discussed previously (Section 3.3.4), the optical conductivity calculated within the one-band V-J model[110] was found to explain the measured redshift in the conductivity peak in (Ga,Mn)As (consistent with the impurity band scenario). Also the Drude weight calculations revealed the proximity of (Ga,Mn)As to the metal-insulator transition. Thus the optical conductivity can be an interesting quantity to start with. The effects of the nanoclusters on the behavior of the conductivity peaks can give rise to interesting physics in these complex systems, which has hardly been studied until now. The total optical conductivity is given by $\sigma(\omega){=}\sum_\sigma \sigma_\sigma(\omega)$, where the subscript σ

denotes the spin index and $\sigma_\sigma(\omega)$ is given by

$$\sigma_\sigma(\omega) = D_\sigma \delta(\omega) + \sigma_\sigma^{reg}(\omega) \tag{5.1}$$

D_σ is the Drude weight (contribution at zero frequency) in the σ-sector, and $\sigma_\sigma^{reg}(\omega)$ is the regular part of the optical conductivity. The Drude weight is the order parameter which determines the metal-insulator transition. Now in order to separate the regular part (finite frequency) from the dc part (zero frequency), periodic boundary conditions should be implemented. The Drude weight is then calculated from the following sum-rule

$$D_\sigma = - \int_0^\infty \sigma_\sigma^{reg}(\omega)d\omega - \frac{\sigma_0}{\hbar} \frac{\langle \hat{K}_\sigma^x \rangle}{N} \tag{5.2}$$

where $\langle \hat{K}_\sigma^x \rangle$ is the average kinetic energy in the x-direction and σ-sector, $N=L^3$ is the total number of sites, and $\sigma_0=\pi e^2/\hbar a$, (a is the simple cubic lattice parameter). Now the regular part of the optical conductivity, $\sigma_\sigma^{reg}(\omega)$, was obtained within the Kubo formalism in Ref.[110]. This involves matrix diagonalization in order to calculate the required eigenvalues and eigenfunctions. Now to study systems with inhomogeneities in a reliable way, the typical size of the systems should be sufficiently large in comparison to the size of the impurity clusters. This implies that the matrices to be diagonalized are also very big, and this can be quite expensive in terms of computational resources. Hence we need some alternative tool or method to efficiently deal with these problems. We will come back to this in the following.

5.2.3 Exchange couplings in presence of inhomogeneities

Throughout this study we have assumed the exchange interactions in inhomogeneous systems to be of a generalized isotropic form with an exponential decay. This, as we have demonstrated, was found to be a reasonably good choice with respect to the real couplings in several diluted materials. However, in order to have an even better quantitative idea of the effects of in-
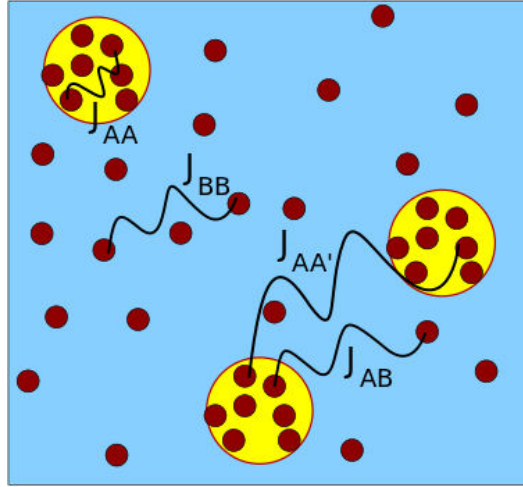
Figure 5.2: Schematic diagram showing the different kind of couplings in a system with inhomogeneities.

homogeneities, it would be vastly useful to calculate the magnetic couplings in the presence of inhomogeneities. These couplings can then be used to calculate the different properties of the systems. One of the advantages of this is we can identify the relevant couplings related to the impurities inside and outside the clusters. This would help us understand in a better way the possible origin of several interesting features as already observed. Figure 5.2 shows a schematic representation of the different type of couplings that one can obtain in a system with impurity clusters. In the figure, the intra cluster couplings are denoted by J_{AA}, the inter cluster couplings by $J_{AA'}$, the coupling between an impurity inside and one outside by J_{AB}, and the couplings between two impurities outside by J_{BB}, respectively.

5.2.4 Efficient method to calculate couplings and optical conductivity

The idea that we put forward here is to calculate the exchange couplings as well as the optical conductivity within the one-band V-J model[97] in presence of inhomogeneities. This model has already been shown to be very efficient and reliable to obtain the magnetic and transport properties in a

wide class of homogeneously diluted magnetic systems (Section 3.3). Now, the couplings and the optical conductivity need to be calculated on considerably large system sizes compared to the typical size of the inhomogeneities, in order to have reliable estimates and account for finite size effects. These calculations require diagonalization of the Hilbert space, which is proportional to the number of sites in the system. For a system size of L=40, the matrix to be diagonalized is already on the order of 64000×64000. This can be computationally very expensive in time. Hence we suggest to use a different approach based on the kernel polynomial method (KPM)[158], which is comparatively much faster and at the same time accurate. The exchange coupling between two magnetic impurities can be expressed in terms of the matrix elements of the local density of states $\rho_{ij}(E)$, as

$$J_{ij} = -\frac{J^2}{4\pi S^2} \int_{E<E_F} \int_{E'>E_F} \frac{F_{ij}(E,E')}{E-E'} dEdE' \tag{5.3}$$

where

$$F_{ij}(E,E') = Re[\rho_{ij}^{\uparrow}(E)\rho_{ji}^{\downarrow}(E')] \tag{5.4}$$

and $\rho_{ij}^{\sigma}(E) = \langle i|\delta(E-\hat{H}^{\sigma})|j\rangle$. Here J is the local coupling constant between the localized impurities and the itinerant carriers, S denotes the magnetic impurity spin, and $\hat{H}$ corresponds to the V-J Hamiltonian. Now within the KPM, the local density of states is calculated very efficiently from the following relation

$$\rho_{ij}(E) \approx \frac{1}{\pi\sqrt{1-E^2}} \left[g_0\mu_0^{ij} + 2\sum_{l=1}^{M} g_l\mu_l^{ij}T_l(E) \right] \tag{5.5}$$

where $T_l(E)$ are the Chebyshev polynomials of the first kind, given by

$$\mu_l^{ij} = \langle i|T_l(\hat{H})|j\rangle \tag{5.6}$$

and g_l are the Jackson kernel coefficients. M is a cutoff number used to truncate the polynomial sum. The coefficients μ_l^{ij} are obtained from the

recurrence relation of Chebyshev polynomials, given by

$$T_{l+1}(\hat{H}) = 2\hat{H}T_l(\hat{H}) - T_{l-1}(\hat{H}) \tag{5.7}$$

with $T_0(\hat{H})=1$, and $T_1(\hat{H})=\hat{H}$.

The regular part of the optical conductivity can be calculated using the following relation

$$\sigma^{reg}(\omega) = \frac{1}{\omega} \int_{-\infty}^{\infty} j(y+\omega)[f_{E_F}(y) - f_{E_F}(y+\omega)]dy \tag{5.8}$$

where $j(x, y)$ is the matrix element density and f_{E_F} represents the Fermi distribution function. Now $j(x, y)$ can be expanded by using a polynomial expansion of order M,

$$j(x, y) = \sum_{m,n=0}^{M-1} \frac{\mu_{mn} h_{mn} g_m g_n T_m(x) T_n(y)}{\pi^2 \sqrt{(1-x^2)(1-y^2)}} \tag{5.9}$$

where the expansion coefficients are given by

$$\mu_{mn} = Tr[T_n(\hat{H}) J T_m(\hat{H}) J] \tag{5.10}$$

This trace is then calculated by using an average over some random vectors (for more details see Ref.[158]).

Now the calculation of these coefficients from the recurrence relations of Chebyshev polynomials represents the most time consuming part of this approach. However, as we can see, the KPM does not involve matrix diagonalization and hence very large systems can be studied at the expense of relatively less computational time. Note that a similar kind of numerical approach, based on an expansion of orthogonal polynomials, was proposed in Ref.[159] to study RKKY interactions in aperiodic systems. Thus, within KPM approach, we can efficiently calculate the exchange couplings and the optical conductivity, within the one-band V-J model, for realistic materials containing inhomogeneities. Using these couplings one can then calculate the Curie temperatures and other magnetic properties, in a similar fashion

as described in this manuscript. This would definitely lead to interesting quantitative results, and also help to confirm the predictions made in this work.

Appendix A

T$_C$ from the Mean field and Virtual Crystal Approximation

In this annexe, we will derive the expression for the Curie temperature obtained within the mean field and virtual crystal approximation. For this we start with the effective Heisenberg Hamiltonian given by

$$H_{Heis} = -\sum_{i,j} p_i p_j J_{i,j} \mathbf{S}_i \cdot \mathbf{S}_j \qquad (A.1)$$

where $\mathbf{S}_i$ is a localized spin (can be classical or quantum) at site i, and the random variable p_i is 1 if the site is occupied by a spin otherwise it is 0. Now assuming the ground state of the system to be completely ferromagnetic and saturated along the z-axis, the effective Hamiltonian within the MF approximation can be written as

$$H^{MF} = -\sum_i h_i^{MF} S_i^z \qquad (A.2)$$

where the local effective field is defined by

$$h_i^{MF} = \sum_j J_{ij} \langle S_j^z \rangle \qquad (A.3)$$

Now within the VCA, all sites of the system are considered as equivalent and the sum over the occupied sites is replaced by a sum over all sites with a weight proportional to the concentration of the spins. Then the local effective field at each site becomes

$$h^{MF-VCA} = 2x \sum_j J_{ij} \langle S^z \rangle \qquad (A.4)$$

Note that the sum now extends over all sites and the factor 2 arises as a result of double counting in the Heisenberg Hamiltonian. Now the average magnetization is given by

$$\langle S^z \rangle = \frac{Tr(e^{-\beta H^{MF-VCA}} S^z)}{Tr(e^{-\beta H^{MF-VCA}})} \qquad (A.5)$$

From the above equation further calculations yield the following expression for $\langle S^z \rangle$,

$$\langle S^z \rangle = S B_S(\beta h^{MF-VCA}) \qquad (A.6)$$

where B_S is the Brillouin function defined by

$$B_S(z) = \frac{2S+1}{S} \coth\left(\frac{2S+1}{2S}z\right) - \frac{1}{2S} \coth\left(\frac{z}{2S}\right) \qquad (A.7)$$

As known when the temperature approaches the Curie temperature, the magnetization tends to zero. Thus in the limit $z \to 0$ the Brillouin function becomes

$$B_S(z) \approx \frac{1}{3}S(S+1)z \qquad (A.8)$$

Hence for the expression of the Curie temperature, within the MF and VCA, we finally obtain

$$k_B T_C^{MF-VCA} = \frac{2}{3}S(S+1)x \sum_i J_{0i} \qquad (A.9)$$

Appendix B

Summary of the SC-LRPA method

In this annexe we present a summary of the SC-LRPA formalism. The SC-LRPA is essentially an extension of the standard RPA, which was successfully used for ordered systems[63, 160], to the case of disordered systems. For this we consider a system of N_{imp} interacting spins (quantum or classical) randomly distributed on a lattice of N sites, which is given by the effective diluted Heisenberg Hamiltonian

$$\mathcal{H} = -\sum_{i,j} J_{ij} p_i p_j \mathbf{S}_i \cdot \mathbf{S}_j \tag{B.1}$$

where the localized spins $\mathbf{S}_i$ and $\mathbf{S}_j$ are situated at the sites i and j of the host lattice respectively. The random variable p_i is 1 if the site is occupied by an impurity otherwise it is 0. We introduce the retarded Green's function, which describe the transverse spin fluctuations, as

$$G_{ij}(t) = -i\theta(t)\langle [S_i^+(t), S_j^-(0)]\rangle \tag{B.2}$$

where $[\hat{A},\hat{B}]$ denotes the commutator and the expectation value of an operator $\hat{A}$ is given by

$$\langle \hat{A} \rangle = \frac{Tr(e^{-\beta\mathcal{H}}\hat{A})}{Tr(e^{-\beta\mathcal{H}})} \tag{B.3}$$

The Fourier transform of the above Green's function is defined as

$$G_{ij}(\omega) = \int_{-\infty}^{+\infty} G_{ij}(t)e^{i\omega t}dt = \langle\langle S_i^+; S_j^- \rangle\rangle \tag{B.4}$$

The exact equation of motion of $G_{ij}(\omega)$ in real space is

$$\omega G_{ij} = 2\langle S_i^z \rangle \delta_{ij} + \langle\langle [S_i^+, \mathcal{H}]; S_j^- \rangle\rangle \tag{B.5}$$

Now the commutator on the right hand side of the above equation is given by

$$[S_i^+, \mathcal{H}] = \sum_l J_{il}(S_i^z S_l^+ - S_l^z S_i^+) \tag{B.6}$$

This gives rise to higher order Green's functions of the form $\langle\langle S_i^+ S_l^z; S_j^- \rangle\rangle$, in the equation of motion. This is decoupled using the Tyablicov decoupling[54] or random phase approximation (RPA). Within this procedure the correlations between S_l^z and S_i^+ are neglected and the higher order Green's functions $\langle\langle S_i^+ S_l^z; S_j^- \rangle\rangle$ are replaced by $\langle S_l^z \rangle \langle\langle S_i^+; S_j^- \rangle\rangle$,

$$\langle\langle S_i^+ S_l^z; S_j^- \rangle\rangle \longrightarrow \langle S_l^z \rangle \langle\langle S_i^+; S_j^- \rangle\rangle \tag{B.7}$$

$\langle S_l^z \rangle$ represents the local magnetization at each site for a diluted system and this has to be evaluated *self-consistently* at each temperature and for each configuration of disorder. Within the self-consistent local RPA, the equation of motion (B.5) becomes

$$(\omega - h_i^{eff})G_{ij}(\omega) = 2\langle S_i^z \rangle \delta_{ij} - \langle S_i^z \rangle \sum_l J_{il} G_{lj}(\omega) \tag{B.8}$$

where $h_i^{eff} = \sum_l J_{il} \langle S_l^z \rangle$ is the local effective field at site i. Now we can write Equation B.8 in a concise form,

$$(\omega \mathbf{I} - \mathbf{H}_{eff})\mathbf{G} = \mathbf{D} \tag{B.9}$$

where $\mathbf{H}_{eff}$, $\mathbf{G}$ and $\mathbf{D}$ are $N_{imp} \times N_{imp}$ matrices. The effective Hamiltonian matrix elements are given by

$$(\mathbf{H}_{eff})_{ij} = -\langle S_i^z \rangle J_{ij} + \delta_{ij} \sum_l \langle S_l^z \rangle J_{lj} \tag{B.10}$$

and

$$(\mathbf{D})_{ij} = 2\langle S_i^z \rangle \delta_{ij} \tag{B.11}$$

We immediately observe from the above equations that

$$\sum_j (\mathbf{H}_{eff})_{ij} = 0 \tag{B.12}$$

which in turn implies that zero (Goldstone mode) is an eigenvalue of $\mathbf{H}_{eff}$. Hence the SC-LRPA treatment is found to be consistent with the Goldstone theorem. It is interesting to note that the matrix $\mathbf{H}_{eff}$ is non-Hermitian (real and non-symmetric) but the spectrum is real and positive at each temperature. Actually this matrix has the property of bi-orthogonality[76]. Hence one needs to define the right and left eigenvectors of $\mathbf{H}_{eff}$ denoted by $|\Psi_\alpha^R\rangle$ and $\langle \Psi_\alpha^L|$ respectively, both associated with the same eigenvalue ω_α, which satisfy the following

$$\mathbf{H}_{eff}|\Psi_\alpha^R\rangle = \omega_\alpha|\Psi_\alpha^R\rangle \tag{B.13}$$

$$\langle \Psi_\alpha^L|\mathbf{H}_{eff} = \omega_\alpha\langle \Psi_\alpha^L| \tag{B.14}$$

These vectors obey the relation

$$\langle \Psi_\alpha^L | \Psi_\beta^R \rangle = \delta_{\alpha,\beta} \quad \text{(B.15)}$$

which indicate that two eigenvectors belonging to to the same family (L or R) are not orthogonal to each other in general. Now inserting the L and R eigenvectors in Equation B.9, the retarded Green's functions can be written as

$$G_{ij}(\omega) = \sum_\alpha \frac{2\langle S_j^z \rangle}{\omega - \omega_\alpha + i\epsilon} \langle i | \Psi_\alpha^R \rangle \langle \Psi_\alpha^L | j \rangle \quad \text{(B.16)}$$

Now in the case of disordered systems, the local magnetization $\langle S_i^z \rangle$ is evaluated from an expression similar to that given by Callen[63] for clean systems. This relates the local Green's function at site i to the local magnetization at this site,

$$\langle S_i^z \rangle = \frac{(S - \Phi_i)(1 + \Phi_i)^{2S+1} + (1 + S + \Phi_i)\Phi_i^{2S+1}}{(1 + \Phi_i)^{2S+1} - \Phi_i^{2S+1}} \quad \text{(B.17)}$$

where the local effective magnon occupation number is given by

$$\Phi_i = -\frac{1}{2\pi \langle S_i^z \rangle} \int_{-\infty}^{+\infty} \frac{\Im G_{ii}(\omega)}{exp(\beta\omega) - 1} d\omega \quad \text{(B.18)}$$

Note that $-\frac{1}{2\pi\langle S_i^z \rangle} \Im G_{ii}(\omega)$ is actually the local magnon DOS $\rho_i(\omega)$ at site i. The equations B.8, B.16, B.17 and B.18 form the basis of the SC-LRPA scheme, which has been used extensively throughout this manuscript.

Expression for the Curie temperature

Now when the temperature of the system approaches the Curie temperature T_C, the local magnetization $\langle S_i^z \rangle$ goes to zero, and the local density of magnons diverges, $\Phi_i \to \infty$. From Equation B.17, we obtain

$$\langle S_i^z \rangle \approx \frac{1}{3} S(S+1) \frac{1}{\Phi_i} \quad \text{(B.19)}$$

We define the average magnetization of the system as

$$m = \langle\langle S^z \rangle\rangle = \frac{1}{N_{imp}} \sum_i \langle S_i^z \rangle \tag{B.20}$$

and introduce the reduced variables

$$E = \frac{\omega}{m} \tag{B.21}$$

$$\lambda_i = lim_{T \to T_C} \frac{\langle S_i^z \rangle}{m} \tag{B.22}$$

From Equation B.17, the effective number of magnons now becomes

$$\Phi_i = \frac{T_C}{m} \int_{-\infty}^{+\infty} \frac{A_{ii}(E)}{E} dE \tag{B.23}$$

where $A_{ii}(E)$ is given by the equation

$$A_{ii}(E) = -\frac{1}{2\pi\lambda_i} \Im G_{ii}(E) \tag{B.24}$$

Now from equations B.18 and B.22, we obtain a semi-analytic expression for the critical temperature,

$$k_B T_C = \frac{1}{3} S(S+1) \frac{1}{N_{imp}} \sum_i \frac{1}{F_i} \tag{B.25}$$

where

$$F_i = \int_{-\infty}^{\infty} \frac{A_{ii}(E)}{E} dE \tag{B.26}$$

This quantity F_i depends on the local parameters λ_i ($i=1,2,...N_{imp}$), which have to be determined self-consistently at each temperature. Now, if we rewrite this equation in terms of the eigenvalues and eigenvectors of the effective Hamiltonian $\mathbf{H}_{eff}$, we get

$$F_i = \sum_{\alpha \neq 0} \frac{\langle i|\Psi_\alpha^R \rangle \langle \Psi_\alpha^L |i\rangle}{E_\alpha} \tag{B.27}$$

where $E_\alpha = \omega_\alpha/m$ and $E_0 = 0$ is the Goldstone mode. Then the expression for the Curie temperature becomes

$$T_C = \frac{1}{3}S(S+1)\frac{1}{N_{imp}}\sum_i\left(\sum_{\alpha\neq 0}\frac{\langle i|\Psi_\alpha^R\rangle\langle\Psi_\alpha^L|i\rangle}{E_\alpha}\right)^{-1} \tag{B.28}$$

Note that the Goldstone mode is excluded from the sum in Equation B.26. This is essential as the inclusion of this mode always leads to a zero critical temperature in the case of finite size systems. From the expression of T_C (Equation B.27), we see that the critical temperature depends both on the excitation spectrum as well as the nature of the magnetic excitations. There is a contribution from both the localized states and the extended states. However, it is not an easy task to determine the contribution of each type of excitation to the magnitude of the Curie temperature. Hence a proper description of the nature of the magnetic excitations is essential to provide a correct estimate of the Curie temperatures.

Thus we have obtained a semi analytic expression for the Curie temperature in disordered systems within the SC-LRPA formalism. It should be noted that the formalism shown here is general in nature as we can calculate the complete Green's functions of a system and hence evaluate other properties like the average magnetization, and the magnetic excitation spectrum of a system.

Bibliography

[1] S. Datta and B. Das, Appl. Phys. Lett. **56,** 665 (1990).

[2] S. A. Wolf *et al.*, Science **294,** 1488 (2001).

[3] I. Zutić, J. Fabian, and S. Das Sarma, Rev. Mod. Phys. **76,** 323 (2004).

[4] J. De Boeck *et al.*, Semicond. Sci. Technol. **17,** 342 (2002).

[5] D. Kennedy and C. Norman, Science **309,** 82 (2005).

[6] T. Dietl, H. Ohno, F. Matsukura, J. Cibert, and D. Ferrand, Science **287,** 1019 (2000).

[7] M. Moreno, A. Trampert, B. Jenichen, L. Däweritz, K. H. Ploog, J. Appl. Phys. **92,** 4672 (2002).

[8] M. Yokoyama, H. Yamaguchi, T. Ogawa, and M. Tanaka, J. Appl. Phys. **97,** 10D317 (2005).

[9] G. Martínez-Criado *et al.*, Appl. Phys. Lett. **86,** 131927 (2005).

[10] L. Vitali, M. G. Ramsey, and F. P. Netzer, Phys. Rev. Lett. **83,** 316 (1999).

[11] J.-Long Li *et al.*, Phys. Rev. Lett. **88,** 066101 (2002).

[12] I. B. Altfeder, J. J. Hu, A. A. Voevodin, and J. Krim, Phys. Rev. Lett. **102,** 136104 (2009).

[13] C. V. Parker *et al.*, Phys. Rev. Lett. **104,** 117001 (2010).

[14] M. Fäth, S. Freisem, A. A. Menovsky, Y. Tomioka, J. Aarts, and J. A. Mydosh, Science **285,** 1540 (1999).

[15] J. Tao, D. Niebieskikwiat, M. Varela, W. Luo, M. A. Schofield, Y. Zhu, M. B. Salamon, J. M. Zuo, S. T. Pantelides, and S. J. Pennycook, Phys. Rev. Lett. **103,** 097202 (2009).

[16] M. Z. Hasan and C. L. Kane, Rev. Mod. Phys. **82,** 3045 (2010).

[17] H. Beidenkopf, P. Roushan, J. Seo, L. Gorman, I. Drozdov, Y. San Hor, R. J. Cava, and A. Yazdani, Nature Phys. **7,** 939 (2011).

[18] H. Ohno, H. Munekata, T. Penney, S. von Molnar, and L.L. Chang , Phys. Rev. Lett. **68,** 2664 (1992).

[19] M. Jamet, A. Barski, T. Devillers, V. Poydenot, R. Dujardin, P. Bayle-Guillemaud, J. Rothman, E. Bellet-Amalric, A. Marty, J. Cibert, R. Mattana, and S. Tatarenko, Nat. Mater. **5,** 653 (2006).

[20] P. A. Lee and T. V. Ramakrishnan, Rev. Mod. Phys. **57,** 287 (1985).

[21] B. Kramer, and A. MacKinnon, Rep. Prog. Phys. **56,** 1469 (1993).

[22] I. A. Abrikosov, O. Eriksson, P. Söderlind, H. L. Skriver, and B. Johansson, Phys. Rev. B **51**, 1058 (1995).

[23] V. L. Moruzzi, Phys. Rev. B **41**, 6939 (1990).

[24] P. James, O. Eriksson, B. Johansson, and I. A. Abrikosov, Phys. Rev. B **59**, 419 (1999).

[25] I. Turek, J. Kudrnovsky, V. Drchal, and P. Weinberger, Phys. Rev. B **49**, 3352 (1994).

[26] M. Hennion, F. Moussa, P. Lehouelleur, F. Wang, A. Ivanov, Y. M. Mukovskii, and D. Shulyatev, Phys. Rev. Lett. **94**, 057006 (2005).

[27] F. Ye, P. Dai, J. A. Fernandez-Baca, Hao Sha, J. W. Lynn, H. Kawano-Furukawa, Y. Tomioka, Y. Tokura, and J. Zhang, Phys. Rev. Lett. **96**, 047204 (2006).

[28] J. M. D. Coey, M. Viret, L. Ranno, and K. Ounadjela, Phys. Rev. Lett. **75**, 3910 (1995).

[29] S. Karmakar, S. Taran, B. K. Chaudhuri, H. Sakata, C. P. Sun, C. L. Huang, and H. D. Yang, Phys. Rev. B **74**, 104407 (2006).

[30] Y. Motome and N. Furukawa, Phys. Rev. B **71**, 014446 (2005).

[31] I. S. Elfimov, S. Yunoki, and G. A. Sawatzky, Phys. Rev. Lett. **89**, 216403 (2002).

[32] J. Osorio-Guillen, S. Lany, S. V. Barabash, and A. Zunger, Phys. Rev. Lett. **96**, 107203 (2006).

[33] M. Venkatesan, C. B. Fitzgerald, and J. M. D. Coey, Nature(London) **430**, 630 (2004).

[34] D. P. Young, D. Hall, M. E. Torelli, Z. Fisk, J. L. Sarrao, J. D. Thompson, H.-R. Ott, S. B. Oseroff, R. G. Goodrich, and R. Zysler, Nature(London) **397**, 412 (1999).

[35] G. Bouzerar and T. Ziman, Phys. Rev. Lett. **96**, 207602 (2006).

[36] F. Máca, J. Kudrnovský, V. Drchal, and G. Bouzerar, Appl. Phys. Lett. **92**, 212503 (2008).

[37] C. Timm, J. Phys. Condens. Matter **15,** R1865 (2003).

[38] S. R. Broadbent and J. M. Hammersley, Proc. Camb. Philos. Soc. **53**, 629 (1957).

[39] P. Dean and N. F. Bird, Proc. Camb. Philos. Soc. **63**, 477 (1967).

[40] S. Kirkpatrick, Solid State Commun. **12**, 1279 (1973).

[41] O. P. Vajk, P. K. Mang, M. Greven, P. M. Gehring, and J. W. Lynn, Science **295**, 1691 (2002).

[42] P. Weiss, J. de Phys. **6**, 661 (1907).

[43] N. D. Mermin and H. Wagner, Phys. Rev. Lett. **17**, 1133 (1966).

[44] J. Goldstone, Nuovo Cimento **19**, 54 (1961).

[45] P. Soven, Phys. Rev. **156,** 809 (1967).

[46] B. Velický, S. Kirkpatrick, and H. Ehrenreich, Phys. Rev. **175,** 747 (1968).

[47] H. Shiba, Prog. Theor. Phys. **46**, 77 (1971).

[48] H. Akai and P. H. Dederichs, Phys. Rev. B **47**, 8739 (1993).

[49] H. Tange, T. Tokunaga, and M. Goto, J. Phys. Soc. Jpn. **45**, 105 (1978).

[50] G. Bouzerar and P. Bruno, Phys. Rev. B **66**, 014410 (2002).

[51] H. Akai, J. Phys. Condens. Matter **1**, 8045 (1989).

[52] I. Turek *et al.*, *Electronic Structure of Disordered Alloys, Surfaces and Interfaces* (Kluwer Academic, Boston, 1997).

[53] K. Sato, L. Bergqvist, J. Kudrnovský, P. H. Dederichs, O. Eriksson, I.Turek, B. Sanyal, G. Bouzerar, H. Katayama-Yoshida, V. A. Dinh, T. Fukushima, H. Kizaki and R. Zeller, Rev. Mod. Phys. **82,** 1633 (2010).

[54] S.V. Tyablikov, Ukr. Mat. Zh. **11**, 287 (1959).

[55] F. Yonezawa, Prog. Theor. Phys. **40**, 34 (1968).

[56] P. L. Leath, Phys. Rev. **171**, 725 (1968).

[57] G. Bouzerar, T. Ziman, and J. Kudrnovský, Europhys. Lett. **69**, 812 (2005).

[58] L. Bergqvist, O. Eriksson, J. Kudrnovský, V. Drchal, A. Bergman, L. Nordström, and I. Turek, Phys. Rev. B **72**, 195210 (2005).

[59] G. Bouzerar, T. Ziman, and J. Kudrnovský, Phys. Rev. B **72**, 125207 (2005).

[60] G. Bouzerar and O. Cépas, Phys. Rev. B **76**, 020401(R) (2005).

[61] H. Saito, V. Zayets, S. Yamagata, and K. Ando, Phys. Rev. Lett. **90,** 207202 (2003).

[62] K. Chen, A. M. Ferrenberg, and D. P. Landau, Phys. Rev. B **48**, 3249 (1993).

[63] H. B. Callen, Phys. Rev.**130**, 890 (1963).

[64] Y. Motome and N. Furukawa, Phys. Rev. B **68**, 144432 (2003).

[65] D. P. Landau and K. Binder, *A Guide to Monte Carlo Simulations in Statistical Physics*, (Cambridge University Press, Cambridge, 2000).

[66] R. Bouzerar and G. Bouzerar, New J. Phys. **12**, 053042 (2010).

[67] F. Popescu, Y. Yildrim, G. Alvarez, A. Moreo, and E. Dagotto, Phys. Rev. B **73**, 075206 (2006).

[68] Y. Yildrim, G. Alvarez, A. Moreo, and E. Dagotto, Phys. Rev. Lett. **99**, 057207 (2007).

[69] G. Bouzerar and R. Bouzerar, Phys. Rev. Lett. **100**, 229701 (2008).

[70] J. L. Alonso, L. A. Fernández, F. Guinea, V. Laliena, and V. Martín Mayor, Nucl. Phys. B **596**, 587 (2001).

[71] Y. Motome and N. Furukawa, J. Phys. Soc. Japan **68**, 3853 (1999).

[72] A. Chakraborty and G. Bouzerar, Phys. Rev. B **81**, 172406 (2010).

[73] A. M. Ferrenberg and D. P. Landau, Phys. Rev. B **44**, 5081 (1991).

[74] F. D. A. Aarao Reis, Phys. Rev. B **58**, 394 (1998).

[75] A. Gordillo-Guerrero and J. J. Ruiz-Lorenzo, J. Stat. Mech. P06014 (2007).

[76] For more details on bi-orthogonality see J. Dieudonné, Michigan Math. J. **2**, 7-20 (1953).

176

[77] V. Dobrosavljević, A. A. Pastor, and B. K. Nikolić, Europhys. Lett. **62**(1), 76, 2003.

[78] Y. J. Uemura and R. J. Birgeneau, Phys. Rev. B **36**, 7024 (1987).

[79] R. Orbach and K. W. Yu, J. Appl. Phys. **61**, 3689 (1987).

[80] A. Aharony, S. Alexander, O. Entin-Wohlman, and R. Orbach, Phys. Rev. Lett. **58**, 132 (1987).

[81] G. Bouzerar, Europhys. Lett. **79**, 57007 (2007).

[82] A. Chakraborty and G. Bouzerar, *to be submitted.*

[83] T. Jungwirth, J. Sinova, J. Masek, J. Kucera, and A. H. MacDonald, Rev. Mod. Phys. **78,** 809 (2006).

[84] J. M. Luttinger and W. Kohn, Phys. Rev. **97,** 869 (1955).

[85] R. Bouzerar, G. Bouzerar, and T. Ziman, Phys. Rev. B **73**, 024411 (2006).

[86] W. Kohn and L. Sham, Phys. Rev. **140,** A1133 (1965).

[87] P. Hohenberg and W. Kohn, Phys. Rev. **136,** B864 (1964).

[88] R. O. Jones and O. Gunnarsson, Rev. Mod. Phys. **61,** 689 (1989).

[89] J. H. Park, S. K. Kwon, and B. I. Min, Physica B **281/282,** 703 (2000).

[90] L. M. Sandratskii, P. Bruno, and J. Kudrnovský, Phys. Rev. B **69,** 195203 (2004).

[91] K. Sato, P. H. Dederichs, and H. Katayama-Yoshida, Europhys. Lett. **61,** 403 (2003).

[92] J. Kudrnovský, I. Turek, V. Drchal, F. Máca, P. Weinberger, and P. Bruno, Phys. Rev. B **69**, 115208 (2004).

[93] T. Chanier, F. Virot, and R. Hayn, Phys. Rev. B **79**, 205204 (2009).

[94] M. Berciu and R. N. Bhatt, Phys. Rev. Lett. **87,** 107203 (2001).

[95] G. Alvarez, M. Mayr, and E. Dagotto, Phys. Rev. Lett., **89,** 277202 (2002).

[96] R. N. Bhatt, M. Berciu, M. P. Kennett, and X. Wan, J. Supercond. **15,** 71 (2002).

[97] R. Bouzerar and G. Bouzerar, Europhys. Lett. **92**, 47006 (2010).

[98] J. Okabayashi, A. Kimura, O. Rader, T. Mizokawa, A. Fujimori, T. Hayashi, and M. Tanaka, Phys. Rev. B **58**, R4211 (1998).

[99] A. K. Bhattacharjee and C. Benoit á la Guillaume, Solid State Commun. **113**, 17 (2000).

[100] R. A. Chapman and W. G. Hutchinson, Phys. Rev. Lett. **18**, 443 (1967).

[101] M. Linnarsson, E. Janzen, B. Monemar, M. Kleverman, and A. Thilderkvist, Phys. Rev. B **55**, 6938 (1997).

[102] A. M. Yakunin *et al.*, Phys. Rev. Lett. **92**, 216806 (2004).

[103] M.I Katsnelson and A. I. Lichtenstein, Phys. Rev. B **61**, 8906 (2000).

[104] P. Mahadevan and A. Zunger, Phys. Rev. B **69**, 115211 (2004).

[105] K. S. Burch, D. D. Awschalom, and D. N. Basov, J. Magn. Magn. Mater. **320** 3207 (2008).

[106] J. Wang *et al.*, J. Phys. Condens. Matter **18**, R501 (2006).

[107] H. Ohno, J. Cryst. Growth **251**, 285 (2003).

[108] M. A. Scarpulla *et al.*, Phys. Rev. Lett. **95**, 207204 (2005).

[109] K. S. Burch *et al.*, Phys. Rev. Lett. **97**, 087208 (2006).

[110] R. Bouzerar and G. Bouzerar, New J. Phys. **13**, 023002 (2011).

[111] A. Chakraborty, R. Bouzerar, and G. Bouzerar, Eur. Phys. J. B **81**, 405 (2011).

[112] L. Bergqvist *et al.*, Phys. Rev. B **67**, 205201 (2003).

[113] L. Bergqvist, O. Eriksson, J. Kudrnovský, V. Drchal, P. Korzhavyi and I. Turek, Phys. Rev. Lett. **93**, 137202 (2004).

[114] K. Sato, W. Schweika, P. H. Dederichs and H. Katayama-Yoshida, Phys. Rev. B **70**, 201202(R) (2004).

[115] K. W. Edmonds, K. Y. Wang, R. P. Campion, A. C. Neumann, N. R. S. Farley, B. L. Gallagher, and C. T. Foxon, Appl. Phys. Lett. **81,** 4991 (2002).

[116] K. W. Edmonds *et al.*, Phys. Rev. Lett. **92,** 037201 (2004).

[117] F. Matsukura, H. Ohno, A. Shen, and Y. Sugawara, Phys. Rev. B **57,** R2037 (1998).

[118] D. Chiba *et al.*, Appl. Phys. Lett. **82**, 3020 (2003).

[119] S. T. B. Goennenwein *et al.*, Appl. Phys. Lett. **82**, 730 (2003).

[120] M. Sperl *et al.*, Phys. Rev. B **77**, 125212 (2008).

[121] T. Jungwirth *et al.*, Phys. Rev. B **72,** 165204 (2005).

[122] M. E. Overberg, C. R. Abernathy, S. J. Pearton, N. A. Theodor-opoulou, K. T. McCarthy, and A. F. Hebard, Appl. Phys. Lett. **79,** 1312 (2001).

[123] N. Theodoropoulou, A. F. Hebard, M. E. Overberg, C. R. Abernathy, S. J. Pearton, S. N. G. Chu, and R. G. Wilson, Appl. Phys. Lett. **78,** 3475 (2001).

[124] M. L. Reed, N. A. El-Masry, H. H. Stadelmaier, M. K. Ritums, M. J. Reed, C. A. Parker, J. C. Roberts, and S. M. Bedair, Appl. Phys. Lett. **79,** 3473 (2001).

[125] G. T. Thaler, M. E. Overberg, B. Gila, R. Frazier, C. R. Abernathy, S. J. Pearton, J. S. Lee, S. Y. Lee, Y. D. Park, Z. G. Khim, J. Kim, and F. Ren, Appl. Phys. Lett. **80,** 3964 (2002).

[126] S. Sonoda, S. Shimizu, T. Sasaki, Y. Yamamoto, and H. Hori, J. Cryst. Growth **237-239**, 1358 (2002).

[127] K. Sato, T. Fukushima, and H. Katayama-Yoshida, Jpn. J. Appl. Phys. Part 2 **46**, L1120 (2007).

[128] Y.D. Park, A. T. Hanbicki, S. C. Erwin, C. S. Hellberg, J. M. Sullivan, J. E. Mattson, T. F. Ambrose, A. Wilson, G. Spanos, and B. T. Jonker, Science **295,** 651 (2002).

[129] A. P. Li, J. Shen, J. R. Thompson, and H. H. Weitering, Appl. Phys. Lett. **86**, 152507 (2005).

[130] S. Cho, S. Choi, S. C. Hong, Y. Kim, J. B. Ketterson, B. J. Kim, Y. C. Kim, and J. H. Jung, Phys. Rev. B **66**, 033303 (2002).

[131] N. Pinto, L. Morresi, M. Ficcadenti, R. Murri, F. D'Orazio, F. Lucari, L. Boarino, and G. Amato, Phys. Rev. B **72**, 165203 (2005).

[132] F. Tsui, L. He, L. Ma, A. Tkachuk, Y. S. Chu, K. Nakajima, and T. Chikyow, Phys. Rev. Lett. **91**, 177203 (2003).

[133] J. S. Kang, G. Kim, S. C. Wi, S. S. Lee, S. Choi, S. Cho, S. W. Han, K. H. Kim, H. J. Song, H. J. Shin, A. Sekiyama, S. Kasai, S. Suga, and B. I. Min, Phys. Rev. Lett. **94,** 147202 (2005).

[134] K. Sato, H. Katayama-Yoshida, and P. H. Dederichs, Jpn. J. Appl. Phys. **44,** L948 (2005).

[135] D. Bougeard, S.Ahlers, A. Trampert, N. Sircar, and G. Abstreiter, Phys. Rev. Lett. **97,** 237202 (2006).

[136] N. Jedrecy, H. J. von Bardeleben, and D. Demaille, Phys. Rev. B **80,** 205204 (2009).

[137] L. Gu, S. Wu, H. Liu, R. Singh, N. Newman, and D. Smith, J. Magn. Magn. Mater. **290-291**, 1395 (2005).

[138] A. Bonanni, Semicond. Sci. Technol. **22**, R41 (2007).

[139] S. Kuroda, N. Nishizawa, K. Takita, M. Mitome, Y. Bando, K. Osuch, and T. Dietl, Nature Mater. **6**, 440 (2007).

[140] B. K. Rao and P. Jena, Phys. Rev. Lett. **89,** 185504 (2002).

[141] T. Hynninen, H. Raebiger, J. von Boehm and A. Ayuela, Appl. Phys. Lett. **88,** 122501 (2006).

[142] D. J. Priour and S. Das Sarma, Phys. Rev. B **73**, 165203 (2006).

[143] A. Chakraborty, R. Bouzerar, S. Kettemann, and G. Bouzerar, Phys. Rev. B **85**, 014201 (2012).

[144] A. Chakraborty, R. Bouzerar, and G. Bouzerar, *to be submitted.*

[145] A.P. Li, J.F. Wendelken, J. Shen, L. C. Feldman, J. R. Thompson and H. H. Weitering, Phys. Rev. B **72,** 195205 (2005).

[146] N. W. Ashcroft and N. D. Mermin, *Solid State Physics* (Saunders, Philadelphia, 1976).

[147] A. Kaminski and S. Das Sarma, Phys. Rev. Lett. **88,** 247202 (2002).

[148] M. Mayr, G. Alvarez, and E. Dagotto, Phys. Rev. B **65,** 241202(R) (2002).

[149] M.P. Kennett, M. Berciu, and R.N. Bhatt, Phys. Rev. B **66,** 045207 (2002).

[150] M. Berciu and R.N. Bhatt, Phys. Rev. Lett. **87,** 107203 (2001).

[151] B. Beschoten, P. A. Crowell, I. Malajovich, D. D. Awschalom, F. Matsukura, A. Shen, and H. Ohno, Phys. Rev. Lett. **83,** 3073 (1999).

181

[152] R. Mathieu, B. S. Sørensen, J. Sadowski, U. Södervall, J. Kanski, P. Svedlindh, P. E. Lindelof, D. Hrabovsky, and E. Vanelle, Phys. Rev. B **68,** 184421 (2003).

[153] S. J. Potashnik, K. C. Ku, S. H. Chun, J. J. Berry, N. Samarth, and P. Schiffer, Appl. Phys. Lett. **79,** 1495 (2001).

[154] S. Das Sarma, E. H. Hwang, and A. Kaminski, Phys. Rev. B **67,** 155201 (2003).

[155] A. Chakraborty, P. Wenk, R. Bouzerar, and G. Bouzerar, Phys. Rev. B **86,** 214402 (2012).

[156] A. Chakraborty, P. Wenk, S. Kettemann, R. Bouzerar, and G. Bouzerar, arXiv:1301.4111.

[157] A. Chakraborty and G. Bouzerar, *to be submitted.*

[158] A. Weiße, G. Wellein, A. Alvermann, and H. Fehske, Rev. Mod. Phys. **78,** 275 (2006).

[159] S. Roche and D. Mayou, Phys. Rev. B **60,** 322 (1999).

[160] R. A. Tahir-Kheli and D. Ter Haar, Phys. Rev.**127**, 88 (1962).

Publications & Articles in preparation

1. *Dynamical properties of a three-dimensional diluted Heisenberg model*
   Akash Chakraborty and Georges Bouzerar, Phys. Rev. B **81,** 172406 (2010).

2. *Magnetic spin excitations in Mn doped GaAs: a model study*
   A. Chakraborty, R. Bouzerar and G. Bouzerar, Eur. Phys. J. B. **81,** 405 (2011).

3. *Nanoscale inhomogeneities: A new path toward high Curie temperature ferromagnetism in diluted materials*
   Akash Chakraborty, Richard Bouzerar, Stefan Kettemann, and Georges Bouzerar, Phys. Rev. B **85,** 014201 (2012).

4. *Spontaneous magnetization in presence of nanoscale inhomogeneities in diluted magnetic systems*
   Akash Chakraborty, Paul Wenk, Richard Bouzerar, and Georges Bouzerar, Phys. Rev. B **86,** 214402 (2012).

5. *Spin-wave excitations in presence of nano-clusters of magnetic impurities*
   Akash Chakraborty, Paul Wenk, Stefan Kettemann, Richard Bouzerar and Georges Bouzerar, arXiv:1301.4111.

6. *Finite temperature spin-dynamics of a three-dimensional diluted Heisenberg model*
   Akash Chakraborty and Georges Bouzerar, (*in preparation*).

7. *Effects of nano-clusters on the Curie temperature in diluted systems: A detailed study*
   Akash Chakraborty *et al.*, (*in preparation*).

Abstract

   This thesis is mainly devoted to the study of nanoscale inhomogeneities in diluted and disordered magnetic systems. The presence of inhomogeneities was detected experimentally in several disordered systems which in turn gave rise to various interesting and unexpected properties. In particular, the possibility of room-temperature ferromagnetism generated a huge thrust in these inhomogeneous materials for potential spintronics applications. However, a proper theoretical understanding of the underlying physics was a longstanding debate. In this manuscript we provide a detailed theoretical account of the effects of these nanoscale inhomogeneities on the magnetic properties of diluted systems. First we show the importance of disorder effects in these systems, and the need to treat them in an appropriate manner. The self-consistent local RPA (SC-LRPA) theory, based on finite temperature Green's function, is found to be the most reliable and accurate tool for this. We have successfully implemented the SC-LRPA to study the dynamical magnetic properties of the 3D nearest-neighbor diluted Heisenberg model. The percolation threshold is found to be reproduced exactly in comparison with previous existing studies. Following this, we discuss the essential role of a minimal model approach to study diluted magnetic systems. The one-band V-J model, has been used to calculate the Curie temperature and the spin excitation spectrum in (Ga,Mn)As. An excellent agreement is obtained with first principles based calculations as well as experiments. Finally we propose an innovative path to room-temperature ferromagnetism in these materials, by nanoscale cluster inclusion. We find a colossal increase in T_C of up to 1600% compared to the homogeneous case in certain cases. Also the spontaneous magnetization is found to exhibit anomalous non-mean-field like behavior in the presence of inhomogeneities. In addition we observe a complex nature of the magnon excitation spectrum with prominent features appearing at high energies, which is drastically different from the homogeneous case. Our study interestingly reveals a strong suppression of the spin-stiffness in these inhomogeneous systems. The results indicate toward the strong complexities associated with the interplay/competition between several typical length scales. We believe this work would strongly motivate detailed experimental as well as theoretical studies in this direction in the near future.

   Keywords: nanoscale inhomogeneities, diluted magnetic systems, Curie temperature, magnon excitation spectrum, spin-stiffness, magnetization, disordered systems, percolation, thermal and transverse fluctuations, self-consistent local RPA, Green's functions, model approach

Résumé

Cette thèse est principalement consacrée à l'étude des inhomogénéités de taille nano-métrique dans les systèmes magnétiques désordonnés ou dilués. La présence d'inhomo-généités, souvent mise en évidence dans de nombreux matériaux, donne lieu à des pro-priétés physiques intéressantes et inattendues. La possibilité de ferromagnétisme à l'ambian-te dans certains matéraux a généré un grand enthousiasme en vue d'application dans la spintronique. Cependant, d'un point de vue fondamental la physique de ces systèmes reste peu explorée et mal comprise. Dans ce manuscrit, on se propose de fournir une étude théorique complète et détaillée des effets des inhomogenéités de tailles nanométriques sur les propriétés magnétiques dans les systèmes dilués. Tout d'abord, on montre que l'approche RPA locale autocohérente est l'outil le plus adapté et fiable pour un traite-ment approprié du désordre et de la percolation. Nous avons implémenté cet outil et étudié dans un premier temps, les propriétés magnétiques dynamiques d'un modèle Heisen-berg dilué (couplages premiers voisins) sur un reseau cubique simple. Nous avons re-produit précisémment la disparition de l'ordre à longue portée au seuil de percolation et comparé ce travail à des études précédentes. Dans le cadre d'un Hamiltonien min-imal (modèle V-J) nous avons ensuite étudié en détails les propriétés magnétiques de (Ga,Mn)As (température critique, excitations magnétiques, stiffness,..). Nous avons obtenu de très bon accords avec les calculs *ab initio* et les résulats expérimentaux. Finalement, nous avons étudié les effets des inhomogénéités dans les sytèmes dilués. Nous avons montré, qu'inclure des inhomogenéités pourrait s'averer être une voie très efficace et prometteuse pour dépasser l'ambiante dans de nombreux matériaux. Nous avons pu obtenir une aug-mentation colossale de la température critique dans certains cas comparée à celle des systèmes dilués homogènes. Nous avons atteint une augmentation de 1600% dans cer-tains cas. Nous avons également analysé les effets des inhomogénéités sur les courbes d'aimantations, elles sont inhabituelles et peu conventionelles dans ces systèmes. Les spectres d'excitations magnétiques sont très complexes, avec des structures très riches, et présentent de nombreux modes discrets à haute energie. De plus, nos calculs ont montré que la "spin-stiffness" est fortement supprimé par l'introduction d'inhomogénéités. Il reste encore de nombreuses voies à explorer, ce travail devrait servir de base à de futures études théoriques et expérimentales des systèmes inhomogènes.